VARIABLE RELUCTANCE MOTOR AIRGAP GEOMETRY FOR MAXIMIZING FORCE PRODUCTION: A DATA ANALYSIS APPROACH USING FINITE ELEMENT GENERATED CHARACTERISTICS

By

Nasir Abdulai Boakye-Boateng

Raga Ahmed
Assistant Professor of Electrical Engineering
(Chair)

James C. Newman III
Professor of Computational Engineering
(Committee Member)

Abdul R. Ofoli
UC Foundation Associate Professor of Electrical Engineering
(Committee Member)

Roger Nichols
Associate Professor of Mathematics
(Committee Member)

VARIABLE RELUCTANCE MOTOR AIRGAP GEOMETRY FOR MAXIMIZING FORCE PRODUCTION: A DATA ANALYSIS APPROACH USING FINITE ELEMENT GENERATED CHARACTERISTICS

By

Nasir Abdulai Boakye-Boateng

A Dissertation Submitted to the Faculty of the University
of Tennessee at Chattanooga in Partial Fulfillment of
the Requirements of the Degree of Doctor of
Philosophy in Computational Engineering

The University of Tennessee at Chattanooga
Chattanooga, Tennessee

May 2020

Copyright © 2020

By Nasir Abdulai Boakye-Boateng

All Rights Reserved

ABSTRACT

Recent widespread utilization of variable reluctance (VR) motors and growing computational capability motivate further research to improve VR motor modeling and control. The primary objective of this study is to identify airgap geometries that maximize force density and minimize force ripple for linear variable reluctance (LVR) motors with both magnetically coupled and uncoupled phases. Complementary objectives include expanding the scope for candidate geometries to include a finer variation of tooth width and non-rectangular tooth shapes and using a comprehensive data analysis framework based on a nonlinear model for LVR motors formed from finite element analysis (FEA) generated characteristics.

The main contribution of this study is the identification of the LVR motor geometry that meets the specified objectives. Further to the existing literature, it establishes the non-monotonous nature of the effect of tooth width on force density and force-ripple; force-ripple reduction is a primary concern of most LVR drive design. The study specifies a narrower range of tooth widths for both high thrust and low force ripple applications. The study introduces tooth fillet parameters; specific values of these further increase LVR output thrust, and the data shows which range of tooth fillets maximize thrust.

Three salient applications of this study are as follows. (i) The detailed FEA-based characterization of the large family of motors has highlighted the effect of airgap geometry and motor characteristics and the set of tooth geometry parameters that impact attributes such as force density.

(ii) The data generated from characterization forms a nonlinear model of the motor that compares well with FEA-based results and is applicable as a predictive plant model in LVR drive design. (iii) The optimal commutation of the family of LVR motors confirms the effect of tooth geometry on attributes such as root mean square (RMS) force density.

The findings regarding the uncoupled configuration of the motor apply to the rotary VR motor and have a more extensive application. The document has suggestions for further study regarding areas of additional refinement for the optimal LVR motor geometry, tools to aid future research, and improvement of the LVR motor's nonlinear model.

ACKNOWLEDGMENTS

In the name of Allah, the Most Gracious, ever Merciful, these words cannot fully express the depth of gratitude for the invaluable support that made this work possible. They came from diverse sources that directly influenced this work and indirectly provided the administrative, moral, and guiding support that made this work possible.

The kernel of the direct support came from Dr. Raga Ahmed (committee chair) and the members of the committee, namely Dr. James C. Newman III, Dr. Abdul R. Ofoli, and Dr. Roger Nichols. They were the tip of the spear, along with an anchor of notable teachers that shaped my education. Notable are my parents Ahmad and Haleema Boakye, Enoch Boateng of my primary education, Sebastian Adu-Gyamfi of my junior high school, Asare Anim of my high school education, and Dr. Timothy W. Swafford for sparking my interest in Computational Engineering. Their support would not be complete without the valuable references from a whole committee of authors and researchers whose works I have cited in this body of work. Also, to my fellow students, faculty, non-faculty staff, and an entire community of support through the University of Tennessee System and beyond that made this possible. These are to express my gratitude to you all.

To my loving family, who gets me the most, your love, caring, and steadfast support throughout this journey has been the beacon that laid the bright path. My wife, Ammatur-Raheem Egyin, my children Nasira, Ahmad, Shahid, my parents, siblings, and the entire Boakye family in Ghana, the United States, and New Zealand; you are most treasured. Stay blessed.

TABLE OF CONTENTS

ABSTRACT iv

ACKNOWLEDGMENTS vi

LIST OF TABLES x

LIST OF FIGURES xi

LIST OF ABBREVIATIONS xiv

LIST OF SYMBOLS xv

CHAPTER

1. INTRODUCTION 1

    1.1 Linear Variable Reluctance Motors 1
        1.1.1 Applications 6
    1.2 Problem Description 7
    1.3 Research Objectives and Literature Review 9
        1.3.1 Characterization 10
        1.3.2 Nonlinear Modeling 12
        1.3.3 Optimal Commutation 13
    1.4 Dissertation Outline 15
    1.5 Preview of Contributions 16

2. CONFIGURATION, TOOLS AND DATA MANAGEMENT 18

    2.1 Introduction 18
    2.2 Solver Design 18
        2.2.1 Governing Equations 19
            2.2.1.1 Differential Form of Maxwell's Equations 19
            2.2.1.2 Static Magnetic Fields 21
            2.2.1.3 Magnetic Vector Potential 24
                2.2.1.3.1 Two-Dimensional Problems 25

2.2.1.3.2 Three-Dimensional Problems 27
2.2.2 Finite Element Formulation 28
2.2.2.1 Newton's Method 28
2.2.2.2 Weighted Residual Method 31
2.2.2.2.1 The Weak Form 33
2.2.2.3 Selection of Weight Functions 35
2.2.3 Solver Selection and Configuration 35
2.2.3.1 deal.II 35
2.2.3.2 MagNet® 36
2.3 Motor Design Specification 38
2.3.1 Construction 39
2.3.2 Motor Geometric Characteristics 41
2.4 Simulation Setup 45
2.4.1 Data Management 48
2.4.1.1 Application Layer Implementation 50

3. CHARACTERIZATION 52

3.1 Introduction 52
3.2 Motor Characteristics 53
3.2.1 Translator Position 54
3.2.2 Phase Excitation 54
3.2.2.1 Uncoupled LVR motor 54
3.2.2.2 Coupled LVR motor 55
3.2.3 Instantaneous Force Production Profile 56
3.2.3.1 Uncoupled LVR motor 57
3.2.3.2 Coupled LVR motor 58
3.2.4 Instantaneous Flux Linkage 60
3.2.4.1 Uncoupled LVR motor 60
3.2.4.2 Coupled LVR motor 63
3.2.4.2.1 Saturation 64
3.3 Effect of Tooth Geometry on Motor Characteristics 65
3.3.1 Analytical Model 66
3.3.2 Parameter Selection 67
3.3.3 Comparison of Force Production for Various Tooth Shape Factors 68
3.3.3.1 Uncoupled LVR motor 69
3.3.3.2 Coupled LVR motor 74
3.3.4 The Effect of Fillets and Tapering on Force Production 78
3.3.4.1 Uncoupled LVR motor 78
3.4 Nonlinear Modeling 80
3.5 Cubic Spline Interpolation for Each Motor Configuration 81
3.5.1 Uncoupled LVR motor 81
3.5.1.1 Verification of the Cubic Spline Interpolation Model 81

3.5.2 Coupled LVR motor ... 83

4. OPTIMAL COMMUTATION ... 85

4.1 Introduction ... 85
4.2 Cost Function Setup ... 85
4.3 Optimization With Nonlinear Model ... 90
4.3.1 Maximum Average Force ... 90
4.3.1.1 Uncoupled LVR motor ... 90
4.3.1.2 Coupled LVR motor ... 91
4.3.2 Ripple-Specified Maximum Average Force ... 92
4.3.2.1 Uncoupled LVR motor ... 93
4.3.2.2 Coupled LVR motor ... 97
4.3.3 Minimum Power Dissipation ... 99
4.3.3.1 Uncoupled LVR motor ... 100
4.3.3.2 Coupled LVR motor ... 101
4.3.4 Practical Range of Tooth Geometries ... 101

5. CONCLUSION ... 103

5.1 Summary of Contributions ... 103
5.2 Recommendations for Further Study ... 105

REFERENCES ... 107

VITA ... 113

LIST OF TABLES

2.1 Common Design Parameters of Linear Variable Reluctance Motors 42

3.1 Comparison of Full Pitch Force Production and Force Densities for Various Designed Motor Tooth Shape Factors (α) 71

3.2 Comparison of Full Pitch Force Production and Force Densities for Various Designed Motor Tooth Shape Factors (α) 77

LIST OF FIGURES

1.1 Structure of Linear Variable Reluctance Motors 2

2.1 Basic components of static magnetic field problems. 22

2.2 Common Structural Components of Coupled and Uncoupled Linear Variable Reluctance Motors 40

2.3 Parameters that define airgap geometry 41

2.4 Tooth configurations with varying tooth geometry 46

2.5 Data Management System Architecture 49

2.6 Technology Layer Implementation 51

3.1 Tooth geometry for initial characterisation 53

3.2 Instantaneous force production for various phase 1 excitations of the uncoupled motor 57

3.3 Instantaneous force production for various normalized positions of the uncoupled motor 58

3.4 Instantaneous force production for various phase 1 excitations of the coupled motor 59

3.5 Instantanous flux linkage for various normalized positions of the uncoupled motor 61

3.6 Instantaneous flux linkage for various phase 1 excitations of the uncoupled motor 62

3.7 Instantaneous flux linkage for various phase 1 flux linkage of the coupled motor 63

3.8 Tooth configurations with varying tooth shape factor 67

3.9 Tooth configurations with varying tooth edge fillet 68

3.10 Tooth configurations with varying tooth base fillet 68

3.11 Tooth configurations with varying tooth edge offset 69

3.12 Effect of tooth shape factor on full pitch force production of the uncoupled motor 70

3.13 Effect of tooth shape factor on magnetic saturation of the uncoupled motor 72

3.14 Flux lines for finite element analysis runs for various motor geometries 73

3.15 RMS force production of various tooth geometries of the coupled motor 74

3.16 Effect of tooth shape factor on full pitch force production of the coupled motor 76

3.17 The effect of tooth fillets on force production of the uncoupled motor 79

3.18 Test phase 1 excitation currents over one tooth pitch 82

3.19 Comparison of nonlinear model and finite element analysis force outputs for the uncoupled motor 83

3.20 Comparison of nonlinear model and finite element analysis force outputs for the coupled motor 84

4.1 Maximum force output and force ripple of the uncoupled motor subject to optimal phase excitation 91

4.2 Maximum force output and force ripple of the coupled motor subject to optimal phase excitation 92

4.3 Optimal phase excitation and instantaneous force output for the uncoupled motor with tooth shape factor $\alpha = 0.4$ 93

4.4 Variation of maximum force output with ripple constraints on the uncoupled motor 94

4.5 Optimal commutation of the uncoupled motor subject to no force ripple constraint 94

4.6 Optimal commutation of the uncoupled motor subject to 50% force ripple constraint 95

4.7 Optimal commutation of the uncoupled motor subject to 5% force ripple constraint 96

4.8 Optimal commutation of the uncoupled motor subject to 0.5% force ripple constraint and minimum copper loss. 96

4.9 Effect of force ripple constraint on maximum force output of the uncoupled motor when subject to minimum copper loss 97

4.10 Effect of force ripple constraint on the uncoupled motor when subject to minimum heat dissipation. 98

4.11 Effect of force ripple constraints on the maximum force and optimal geometry of the coupled motor 99

4.12 Optimal commutation of the coupled motor with tooth shape factor $\alpha = 0.3$ subject to 50% force ripple 100

LIST OF ABBREVIATIONS

API, Application program interface

AWG, American wire gauge

DB, Database

FEA, Finite element analysis

LVR, Linear variable reluctance

MCA, Magnetic circuit analysis

PCHIP, Piecewise cubic Hermite interpolating polynomial

RHS, Right hand side

RMS, Root mean square

SQL, Structured query language

VR, Variable reluctance

XML, Extensible markup language

LIST OF SYMBOLS

α, Tooth shape factor

α_P, Practical tooth shape factor

$\mathbb{A}$, Magnetic vector potential

β, Force ripple constraint factor

$\mathbb{B}$, Magnetic flux density

$\mathbb{D}$, Electric flux density

δ_F, Instantaneous force ripple

δ_{te}, Tooth edge offset

Δ_F, Force ripple

Δ_{Fcon}, Force ripple limit

Δ_{Fmax}, Maximum force ripple

$\mathbb{E}$, Electric field intensity

$\mathbb{E}_i$, Impressed electric field

ϵ, Permittivity

ϵ_0, Permittivity of vacuum

ϵ_r, Relative permittivity

f, Instantaneous force

f_p, Pole fillet

f_{tb}, Valley fillet

$R_{f_{tb}}$, Valley fillet radius

f_{te}, Tooth fillet

F, Force

F_{avg}, Average force

F_{RMS}, RMS force

FD_{RMS}, RMS force density

$F_{avg_{max}}$, Maximum average force

F_{RMS_max}, Maximum RMS force

Γ_H, Field normal boundary

Γ_B, Flux tangential boundary

Γ_{m0}, Boundary between magnetic material and air

$\mathbb{H}$, Magnetic field intensity

i, Instantaneous current

$\mathbb{J}$, Electric current density

$\mathbb{K}$, Surface current density

l_b, Back iron length

l_d, Device depth

l_g, Airgap length

l_p, Pole length

l_t, Tooth length

L, Inductance

λ, Flux linkage

$\mathbb{M}$, Magnetization

m, Pole pitch integer

n, Teeth per pole

n_p, Poles per phase

p_t, Tooth pitch

Ω_0, Air box domain

Ω_m, Magnetic material domain

ρ, Electric charge density

p_{ph}, Phase pitch

$\mathbb{P}$, Polarization

P, Loss

P_{avg}, Average loss

P_{RMS}, RMS loss

R, Resistance

$R_{f_{te}}$, Tooth fillet radius

μ, Permeability

μ_0, Permeability of vacuum

μ_r, Relative permeability

v, Reluctivity

V_T, Translator volume

w_t, Tooth width

w_v, Valley width

W, Stored magnetic energy

x, Motor position

x_n, Normalized motor position

ϕ, Weight function

CHAPTER 1

INTRODUCTION

1.1 Linear Variable Reluctance Motors

Linear variable reluctance (LVR) motors are a class of electric machines that yield mechanical thrust along a linear axis with defined endpoints using the principle of alignment of magnetic flux. Unlike induction and synchronous motors, where the magnetic field in the moving component interacts with that in the stationary part to generate thrust, the moving component of the variable reluctance (VR) motor is the only source magnetic field, and it is solely responsible for producing thrust. The tendency to minimize airgap reluctance displaces the moving component to the position that minimizes airgap reluctance for the magnetic field generated in the moving part and thereby yields a net thrust as it moves to this position. This position presents stable equilibrium, so long as the magnetic field remains unchanged. Changing the magnetic field by altering excitation current changes the configuration that minimizes airgap reluctance, and the moving component displaces to minimize reluctance. Applying varying phase excitation (commutation) helps to achieve continuous motion in LVR motors. Commutation and airgap geometry are, therefore, essential parts of LVR drive technology.

The conventional LVR motor consists of a laminated steel-cored moving part (translator) that hosts the coils used to engage a stationary component (stator) and a large airgap between the two. The most common translator configuration consists of three phases, with poles bearing one

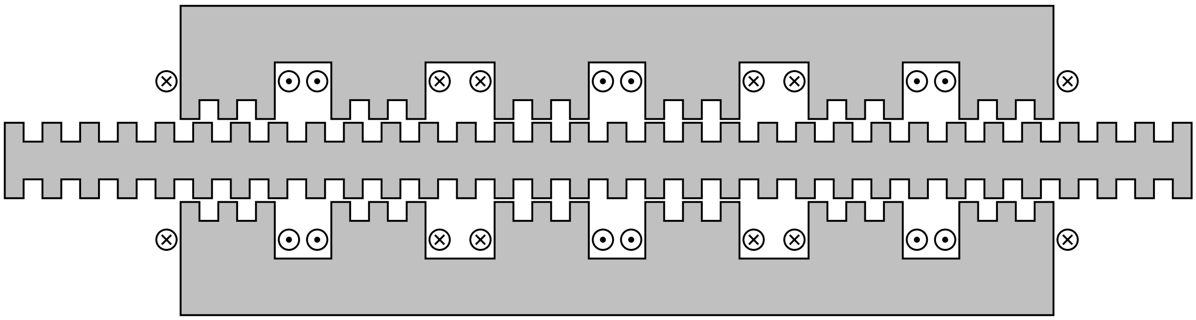

(a) Uncoupled configuration

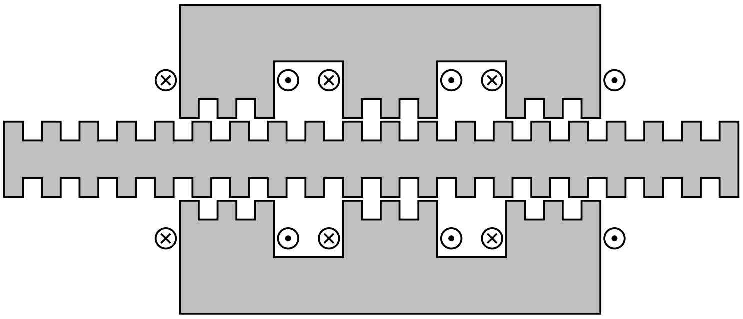

(b) Coupled configuration

Figure 1.1 Structure of Linear Variable Reluctance Motors

or more teeth each. Coils are typically located on the poles [1–3]. The main design distinction between the variable reluctance and hybrid motor is that the latter makes use of a permanent magnet, whereas excitation current solely drives the former [1–3].

Similar to a generally accepted set of terms for parts of the rotary motor (namely, the stator for the stationary part and rotor for the moving part), there are terminologies used to describe the components of linear motors. The stationary part has been called a stator, or forcer [1–3], in the literature. The moving part has likewise been called a translator, or platen [1–3], in literature. For clarity, stator and translator would refer to the stationary and moving parts of linear motors, respectively, henceforward.

The linear configuration and thrust generation through variable airgap reluctance (which is highly dependent on the magnetic core geometry of the motor), impact characteristics, commutation, and potential applications [1] of linear variable reluctance motors. Airgap reluctance is vital to the operation of linear variable reluctance motors, and the presence of teeth leads to varying airgap reluctance with tooth position. Varying airgap reluctance produces force, and constant airgap reluctance results in zero thrust. Tooth width should be wide enough to ensure non-zero air gap reluctance for all positions, and narrow enough to ensure that there are no positions where the slope of the airgap reluctance is zero with respect to position. LVR motors typically have more significant airgaps than synchronous or inductance motors, due to this characteristic. The shape of the teeth on translators and stator determine the variations in the airgap geometry and, thus, magnetic reluctance. The tooth geometry is, therefore, a proxy for airgap geometry.

The interaction between two time-varying magnetic fields generates thrust in synchronous and induction motors, and thrust is, therefore, dependent on time and independent of position. Variable reluctance motors, on the other hand, move to minimize airgap reluctance by aligning magnetic flux. For any given variable reluctance motor, airgap reluctance is a function of airgap geometry and excitation current. Since airgap geometry is affected by tooth shape and motor position, thrust is a function of tooth shape, motor position, and excitation current. The tooth geometry is constant for any given motor design. Hence for any specific variable reluctance motor, thrust is a function only of motor position and excitation current and independent of time.

Since airgap reluctance varies with motor position, the maximum thrust that is attainable varies with the position for any given excitation current. Therefore, for any given excitation current, output force peaks to a maximum positive force and troughs to a minimum negative force (of equal magnitude) depending on motor position. Under conventional control, pulses of excitation current drive the motor, and the full range of output thrust results in force ripple that most applications desire to eliminate. The excitation current needs to be changed, as the position changes, depending on the desired motion profile of the motor. Commutation is the application of continuously varying excitation current with the motion of the motor to achieve the desired motion profile. The need to minimize force ripple adds to the complexity of commutation and control.

LVR motors produce translational mechanical thrust along a linear axis with defined endpoints. Unlike rotary motors whose thrust is rotational about a central axis, the presence of endpoints introduces end effects that distinguish the behavior of linear motors from their rotary counterparts. Through the introduction of end effects, inherently more significant airgaps, and a different magnetic circuit, LVR motors are significantly more complicated to model than other linear motors [1].

A common practice is to produce linear motion from a rotary motor through the use of gears, pulleys, worm screws, and other mechanisms. The preference for this rotary-to-linear configuration is driven by the relatively higher efficiency of rotary motors compared to their linear counterparts due to their inherently smaller airgaps. LVR direct drive systems, however, have higher overall efficiency, they are quieter and more reliable. They can be less expensive than equivalent rotary-to-linear systems due to the elimination of motion conversion mechanisms.

Some of the advantages of LVR over rotary motors include the following [1–4].

- Higher thrust with lower wear during acceleration or deceleration due to the absence of mechanical contact and friction.

- Withstands hostile environments better due to better mechanical and electrical protection.
- They are easier to repair, maintain, and replace parts.
- Exerts linear thrust without mechanical contact and controls speed with electromagnetic gearing.
- The existence of a net normal force that enables the stabilization of levitation machines.
- Higher positioning accuracy due to the absence of backlashes in mechanical converters.
- Linear variable reluctance motors experience less core loss due to the electromagnetic coupling between the stator and the translator [1–3].
- They are less expensive than all other alternatives for linear motion [1–3].
- They also experience less stalling at higher speeds [1–3].
- In open-loop control, they operate as stepper motors, and closed-loop control is used for precise position and velocity control.

Some of the disadvantages of LVR motors include the following:

- Even though variable reluctance linear motors have been in existence for a long time [1–3], there is still relatively much less understanding of their commutation and control compared to other motors.
- Just like their rotary counterparts, linear variable reluctance motors can be noisy [1–3].

- In open-loop control, they usually operate in a full-step mode with lower precision [1–3] than is achievable. Complex control is required in closed-loop to improve precision.

1.1.1 Applications

Linear variable reluctance (LVR) motors have a wide range of applications because they are simple to construct, inexpensive, and very reliable. The areas of application classify them into force, power, or energy machines. LVR motors are force machines when used in short-stroke applications at rest or low speeds. These are low-power operations where efficiency is not a significant concern. Power LVR motors operate at medium to high speeds over sustained periods, requiring high efficiency. Energy LVR motors are short-duty, high energy configurations that are typically used as accelerators and impact extruders [1].

Whereas rotary motors are not suited for speeds above $250km/hr$ due to mechanical limitations such as adhesion, LVR motors attain their highest efficiencies at speeds exceeding $250km/hr$. In such applications, the combination of LVR motors' net normal force and thrust can provide magnetic levitation to guide vehicles at high speed. Thrust also serves the three functions of accelerating the vehicle to cruising speed, balancing drag on the vehicle at that speed, and providing braking deceleration. The most numerous applications are low-speed, including placement systems, traction of overhead cranes, drive for conveyance systems, automated fabrication systems, and instrumentation. Energy applications for launching air crafts were the earliest for LVR motors. Other subsequent applications include high-speed actuators in circuit breakers and accelerators for high-velocity projectiles [1, 3].

1.2 Problem Description

The specific application of electrical motors determines the choice of their mechanical and electromechanical design [1–3], and each design element comes with its advantages and disadvantages. For precise linear motion where the motor position is of interest, the linear motor is preferred. Precision can be achieved by either coupling a threaded rod with a rotary motor, or by applying a genuinely linear motor. The latter is preferred since their geometry is consistent with their motion, and there is no loss of efficiency due to mechanical transmission [1–3]. There are two choices of linear motors that support both open- and closed-loop position control, namely the variable reluctance (VR) motor and the hybrid [2]. Hybrid motors require permanent magnets, making them susceptible to demagnetization over time. They are also more expensive to construct and maintain as a result.

The specific class of motors investigated in this document is linear variable reluctance (LVR) motors. Figure 1.1 depicts two typical configurations of the motor. The coupled configuration has a high mutual inductance between its phases. It requires continuous 3-phase excitation currents as opposed to the switched excitation requirement for the uncoupled configuration (with negligible phase mutual inductance). It operates on the principle that its magnetic circuit reluctance is position-dependent and varies in the direction of its motion.

Although not in common use compared to rotary motors, the linear variable reluctance (LVR) motor can substitute rotary-to-linear drives and other linear motors because of the following advantages that are unique to them [1] (in addition to those common to linear electric motors).

- They can be precisely controlled in an open-loop in steps as small as $0.1mm$, and to an even higher resolution in closed-loop control.
- They have a simple construction and robust to operate.
- They have a longer operating life because repeated stalling does not damage them.
- They require only simple electronic controllers to eliminate cumulative error in operation.

However, the following disadvantages limit their application under normal pulse commutation [1].

- Under open-loop control, they have low power efficiency, a fixed step size, and potential for a significant overshoot or oscillations.
- The motor inertia can limit the stroke length for large payloads.
- Open-loop positional errors for frictional loads.
- Higher complexity of electronic commutation and control in closed-loop control.

Previous research has demonstrated that higher efficiency controllers that optimally apply phase commutation can overcome the known disadvantages of LVR motors without adversely affecting their advantages [1]. In such precise controllers, the number of steps equals the number of controller pulses; and it attains precise sub-step positioning by accurate application of phase commutation. To develop these high-efficiency controllers, a representative model of the motor to be controlled is essential for tuning and initial verification. Such a motor model characterizes which phase commutations optimally produce the desired output thrust for a given position.

Because they typically operate with magnetic saturation, hysteresis, and eddy-currents, precise analytical calculation of their differing reluctance with the motor's position is inconvenient and error-prone in practice. Hence, analytical motor models are limited in practice, and they lose their accuracy, or they become overly complicated with complex airgap geometry. Finite element analysis is the preferred method for the characterization of LVR motors [1, 5].

This study investigates the effect of airgap geometry on the characterization and optimal commutation of LVR motors using finite element analysis. This study develops a finite element characterization for a wide range of airgap geometries for both coupled and uncoupled LVR motors and derives the optimal commutation for each geometry. Analyzing the maximum output force for the various geometries under optimal commutation helps to select the airgap geometries that respectively maximize output force, minimize force ripple, and maximize efficiency.

1.3 Research Objectives and Literature Review

The primary objectives of this study are to:

- identify the tooth geometries that respectively maximize output force, minimize force ripple, and maximize efficiency.
- determine the effect of tooth geometry on characterization and optimal commutation and identify optimal airgap geometries for LVR motors.
- define the optimal commutation current waveforms for the family LVR motors.
- develop a nonlinear model for each motor characterized.

- use finite element analysis to characterize a family of LVR motors with varying airgap geometry and phase coupling.

Although literature search found published works that address some of the objectives of this research, the approach of using finite element analysis to characterize the full range of airgap geometries of LVR motors (including non-rectangular tooth shapes) and the data management framework introduced are new in this study. The following subsections discuss existing published research on the characterization, nonlinear modeling, and optimal commutation of LVR motors.

1.3.1 Characterization

The first focus of this study is on the characterization of the LVR motor [5–15], including the effect of tooth geometry on force production and force density. Experimental characterization provides the most accurate data for analyzing any given geometric configuration of the LVR motor, as seen in [4,16,17]. These setups accurately represent the effect of magnetic saturation, hysteresis, and eddy-currents on the characteristics of a given motor. However, due to the cost of experimental setups, published research has only characterized a limited range of motor geometries. Also, there is a high cost and time requirement that makes it prohibitive to continually change the airgap geometry of the motor in experimental setups. Because of these limitations, the experimental approach is not scalable when developing wide-ranging studies that analyze a large number of geometries or explore ways to tune geometric parameters. As a result, there is minimal experimental data on the coupled configuration of LVR motors. Studies that include tooth geometry variation require a more considerable amount of data for analysis or design compared to the study of a single select model; this makes data generation using accurate numerical analysis rather than experimental prototyping an attractive option. The experimental approach is, therefore, not cost-effective for a study that explores a wide range of airgap geometries such as this.

The most common approach to characterizing variable reluctance motors in existing literature has been to rely on analytical models as a more computationally inexpensive alternative to FEA. Such models, however, have limited ability to model complex geometries [1]. The effect of tooth geometry on force production has been investigated in [11] using a linear model that does not account for saturation and is limited to only varying tooth width. [10, 15] investigate the effect of tooth shape on force production, but the model used is linear and does not account for saturation and harmonics. [14] used lumped parameter magnetic circuit analysis (MCA) and motor dynamics to develop a coupled network model of the coupled LVR for dynamic simulation for a brute force search for the best geometry for the fastest point-to-point move.

Although data using FEA is of comparable accuracy to experimental data (see, results of, [1, 5, 10, 14, 18–20]), the scope of application of FEA in characterizing variable reluctance motors is still limited to a small range of geometries. Transient 2D FEA has been used to characterize and compare three geometries of the uncoupled LVR motor in [6]. 3D finite element analysis with experimental verification has been used in [9] to compare the dual side mover, and segmental stator uncoupled LVR motor. [7, 8] investigated the optimal design of the linear switched reluctance motor that does not focus on its airgap geometry, but on other aspects such as winding topology and general geometric dimensions.

A literature search found no results for characterization using FEA and involving the range of tooth geometries in the study. The tooth geometries found in the search are all rectangular and limited to a few choices of tooth widths; no consideration has been given to including tooth angle, edge fillet, or base fillet. The present study uses FEA and also investigates which tooth geometry is favorable for improved force production, not for a specific motion application. It analyses a higher number of tooth widths and includes tooth fillets and tapering in the airgap geometry. It addresses the computational challenge of FEA by taking advantage of motor symmetry and using 2D magnetostatic FEA.

Due to the full range of motor geometries and phase excitations used in characterization (the continuous three-phase-excitation feature of the coupled motor compounds the scope of excitation currents challenge), a large volume of data is generated to form the nonlinear model of the motor. Data for full characterization over a fundamental period of operation considers, as independent variables, the position of the translator and the currents of all phases simultaneously. A more precise understanding of the effects of three-phase currents and tooth geometry on any of the dependent variables of interest (including force production) requires five-dimensional data representation in a two-dimensional plane. A multi-plot matrix is used to achieve this objective.

1.3.2 Nonlinear Modeling

The second focus of this study is the application of the dataset acquired from characterization in the nonlinear modeling of the LVR motor for analysis and control of the motor. The model takes excitation currents and position as input and outputs force, flux linkage, and magnetic co-energy. Such a model that accounts for saturation, as well as harmonics, is required for commutation and control design; dynamic performance requirements are not well satisfied by less detailed models that assume magnetic linearity [16] or ignore harmonics.

Several examples of mathematical models generated from characterization exist in the literature. [21, 22] presents a model of the rotary counterpart of the uncoupled LVR motor that accounts for magnetic saturation. Machine learning has been used to develop the nonlinear model of rotary LVR motors using a genetic algorithm and simulated annealing in [23] and particle swarm theory in [24]. [25] uses a Fourier series approach to develop an analytical model of the phase inductance of an LVR motor with position and current as independent variables; that model takes non-linearity of the magnetic circuit into account.

The model used in this study is a fast and straightforward nonlinear model based on a grid of outputs developed from an extensive set of FEA simulations.

1.3.3 Optimal Commutation

This study finally presents the effect of tooth geometry on the operating limits of the linear variable reluctance (LVR) motor under optimal commutation subject to multiple operating objectives. For each objective, this study also produces a database of optimal excitation waveforms and the corresponding instantaneous force profiles for all of the motor geometries. The relative performance of all motor geometries under each objective function becomes a basis for selecting an LVR motor for applications where the constraints associated with the objective functions apply.

The first objective function determines how the maximum average force output of the motor over one tooth pitch varies with tooth geometry. Using this objective function [26–28] derived optimal current waveforms for the rotary equivalent of the variable reluctance (VR) motor using an analytical model of the motor that did not account for saturation or harmonics. In this study, the underlying model is formed using a parametric set of finite element simulations that were used to develop a nonlinear model of the motor. Ref. [29] used this objective function to assess the performance limits for a specific geometry of the uncoupled LVR motor using the finite element method but did not extend the study to a full range of tooth geometries.

The second objective function determines the effect of ripple constraints on the maximum average force output of each motor geometry over one tooth pitch. The reduction of force ripple is a common objective in many optimal commutation and control applications of the LVR motor. Force ripple is often an undesirable feature of both linear and rotary reluctance variable (VR) motors. See [30–42]. This study additionally performs geometry optimization by comparing the optimal performance of a wide range of airgap geometries.

Finally, the first two objective functions were extended to impose power dissipation reduction as an additional constraint. The comparative performance of the various motor geometries presented in resulting data forms the basis for selecting motors for applications similar to those given in the above objective functions but with the additional constraint of maximizing efficiency by minimizing copper losses.

Using all the above constraints [26] derived optimal current waveforms for the rotary equivalent of the variable reluctance (VR) motor using an analytical model of the motor that accounted for saturation or harmonics; the study, however, did not look at the effect of geometry on optimal commutation. The approach used in [43–50] for optimal current commutation for the rotary equivalent motor required the specification of turn-on and turn-off angles which limit the range of possible excitation waveforms and could lead to a local minimum that is higher than the global minimum that is being sought. This study removes this constraint in finding the optimal current waveforms. Also, [10, 11] used all the above objective functions to determine the optimal commutation of the uncoupled LVR motor using magnetic circuit analysis (MCA) based models that did not account for saturation, and they used a smaller set of tooth geometries than that considered in this study.

Compared to previous studies, this study uses the finite element method to generate a high-resolution lookup table that forms the basis for nonlinear modeling of a wide range of tooth geometries of the uncoupled LVR motor. The model is then used to determine the optimal commutation of each motor geometry subject to ripple and power dissipation constraints. Based on these, one can select particular motor geometries that are optimal for specific application conditions. And, the library of excitation current waveforms would narrow down the lookup table to those current excitations that meet operational objectives.

1.4 Dissertation Outline

The remainder of this dissertation is organized as follows. Chapter 2 begins with a discussion of the solver that performs the finite element analysis (FEA) based on the characterization of the motor. It outlines the solver selection criteria and identifies a specific solver for use in this study. It concludes with a discussion of the simulation and data analysis driver for managing all characterization and optimal commutation data.

Chapter 3 discusses the FEA characterization and nonlinear modeling of coupled and uncoupled LVR motors. It begins by defining the common configuration properties of the motors, the parameterization of their different features and excitation currents, and the configuration of the solver used. Then it discusses the results of characterization and the effect of tooth geometry on characterization.

Chapter 4 presents the optimal commutation of coupled and uncoupled LVR motors. It starts with the methodology for setting up cost functions for optimization. Then it discusses the results of optimizing the commutation of each motor to maximum thrust, minimize heat dissipation, and minimize ripple in force output. Finally, there is a comparative analysis of the optimal commutation of different motor geometries. Chapter 5 reviews the findings of the research and outlines avenues for future research.

1.5 Preview of Contributions

The main contribution of this dissertation is the identification finite element analysis (FEA) based characterization of airgap geometry for optimal commutation of both coupled and uncoupled linear variable reluctance (LVR) motors. It identifies which airgap geometries provide the highest thrust and minimizes force ripple while also minimizing heat dissipation, and what commutation of the motor geometry achieves this objective.

It goes beyond the existing literature and performs a detailed analysis of the effect of tooth geometry on the characteristics of LVR motors. It demonstrates the effect of three new airgap geometry parameters (tooth base fillet, tooth edge fillet, tooth tapering/dovetailing) on the characteristics of LVR motors. Published literature has not studied these geometric parameters.

The results of the study contribute to the following specific applications for both coupled and uncoupled LVR motors:

1. It presents a data management system and simulation driver for the characterization of a large number of LVR motor geometries and performs the characterization using finite element analysis (FEA).

2. It builds a nonlinear motor model based on FEA data and cubic spline interpolation of the data. The model relates input variables (displacement and phase currents) to corresponding outputs (force, coenergy, and phase flux linkages) using the stored data, which accounts for saturation and harmonics. The stored data serves an additional purpose by facilitating comparisons of the motors under study using three force production attributes. These attributes are the root mean square (RMS) averaged force (averaged over one tooth pitch), the RMS force density, and the ratio of RMS force density to copper loss.

3. Analysis of the data reveals the influence of tooth geometry on motor characteristics such as which geometry provides the maximum average force per mass (necessary for fast motion applications). Force production capability does not vary monotonically with tooth width or tooth fillet; instead, a particular tooth width and tooth fillet correspond to maximum average force (averaged over a tooth pitch). This observation provides valuable insight into geometry optimization.

4. It provides a basis for identifying which motor tooth geometries are more favorable given an intended application, be that an application tolerates force ripple, requires a constant force (minimum ripple), or minimizes heat dissipation. The study identifies a subset of tooth geometry shapes that are generally favorable, and it introduces a new expression for tooth shape factor to help in the analysis and design studies by constraining choices from the range of possible tooth geometries to this favorable subset.

CHAPTER 2

CONFIGURATION, TOOLS AND DATA MANAGEMENT

2.1 Introduction

This chapter presents this study's prerequisite foundational tools that aid the characterization and optimal commutation of linear variable reluctance (LVR) motors. The chapter is in three main sections. The first section describes the core tools used in finite element analysis; the second section describes the general construction of LVR motors, spatial discretization of the problem domain, and the resulting constraints imposed on the solver. The final section presents the setup of the simulation driver and its data management.

2.2 Solver Design

This section describes the system of differential equations that should be solved using the finite element method. Next, there is a presentation of the finite element formulation of the governing differential equations and a discussion of options for its programmatic implementation. Finally, the discussion presents the basis for solver selection and the configuration settings used in running the selected solver.

Using the finite element method to solve electromagnetics problems creates avenues for formulating several alternative approaches to the solution [51]. Applying the constraints of the problem to be addressed can results in approximations to Maxwell's equations that reduce the computational and memory requirements of the solution. This section discusses the differential equations, solved during the characterization and design optimization of LVR motors, and the physical conditions that motivate choices in approximation.

2.2.1 Governing Equations

2.2.1.1 Differential Form of Maxwell's Equations

Maxwell's equations in their differential form are a set of partial differential equations that describe the interaction of a pair of vector fields (electric, $\mathbb{E}$, and magnetic, $\mathbb{H}$) and their corresponding flux densities (electric, $\mathbb{D}$, and magnetic, $\mathbb{B}$). Equations 2.1 to 2.4 are the differential form of Maxwell's equations; there are equivalent integral forms that are used in other texts [51,52]. They relate electromagnetic field quantities to one another, and they make it convenient to study electromagnetic field phenomena due to their comprehensive, yet concise, nature [51]. ρ is the electric charge density, $\mathbb{J}$ is the electric current density, $\boldsymbol{r}$ describes the spatial domain and t is time. When subjected to appropriate boundary conditions and material properties for the domain of interest, they can be used to perform field simulation of electromagnetic problems [51,52].

$$\nabla \times \mathbb{H}(\boldsymbol{r}, t) = \mathbb{J}(\boldsymbol{r}, t) + \frac{\partial \mathbb{D}(\boldsymbol{r}, t)}{\partial t} \tag{2.1}$$

$$\nabla \times \mathbb{E}(\boldsymbol{r}, t) = -\frac{\partial \mathbb{B}(\boldsymbol{r}, t)}{\partial t} \tag{2.2}$$

$$\nabla \cdot \mathbb{B}(\boldsymbol{r}, t) = 0 \tag{2.3}$$

$$\nabla \cdot \mathbb{D}(\boldsymbol{r}, t) = \rho(\boldsymbol{r}, t) \tag{2.4}$$

$$\mathbb{B}(\boldsymbol{r}, t) = \mu_0[\mathbb{H}(\boldsymbol{r}, t) + \mathbb{M}(\boldsymbol{r}, t)] \tag{2.5a}$$

$$\mathbb{J}(\boldsymbol{r}, t) = \sigma[\mathbb{E}(\boldsymbol{r}, t) + \mathbb{E}_i(\boldsymbol{r}, t)] \tag{2.5b}$$

$$\mathbb{D}(\boldsymbol{r}, t) = \epsilon_0\mathbb{E}(\boldsymbol{r}, t) + \mathbb{P}(\boldsymbol{r}, t) \tag{2.5c}$$

Equations 2.5a to 2.5c are the *constitutive relations* and they spell out the effect of a material medium's conductivity (σ), permittivity (ϵ) and permeability (μ) on the electric and magnetic fields. $\mu_0 = 4\pi\times10^{-7}Hm^{-1}$ and $\epsilon_0 = 8.854\times10^{-12}Fm^{-1}$ are respectively the permeability and permittivity of vacuum. $\mathbb{M}$ is magnetization, $\mathbb{P}$ is polarization and $\mathbb{E}_i$ is the impressed electric field. Nonlinear material properties are defined in equations 2.6a to 2.6d. μ_r is relative permeability and ϵ_r is relative permittivity.

$$\epsilon = \epsilon_0\epsilon_r \tag{2.6a}$$

$$\mu = \mu_0\mu_r \tag{2.6b}$$

$$\epsilon_r = 1 + \frac{\mathbb{P}}{\mathbb{E}} \tag{2.6c}$$

$$\mu_r = 1 + \frac{\mathbb{M}}{\mathbb{H}} \tag{2.6d}$$

Equations 2.7a to 2.7c are the simplified constitutive relations obtained by substituting 2.6a to 2.6d into 2.5a to 2.5c and assuming $\mathbb{E}_i = 0$. The simplicity of these equations does not eliminate the complexity of the original equations. Rather, they compartmentalize the material effects in the material properties such that the existence of non-homogeneity and anisotropicity are reflected in the definition of material properties. Therefore, the properties of non-homogeneous materials are functions of the position, and those of anisotropic materials are tensors [51, 52].

$$\mathbb{B} = \mu \mathbb{H} \tag{2.7a}$$

$$\mathbb{J} = \sigma \mathbb{E} \tag{2.7b}$$

$$\mathbb{D} = \epsilon \mathbb{E} \tag{2.7c}$$

It is sometimes convenient to respresent equation 2.7a as 2.8 where $v = 1/\mu$. This form is preferred, and this document would adopt it henceforward.

$$\mathbb{H} = v \mathbb{B} \tag{2.8}$$

2.2.1.2 Static Magnetic Fields

Figure 2.1 shows the structure of a typical static magnetic field problem. A time-independent current, i, flows through the coil. The current density $\mathbb{J}_0$ generates independent/uncoupled electric, $\mathbb{E}$, and magnetic, $\mathbb{H}$, field intensities.

When the current density is time-independent, $\mathbb{J}_0 = \mathbb{J}_0(\boldsymbol{r})$, it generates a time-independent magnetic field intensity $\mathbb{H} = \mathbb{H}(\boldsymbol{r})$ and time-independent magnetic flux density $\mathbb{B} = \mathbb{B}(\boldsymbol{r})$.

It is practically acceptable under such conditions to assume $\partial/\partial t = 0$ in equations 2.1 and 2.3 and they take a new form expressed as follows.

$$\nabla \times \mathbb{H}(\boldsymbol{r}) = \mathbb{J}_0(\boldsymbol{r}) \tag{2.9}$$

$$\nabla \cdot \mathbb{B}(\boldsymbol{r}) = 0 \tag{2.10}$$

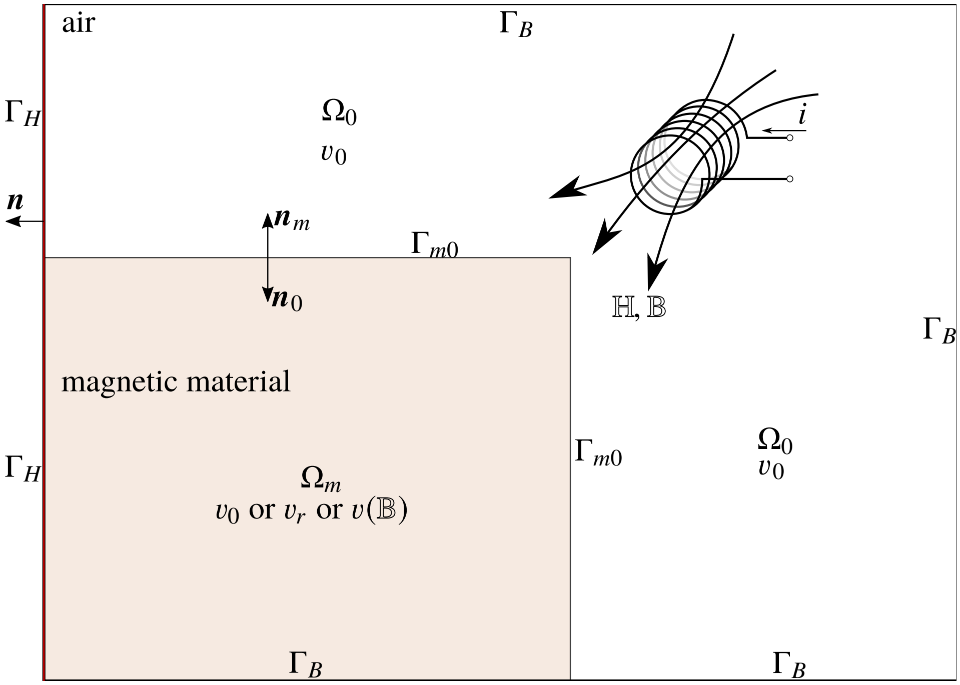

Figure 2.1 Basic components of static magnetic field problems. Ω_0 and Ω_m are respectively the volumes containing air and magnetic material. Γ_H is the field normal boundary which is also a symmetry plane for the problem. Γ_B is the flux tangential boundary which sets the limit of the air box.

Maxwell's equations take the static form as follows.

$$\boldsymbol{\nabla} \times \mathbb{H} = \mathbb{J}_0 \quad \text{in} \quad \Omega_0 \cup \Omega_m \tag{2.11}$$

$$\boldsymbol{\nabla} \cdot \mathbb{B} = 0 \quad \text{in} \quad \Omega_0 \cup \Omega_m \tag{2.12}$$

$$\mathbb{H} = \begin{cases} v_0 \mathbb{B} \quad \text{in} \quad \Omega_0 \\ v_0 v_r \mathbb{B} \quad \text{in linear} \quad \Omega_m \\ v(\mathbb{B})\mathbb{B} \quad \text{in nonlinear} \quad \Omega_m \end{cases} \tag{2.13}$$

The problem domain, $\Omega = \Omega_0 \cup \Omega_m$, is bounded by $\partial\Omega = \Gamma_H \cup \Gamma_B$. The normal component of $\mathbb{B}$ vanishes along Γ_B and the tangential component of $\mathbb{H}$ along Γ_H is a constant surface current density, $\mathbb{K}$. When $\mathbb{K} = 0$, Γ_H is a symmetry plane. Along the air-to-magnetic material boundary, Γ_{m0}, both the normal component of $\mathbb{B}$ and the tangential component of $\mathbb{H}$ are continuous. All of these conditions are formulated as shown in the below equations. b is an arbitrary constant, and it is often assumed to be $b = 0$ where the airbox surrounding the magnetic material is sufficiently large.

$$\mathbb{H} \times \boldsymbol{n} = \mathbb{K}, \quad \text{or} \quad \mathbb{H} \times \boldsymbol{n} = 0, \quad \text{on} \quad \Gamma_H \tag{2.14}$$

$$\mathbb{B} \cdot \boldsymbol{n} = -b, \quad \text{or} \quad \mathbb{B} \cdot \boldsymbol{n} = 0, \quad \text{on} \quad \Gamma_B \tag{2.15}$$

$$\mathbb{H}_0 \times \boldsymbol{n}_0 + \mathbb{H}_m \times \boldsymbol{n}_m = 0, \quad \text{and} \quad \mathbb{B}_0 \cdot \boldsymbol{n}_0 + \mathbb{B}_m \cdot \boldsymbol{n}_m = 0, \quad \text{on} \quad \Gamma_{m0} \tag{2.16}$$

The magnitude of current density is calculated using equation 2.17 and its direction is determined by the geometry of the coil. N is the number of turns of the coil and S_c is the cross-sectional area of the coil.

$$|\mathbb{J}_0| = \frac{Ni}{S_c} \tag{2.17}$$

2.2.1.3 Magnetic Vector Potential

For any vector function $\upsilon = \upsilon(\boldsymbol{r})$, $\boldsymbol{\nabla} \cdot \boldsymbol{\nabla} \times \upsilon$=0. Thus, the magnetic vector potential $\mathbb{A}$ is defined as follows to give $\mathbb{B}$ a value that satisfied equation 2.3.

$$\mathbb{B} = \boldsymbol{\nabla} \times \mathbb{A} \tag{2.18}$$

Substituting equation 2.18 into 2.11 (which satisfies equation 2.3 by definition) and 2.14 to 2.16 yields equations 2.19 to 2.22 which constitute the magnetic vector potential formulation of Maxwell's equations for both two-dimensional and three-dimensional problems.

$$\boldsymbol{\nabla} \times \left(\upsilon(\mathbb{A})\boldsymbol{\nabla} \times \mathbb{A}\right) = \mathbb{J}_0, \quad \text{in} \quad \Omega \tag{2.19}$$

$$\left(\upsilon(\mathbb{A})\boldsymbol{\nabla} \times \mathbb{A}\right) \times \boldsymbol{n} = \mathbb{K}, \quad \text{or} \quad \left(\upsilon(\mathbb{A})\boldsymbol{\nabla} \times \mathbb{A}\right) \times \boldsymbol{n} = 0, \quad \text{on} \quad \Gamma_H \tag{2.20}$$

$$\boldsymbol{\nabla} \cdot \left(\boldsymbol{n} \times \mathbb{A}\right) = b, \quad \text{or} \quad \boldsymbol{n} \times \mathbb{A} = 0, \quad \text{on} \quad \Gamma_B \tag{2.21}$$

$$\begin{gathered}\left(\upsilon(\mathbb{A}_0)\boldsymbol{\nabla} \times \mathbb{A}_0\right) \times \boldsymbol{n}_0 + \left(\upsilon(\mathbb{A}_m)\boldsymbol{\nabla} \times \mathbb{A}_m\right) \times \boldsymbol{n}_m = 0, \quad \text{and} \\ \left(\boldsymbol{n}_0 \times \mathbb{A}_0\right) + \left(\boldsymbol{n}_m \times \mathbb{A}_m\right) = 0, \quad \text{on} \quad \Gamma_{m0}\end{gathered} \tag{2.22}$$

Equation 2.19 has no unique three-dimensional solution [52], and uniqueness is achieved by enforcing the Coulomb gauge,

$$\nabla \cdot \mathbb{A} = 0, \quad \text{in} \quad \Omega \tag{2.23}$$

The three-dimensional solution of equation 2.19 has a limited scope of applications in electrical machine design (compared to the two-dimensional form) due to the complex magnetic core geometries of such machines. The high computational costs that result from the more significant problem size and the numerical problems resulting from the lack of uniqueness of equation 2.19. As a result, two-dimensional approximations of electrical machines (that assume infinitely long third axis) have a broader application. For these, the two-dimensional form of equation 2.19 is comparable to the three-dimensional form in accuracy [51]. It is, therefore, a common practice to design or characterize electrical machines using its two-dimensional model. Although the assumptions of two-dimensional analysis eliminate end-effects that affect design and characterization, the parameters that are extracted are useful to the engineering analysis of the machine [51]. Subsequently, a three-dimensional model of the electrical machine may be used to refine its design and validate already established parameters.

2.2.1.3.1 Two-Dimensional Problems

The two-dimensional case is derived from equation 2.19 by assuming $\mathbb{A}$ and $\mathbb{J}$ are entirely in a third axis (z-directed in our case). Additionally, the material properties, cross-sectional geometry, and source functions are assumed to be translationally symmetric along the z-axis. Consequently, the fields and fluxes are independent of the z-axis; $\mathbb{H}$ and $\mathbb{B}$ are constrained to the x-y plane. The Coulomb gauge (equation 2.23) is automatically satisfied in the two-dimensional case since the sources, and the magnetic vector potential term is independent of the z-axis.

$$\mathbb{A} = A_z(x, y)\mathbf{e}_z \tag{2.24a}$$

$$\mathbb{J} = J_z(x, y)\mathbf{e}_z \tag{2.24b}$$

$$\mathbb{H} = H_x(x, y)\mathbf{e}_x + H_y(x, y)\mathbf{e}_y \tag{2.24c}$$

$$\mathbb{B} = B_x(x, y)\mathbf{e}_x + B_y(x, y)\mathbf{e}_y \tag{2.24d}$$

Translational symmetry in the z-axis by definition means that A_z and B_z are both constant in $\mathbf{e}_z$. Substituting equation 2.24a into 2.18 provides a means to calculate $\mathbb{B}$ in equation 2.25.

$$\mathbb{B} = \boldsymbol{\nabla} \times \mathbb{A} = \frac{\partial A_z}{\partial y}\mathbf{e}_x - \frac{\partial A_z}{\partial x}\mathbf{e}_y \tag{2.25}$$

Finally, substituting equation 2.25 into 2.19, computing the vector operations and eliminating the unit vector yields equation 2.26.

$$\frac{\partial}{\partial x}\left(v\left(\left|\nabla A_z\right|\right)\frac{\partial A_z}{\partial x}\right) + \frac{\partial}{\partial y}\left(v\left(\left|\nabla A_z\right|\right)\frac{\partial A_z}{\partial y}\right) = -J_z, \quad \text{in} \quad \Omega \tag{2.26}$$

It has the form of the nonlinear Poisson equation and can, therefore, be written in the more concise notation in equation 2.27. The boundary conditions are the same as those specified in equations 2.20 to 2.22. After assuming $b = 0$ and $\mathbb{K} = 0$, the Dirichlet and Neumann boundary conditions can be simplified as equations 2.28 to 2.29.

$$\boldsymbol{\nabla} \cdot \left(v\left(\left|\nabla A_z\right|\right) \nabla A_z \right) = -J_z, \quad \text{in} \quad \Omega \tag{2.27}$$

$$\frac{\partial A_z}{\partial n_z} = 0, \quad \text{on} \quad \Gamma_H \tag{2.28}$$

$$A_z = 0, \quad \text{on} \quad \Gamma_B \tag{2.29}$$

The core material for the electric motors used in this study can be modeled as a nonlinear isotropic material. In this case, the reluctivity for nonlinear isotropic materials can be calculated directly from equation 2.30.

$$v\left(\mathbb{B}\right) = v\left(|\mathbb{B}|\right) = v\left(\left|\nabla A_z\right|\right) \tag{2.30}$$

2.2.1.3.2 Three-Dimensional Problems

These can be solved either by replacing equation 2.19 with a functional that implicitly enforces the Coulomb gauge (gauged magnetic vector potential formulation) or using a numerical approach that is insensitive to the Coulomb gauge (ungauged magnetic vector potential formulation). The former has a more widespread application in literature [51–53], and it would be the focus of this section.

The gauged magnetic vector potential formulation can be obtained by adding a Coulomb gauge term to equation 2.19 as in equation 2.31 and applying the corresponding boundary conditions in equations 2.31 to 2.33 [52].

$$\boldsymbol{\nabla} \times \left(v(\mathbb{A}) \boldsymbol{\nabla} \times \mathbb{A} \right) - \nabla\left(v(\mathbb{A}) \boldsymbol{\nabla} \cdot \mathbb{A} \right) = \mathbb{J}, \quad \text{in} \quad \Omega \tag{2.31}$$

$$\big(v(\mathbb{A})\boldsymbol{\nabla}\times\mathbb{A}\big)\times\boldsymbol{n}=\mathbb{K},\quad\text{or}\quad\mathbb{A}\cdot\boldsymbol{n}=0,\quad\text{on}\quad\Gamma_H \tag{2.32}$$

$$\boldsymbol{\nabla}\cdot\big(\boldsymbol{n}\times\mathbb{A}\big)=b,\quad\text{or}\quad\boldsymbol{\nabla}\cdot\mathbb{A}=0,\quad\text{on}\quad\Gamma_B \tag{2.33}$$

2.2.2 Finite Element Formulation

2.2.2.1 Newton's Method

The magnetic vector potential formulation of the static magnetic field problem in two dimensions (equations 2.27 to 2.29) can be solved using Newton's method by first computing the $(n+1)^{th}$ approximate solution from the n^{th} one.

For the two-dimensional case, the functional to be solved using Newton's method is:

$$F(A_z)=-\boldsymbol{\nabla}\cdot\left(v\left(\left|\nabla A_z\right|\right)\nabla A_z\right)-J_z \tag{2.34}$$

Defining A_z^n as the n^{th} approximate solution, and δA_z^n as the n^{th} increment, the $(n+1)^{th}$ approximate solution (A_z^{n+1}) can be computed using the below equations. A damping parameter, a^n, is often used to improve the global convergence behavior.

$$F'(A_z^n,\delta A_z^n)=-F(A_z^n) \tag{2.35}$$

$$A_z^{n+1}=A_z^n+a^n\delta A_z^n \tag{2.36}$$

Where, for any positive rational number ξ:

$$F'(A_z,\delta A_z)=\lim_{\xi\to 0}\frac{F(A_z+\xi\delta A_z)-F(A_z)}{\xi} \tag{2.37}$$

Substituting equation 2.34 into 2.35 and performing the necessary mathematical operations yields the strong form of the magnetic vector potential formulation in equation 2.38. The solution for the equation starts by repeatedly solving for δA_z^n in equation 2.38 and substituting the result into equation 2.36 until $\delta A_z^n < tol$. tol is the tolerance that prescribes the accuracy of the expected solution. In order to enforce the essential boundary conditions, it is assumed that the boundary conditions are already satisfied for $A_z^n \; \forall \; n > 0$ and thus $\delta A_z^n = 0 \; \forall \; n > 0$. Therefore, enforcing 2.29 at $n = 0$ yields $\delta A_z^0 = 0$. It is also common to start with $A_z^0 \equiv 0$; see equation 2.39.

$$-\boldsymbol{\nabla}\cdot\left(\upsilon\left(\left|\nabla A_z^n\right|\right)\nabla\delta A_z^n\right)-\boldsymbol{\nabla}\cdot\left(\upsilon'\left(\left|\nabla A_z^n\right|\right)\left(\nabla A_z^n\cdot\nabla\delta A_z^n\right)\frac{\nabla A_z^n}{\left|\nabla A_z^n\right|}\right)=\boldsymbol{\nabla}\cdot\left(\upsilon\left(\left|\nabla A_z^n\right|\right)\nabla A_z^n\right)+J_z \quad \text{in} \quad \Omega \tag{2.38}$$

$$\begin{aligned} A_z^0 &\equiv 0, \quad \text{in} \quad \Omega \\ \delta A_z^n &= 0, \quad \forall \quad n \geq 0, \quad \text{on} \quad \Gamma_B \end{aligned} \tag{2.39}$$

An alternative approach to solving the two-dimensional magnetic vector potential formulation of the static magnetic field is to minimize the stored magnetic energy, $W = W(\mathbb{A}) = W\left(A_z\right)$, in the following functional.

$$F(A_z) = \int \frac{\partial W\left(A_z\right)}{\partial A_z} \mathrm{d}\Omega - \int J_z \mathrm{d}\Omega \tag{2.40}$$

$$W(\mathbb{A}) = \int \mathbb{H} \cdot \mathrm{d}\mathbb{B} = \int \upsilon(\mathbb{B})\mathbb{B} \cdot \mathrm{d}\mathbb{B} \tag{2.41}$$

Substituting equation 2.41 into the first term of equation 2.40.

$$\frac{\partial W\left(A_z\right)}{\partial A_z} = \frac{\partial}{\partial A_z} \int_0^B \upsilon(b) b \mathrm{d}b \tag{2.42}$$

Where $B = \left|\mathbb{B}\right| = \left|\nabla A_z\right|$, and b is a dummy variable for integration. Recasting reluctivity as a function of $B^2 = \left|\nabla A_z\right|^2$ and applying chain rule of differentiation yields

$$\frac{\partial W(A_z)}{\partial A_z} = \frac{1}{2}\frac{\partial}{\partial A_z}\int_0^{|A_z|^2} v(b^2)\mathrm{d}(b^2) = \frac{1}{2}v\left(\left|\nabla A_z\right|^2\right)\frac{\partial\left(\left|\nabla A_z\right|^2\right)}{\partial A_z} \tag{2.43}$$

Substituting equation 2.43 into equation 2.40 yields the functional to be minimised using Newton's method in equation 2.44. Differentiating the functional, results in the Jacobian in equation 2.45, and subsequently with change of variable the form changes to 2.46.

$$F(A_z) = \int\left(\frac{1}{2}v\left(\left|\nabla A_z\right|^2\right)\frac{\partial\left(\left|\nabla A_z\right|^2\right)}{\partial A_z} - J_z\right)\mathrm{d}\Omega \tag{2.44}$$

$$F'(A_z) = \frac{1}{2}v\left(\left|\nabla A_z\right|^2\right)\frac{\partial^2\left(\left|\nabla A_z\right|^2\right)}{\partial A_z^2} + \frac{1}{2}\frac{\mathrm{d}v\left(\left|\nabla A_z\right|^2\right)}{\mathrm{d}\left(\left|\nabla A_z\right|^2\right)}\left(\frac{\partial\left(\left|\nabla A_z\right|^2\right)}{\partial A_z}\right)^2 \tag{2.45}$$

$$F'(A_z, \delta A_z) = 2v\left(\left|\nabla A_z\right|^2\right)\left(\nabla\delta A_z\cdot\nabla\delta A_z\right) + 2\frac{\mathrm{d}v\left(\left|\nabla A_z\right|^2\right)}{\mathrm{d}\left(\left|\nabla A_z\right|^2\right)}\left(\nabla A_z\cdot\nabla\delta A_z\right)^2 \tag{2.46}$$

The Newton update vector for the n^{th} iteration is therefore attained in equation 2.47 by substituting equations 2.44 and 2.47 into equation 2.35.

$$\begin{aligned} 2v\left(\left|\nabla A_z^n\right|^2\right)\left(\nabla\delta A_z^n\cdot\nabla\delta A_z^n\right) + 2\frac{\mathrm{d}v\left(\left|\nabla A_z^n\right|^2\right)}{\mathrm{d}\left(\left|\nabla A_z^n\right|^2\right)}\left(\nabla A_z^n\cdot\nabla\delta A_z^n\right)^2 \\ = -\frac{1}{2}v\left(\left|\nabla A_z^n\right|^2\right)\frac{\partial\left(\left|\nabla A_z^n\right|^2\right)}{\partial A_z^n} + J_z \quad \text{in} \quad \Omega \end{aligned} \tag{2.47}$$

For three-dimensional problems, the functional to be minimized using Newton's method is derived from equation 2.31 in

$$F(\mathbb{A}) = \boldsymbol{\nabla} \times \big(v(\mathbb{A})\boldsymbol{\nabla} \times \mathbb{A}\big) - \nabla\big(v(\mathbb{A})\boldsymbol{\nabla} \cdot \mathbb{A}\big) + \mathbb{J}, \quad \text{in} \quad \Omega \tag{2.48}$$

$F(\mathbb{A}, \delta\mathbb{A})$ is often calculated using automatic differentiation using automatic differentiation by the operator overloading using the chain rule or the complex number method in equation 2.49.

$$F'(\mathbb{A}, \delta\mathbb{A}) = \mathrm{Im}\left(\frac{F(\mathbb{A} + j\xi\delta\mathbb{A}) - F(\mathbb{A})}{\xi}\right) \tag{2.49}$$

2.2.2.2 Weighted Residual Method

The weighted residual method approaches the solution to the problems such as those presented in equations 2.38, 2.47 and 2.48 by replacing the original function ($\mathbb{A}$ or A_z) with an approximate solution U that satisfies the Dirichlet boundary conditions exactly (these methods automatically meet the Neumann boundary conditions without the need to enforce them). It permits a reduction of the differentiability requirements on U and thus better support for less smooth solutions to the given problem.

For a typical element domain, the following steps are used to attain the weighted residual form. The differential equation is first converted to *weighted-integral form* by multiplying the differential equation by an arbitrary weight function (ϕ) and integrating over the entire problem domain. Next, the differentiation in the weighted-integral form is distributed between ϕ and U to reduce the differentiability requirements on U. Finally, the boundary conditions are enforced to give the *weighted residual form*.

The weighted integral form for the Poisson form of the two-dimensional magnetic vector potential problem is obtained as follows by multiplying equation 2.38 by a weight function ϕ.

$$\begin{aligned} -\int_{\Omega}\phi\boldsymbol{\nabla}\cdot\left(v\left(\left|\nabla A_z^n\right|\right)\nabla\delta A_z^n\right)-\int_{\Omega}\phi\boldsymbol{\nabla}\cdot\left(v'\left(\left|\nabla A_z^n\right|\right)\left(\nabla A_z^n\cdot\nabla\delta A_z^n\right)\frac{\nabla A_z^n}{\left|\nabla A_z^n\right|}\right) \\ =\int_{\Omega}\phi\boldsymbol{\nabla}\cdot\left(v\left(\left|\nabla A_z^n\right|\right)\nabla A_z^n\right)+\int_{\Omega}\phi J_z \end{aligned} \tag{2.50}$$

Distributing the differentiation as evenly as possible over δA_z and ϕ, and imposing the Dirichlet boundary condition of $\phi = 0$ results in

$$\begin{aligned} \int_{\Omega}\nabla\phi\cdot\left(v\left(\left|\nabla A_z^n\right|\right)\nabla\delta A_z^n\right)\mathrm{d}\Omega+\int_{\Omega}\nabla\phi\cdot\left(v'\left(\left|\nabla A_z^n\right|\right)\left(\nabla A_z^n\cdot\nabla\delta A_z^n\right)\frac{\nabla A_z^n}{\left|\nabla A_z^n\right|}\right)\mathrm{d}\Omega \\ =\int_{\Omega}\nabla\phi\cdot\left(v\left(\left|\nabla A_z^n\right|\right)\nabla A_z^n\right)\mathrm{d}\Omega+\int_{\Omega}\phi J_z\mathrm{d}\Omega \end{aligned} \tag{2.51}$$

Similarly, the weighted integral form of the minimum stored magnetic energy functional approach to the two-dimensional magnetic vector formulation of static magnetic fields is

$$\begin{aligned} \int_{\Omega}\phi\left(2v\left(\left|\nabla A_z^n\right|^2\right)\left(\nabla A_z^n\cdot\nabla\delta A_z^n\right)\right)\mathrm{d}\Omega+\int_{\Omega}\phi\left(2\frac{\mathrm{d}v\left(\left|\nabla A_z^n\right|^2\right)}{\mathrm{d}\left(\left|\nabla A_z^n\right|^2\right)}\left(\nabla A_z^n\cdot\nabla\delta A_z^n\right)^2\right)\mathrm{d}\Omega \\ =-\int_{\Omega}\phi\left(\frac{1}{2}v\left(\left|\nabla A_z^n\right|^2\right)\frac{\partial\left(\left|\nabla A_z^n\right|^2\right)}{\partial A_z^n}\right)\mathrm{d}\Omega+\int_{\Omega}\phi J_z\mathrm{d}\Omega \end{aligned} \tag{2.52}$$

Finally, the weighted integral form of the three-dimensional magnetic vector potential formulation is in equation 2.53. It uses the vector form of the weight function $\boldsymbol{\phi}$ to perform the aforementioned operations, and impose the Dirichlet boundary conditions of $\boldsymbol{\phi} \cdot \boldsymbol{n} = 0$ or $\boldsymbol{n} \times \boldsymbol{\phi} = 0$.

$$F(\mathbb{A}) = \int_{\Omega} \left(\boldsymbol{\nabla} \times \boldsymbol{\phi}\right) \cdot \left(\upsilon(\mathbb{A}) \boldsymbol{\nabla} \times \mathbb{A}\right) \mathrm{d}\Omega - \int_{\Omega} \left(\boldsymbol{\nabla} \cdot \boldsymbol{\phi}\right) \left(\upsilon(\mathbb{A}) \boldsymbol{\nabla} \cdot \mathbb{A}\right) \mathrm{d}\Omega + \int_{\Omega} \boldsymbol{\phi} \cdot \mathbb{J} \mathrm{d}\Omega \tag{2.53}$$

There are three approaches to attaining the weighted residual form of equations 2.38, 2.47 and 2.48 from their weighted integral forms in equations 2.51 to 2.53 respectively. The *direct form* is derived using methods such as *Bubnov-Galerkin*, *Moment*, or *finite difference*. These methods directly apply the weight function and an approximating magnetic vector potential (without first reducing the differentiability requirements) and, as such, required double differentiation of the weight function. *Inverse* methods such as *Trefftz* and the *boundary element* methods use the inverse form of the partial differential equations. They thus derive the solution from the weight function instead of an approximating magnetic potential. This document focuses on the *weak form*, which is the basis for the Finite Element Method.

2.2.2.2.1 The Weak Form

The approach to the Finite Element Method used in this study depends on the weighted residual weak form of the original equations attained using the *Galerkin method*. An approximate solution of the magnetic vector potential, and the current density are defined for both 2D and 3D as follows.

$$\delta A_z^n = \sum_{m=1}^{M} \phi_m U_m \tag{2.54}$$

$$J_z = \sum_{m=1}^{M} \phi_m J_m \tag{2.55}$$

$$\mathbb{A} = \sum_{m=1}^{M} \boldsymbol{\phi}_m \cdot \mathbb{U}_m \tag{2.56}$$

$$\mathbb{J} = \sum_{m=1}^{M} \boldsymbol{\phi}_m \cdot \mathbb{J}_m \tag{2.57}$$

Substituting equations 2.54 and 2.55 into 2.51 results in the weak form of the two-dimensional magnetic vector potential formulation.

$$\begin{aligned}\sum_{m=1}^{M}\sum_{n=1}^{N}\left[\int_{\Omega}\nabla\phi_m\cdot\left(v\left(\left|\nabla A_z^n\right|\right)\nabla\phi_n\right)\mathrm{d}\Omega+\int_{\Omega}\nabla\phi_m\cdot\left(v'\left(\left|\nabla A_z^n\right|\right)\left(\nabla A_z^n\cdot\nabla\phi_n\right)\frac{\nabla A_z^n}{\left|\nabla A_z^n\right|}\right)\mathrm{d}\Omega\right]U_n \\ =\sum_{m=1}^{M}\left[\int_{\Omega}\nabla\phi_m\cdot\left(v\left(\left|\nabla A_z^n\right|\right)\nabla A_z^n\right)\mathrm{d}\Omega+\int_{\Omega}\phi_m J_m\mathrm{d}\Omega\right]\end{aligned} \tag{2.58}$$

Similarly, the weak form of the minimum stored magnetic energy and three-dimensional formulation are respectively as follows.

$$\begin{aligned}\sum_{m=1}^{M}\sum_{n=1}^{N}\left[\int_{\Omega}\phi_m\left(2v\left(\left|\nabla A_z^n\right|^2\right)\left(\nabla A_z^n\cdot\nabla\phi_n\right)\right)\mathrm{d}\Omega+\int_{\Omega}\phi_m\left(2\frac{\mathrm{d}v\left(\left|\nabla A_z^n\right|^2\right)}{\mathrm{d}\left(\left|\nabla A_z^n\right|^2\right)}\left(\nabla A_z^n\cdot\nabla\phi_n\right)^2\right)\mathrm{d}\Omega\right]U_n \\ =\sum_{m=1}^{M}\left[-\int_{\Omega}\phi_m\left(\frac{1}{2}v\left(\left|\nabla A_z^n\right|^2\right)\frac{\partial\left(\left|\nabla A_z^n\right|^2\right)}{\partial A_z^n}\right)\mathrm{d}\Omega+\int_{\Omega}\phi_m J_z\mathrm{d}\Omega\right]\end{aligned} \tag{2.59}$$

$$\begin{aligned}F(\mathbb{A})=\sum_{m=1}^{M}\sum_{n=1}^{N}\left[\int_{\Omega}\left(\boldsymbol{\nabla}\times\boldsymbol{\phi}_m\right)\cdot\left(v(\mathbb{A}_m)\boldsymbol{\nabla}\times\boldsymbol{\phi}_n\right)\mathrm{d}\Omega-\int_{\Omega}\left(\boldsymbol{\nabla}\cdot\boldsymbol{\phi}_m\right)\left(v(\mathbb{A}_m)\boldsymbol{\nabla}\cdot\boldsymbol{\phi}_n\right)\mathrm{d}\Omega\right]\mathbb{U}_n \\ +\sum_{m=1}^{M}\left[\int_{\Omega}\boldsymbol{\phi}_m\cdot\mathbb{J}_m\mathrm{d}\Omega\right]\end{aligned} \tag{2.60}$$

2.2.2.3 Selection of Weight Functions

Third-order Lagrange elements belong to an element space $V_h \subset H^1 \subset \Omega$. H^1 is the Sobolev element space, and it is sufficiently dense enough to find the correct solution for both of the two-dimensional magnetic vector potential formulations of the static magnetic field.

For the three-dimensional problem, however, H^1 is not dense enough in Ω for the norm $||\cdot||_\Omega = ||\cdot||_{H_{curl} \cap H_{div}}$ and equation 2.60 may not converge to the correct solution when using Lagrange elements [54]. $H_{curl} \subset \Omega$ and $H_{div} \subset \Omega$ are respectively the subdomains where valid curls and divergences respectively exist. Hence for the three-dimensional formulation, Nedelec elements may be used [55] to ensure convergence to the right solution.

2.2.3 Solver Selection and Configuration

The three variations of the weighted residual weak form of the magnetic vector potential formulation of the static magnetic field problem have been summarized in equations 2.58 to 2.60. Two software systems were considered in solving the two-dimensional and three-dimensional problems in the characterization and design optimization of linear variable reluctance (LVR) motors.

2.2.3.1 deal.II

Differential Equations Analysis Library II (deal.II) is a c++ software library that provides a suite of computational tools for solving differential equations using adaptive finite elements. It has state-of-the-art programming techniques and a modern object-oriented application programmer interface (API). The core features of deal.II are as follows [55].

- Template-based support for both two-dimensional and three-dimensional geometry, reducing code duplication.
- Local and global h, p, and hp grid refinement and integrated transfer of solution from the coarse to the fine grid.
- Numerical integration with various finite elements, including Lagrange elements of any order, continuous and discontinuous, and Nedelec elements of any order.
- Parallelization that scales up to a 16k processor using Intel's Threading Building Blocks (TBB) or Message Passing Interface (MPI).
- Interface with linear solvers such as Trilinos, PETSc, and METIS.
- Open source.

2.2.3.2 MagNet®

MagNet® is a Windows-based proprietary software the is built and maintained by Mentor Graphics. It uses the finite element method to solve Maxwell's equations for two-dimensional and three-dimensional electric machine design. These are the core features of the MagNet® [53].

- It uses the magnetic vector potential formulation of Maxwell's equations, which is more suited for electric machine design.
- Magnetostatic, transient, and time-harmonic analysis in both two- and three-dimensions.
- Multithreaded, supporting up to 6 cores simultaneously. License limitation to a maximum of 12 cores.

- Integrated meshing tool with mesh movement and adaptation for both two- and three-dimensional meshes.
- Material library with the necessary magnetic, electrical, and thermal characteristics.
- Integrated scripting through windows ActiveX® API through VBScript, JScript, or PowerShell®.
- Automatic post-processing and presentation of quantities of interest such as forces and flux linkages.

Although deal.II is more scalable than MagNet®, the amount of development effort required to benefit from this advantage is high, resulting in high lead time for delivery. It was, therefore, earlier decided to use MagNet® for this study, while ongoing work to develop deal.II for future studies continues. The rest of the discussions for this section would be about MagNet®.

2.3 Motor Design Specification

Figure 1.1 shows transverse views of the magnetically uncoupled and coupled configurations of the linear variable reluctance (LVR) motor under consideration. See also [10–13]. Each has a longitudinal flux three-phase configuration with an equal number of toothed poles on each phase. The motor coils are series-connected and concentrated on the poles of the translator (moving assembly); there are none on the stator. A phase-to-phase offset of $\frac{1}{3}p_t$ provides misalignment, although tooth pitch (p_t) is constant on all poles. Hence, the minimum step size of the motor is $\frac{1}{3}p_t$. The doubly-salient construction of the poles results in zero net normal forces, and this construction is favored over a single-sided construction [1].

For the coupled configuration, the winding direction for the three phases is identical, and each phase's poles serve as the return path for magnetic flux of adjacent phases, causing significant magnetic coupling of the phase fluxes. The high magnetic coupling results in comparable magnitudes of both mutual and self-inductances of the phase windings; nonlinear modeling of the motor must consider simultaneous excitation in all three-phase coils.

In the uncoupled configuration, phase fluxes have a negligible mutual coupling, since phase windings are concentrated on pairs of poles with alternating/opposing winding directions. Consequently, the minimum number of poles needed to construct the uncoupled LVR motor is six;

in contrast, the coupled configuration requires a minimum of three poles. Figures 1.1a and 1.1b respectively have these minimal configurations, with phase 2 teeth in full alignment. Because the phase flux paths are effectively magnetically isolated from one another, analysis using single-phase excitation (phase 1) for the uncoupled configuration is permissible. Force and flux linkage outputs for phases 2 and 3 are obtained from phase 1 results by shifting; this predictable fact was evident in initial finite element runs. As an additional consequence, the sign of the phase excitation current does not affect the direction of thrust. Using only positive excitation currents to drive the motor is therefore sufficient.

The LVR motors used in this study have the following common characteristics.

- planar air gaps between the active translator and the passive stator.
- concentrated windings, unlike the distributed ones of synchronous variable reluctance motors.
- longitudinal flux (parallel to the direction of mechanical motion)
- three phases of excitation.

2.3.1 Construction

Figure 2.2 shows the typical components used in the construction of both coupled (Figure 2.2b) and uncoupled (Figure 2.2a) configurations of LVR motors. A typical LVR motor has two moving assemblies (translators), and one stationary core (stator) sandwiched between the two. The stator has translationally periodic teeth on both sides (upper and lower) and facing corresponding moving assemblies with an air gap separating the stator teeth from the teeth of the moving assembly. Gaps called valleys separate the teeth.

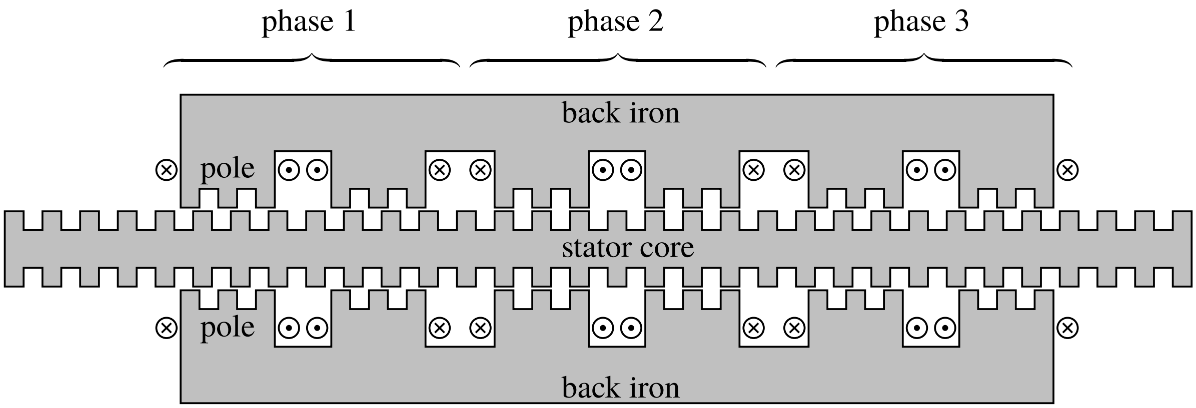

(a) Uncoupled configuration

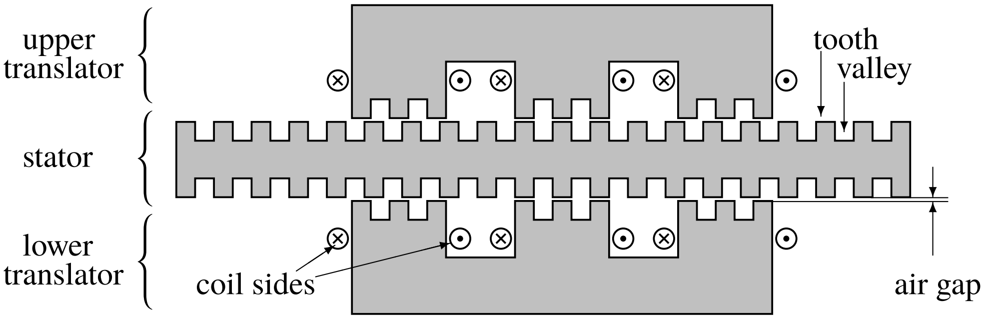

(b) Coupled configuration

Figure 2.2 Common Structural Components of Coupled and Uncoupled Linear Variable Reluctance Motors

Each of the moving assemblies consists of toothed poles mounted on a back iron. Teeth on corresponding poles in the upper and lower moving assemblies are identical and aligned, ensuring symmetry about the stator axis.

The phase windings are mounted on each pole, making the translator the active part responsible for generating the magnetic flux in the motor's operation. Consequently, the number of poles is a multiple of the number of phases; there are three phases in this study, numbered one to three in the positive x direction. For the coupled LVR motor that relies on shared magnetic paths, the minimum number of poles is three (one for each phase), and phase coils are wound in the same

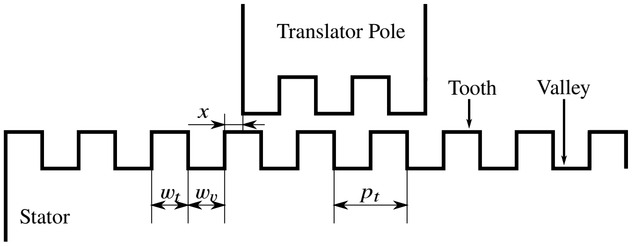

Figure 2.3 Parameters that define airgap geometry

direction for each phase. For the uncoupled LVR motor with noninteracting, the minimum number of poles is six (one pair for each phase), and phase coils are wound such that is pair's windings run in the opposite direction of one another. As a result, there is a closed flux path for each pole pair that is noninteracting and magnetically "uncoupled" from the rest of the poles.

The uncoupled motor represents typical (i.e., switched) linear and rotary variable reluctance motors while the coupled motor exhibits features of both switched and synchronous varieties of variable reluctance motors.

2.3.2 Motor Geometric Characteristics

Table 2.1 describes the common characteristics of all motors used in this study. A typical design has n_p poles on each phase and $n \geq 1$ teeth on each pole. $n_p \geq 1$ for the coupled configuration, and $n_p \geq 2$ for the uncoupled configuration. The n teeth on each pole have the same width (w_t) and separated by a constant tooth pitch (p_t); stator teeth have an identical configuration. p_t is the distance from the beginning of a tooth to the start of an adjacent tooth on the same pole. The valley width (w_v) is the distance from the end of one tooth to the beginning of the next tooth

Table 2.1 Common Design Parameters of Linear Variable Reluctance Motors

Motor Parameter	Value
Device depth (l_d)	$50mm$
Tooth pitch (p_t)	$10mm$
Air gap length (l_g)	$\frac{1}{4}mm$
Core material	M19 Steel
Tooth length (l_t)	$5mm$
Pole length (l_p)	$10mm$
Back iron length (l_b)	$15mm$
Winding material	Copper
Winding conductivity	$5.77 \times 10^7 Sm^{-1}$
Winding wire gauge	$18AWG$
Teeth per pole (n)	3
Pole-to-pole tooth pitches (l_m)	4
Poles per phase (n_p)	$[1, 2] \in \mathbb{Z}$
Tooth shape factor (α)	$[0, 1] \in \mathbb{R}$
Tooth edge fillet (f_{te})	$[0, 1] \in \mathbb{R}$
Tooth base fillet (f_{tb})	$[0, 1] \in \mathbb{R}$
Pole fillet (f_p)	$[0, 1] \in \mathbb{R}$
Tooth edge scaling factor (δ_{te})	$[0, 2] \in \mathbb{R}$
Excitation Current (i)	$[-15, 15]A$

on the same pole. Eq. (2.61) and figure 2.3 the relationship between p_t, w_t and w_v.

$$p_t = w_t + w_v \tag{2.61}$$

The spacing between adjacent poles is specified as $m \geq n$ tooth pitches with a minimum of one valley width (w_v) available when $m = n$. Varying m also changes the pole pitch, which in turn alters the maximum number of feasible turns that the motor coils can carry.

The spacing from the beginning of one phase to the start of an adjacent phase (p_{ph}) is based on the characteristics as mentioned earlier and chosen to ensure the $\frac{1}{3}p_t$ offset between teeth of adjacent phases.

$$p_{ph} = p_t\left[n(n_p - 1) + m + \frac{1}{3}\right] - w_v(n_p - 1) \tag{2.62}$$

A tooth shape factor (α) expresses w_t and w_v as functions of α and p_t as follows. The minimum feasible w_t (when $\alpha = 0$) is $\frac{1}{3}p_t$, and the maximum feasible w_t (when $\alpha = 1$) is $\frac{1}{2}p_t$. Because α is a dimensionless quantity with range $[0, 1]$, it is independent of the dimensions of the motor, and it only indicates the shape of the teeth.

The tooth width (w_t) and valley width (w_v) can be expressed as fractions of p_t a using tooth shape factor (α).

$$w_t = p_t(2 + \alpha)/6 \tag{2.63a}$$

$$w_v = p_t(4 - \alpha)/6 \tag{2.63b}$$

In addition to varying the tooth width, the sharp corners at the bases and edges of teeth can be smoothed by rounding them using fillets. The radii of the respective fillets are defined as $R_{f_{te}}$ and $R_{f_{tb}}$. The maximum fillet radius for rounding the tooth edge or base varied with the tooth width and may be limited by tooth length (l_t) in cases where $l_t < w_t$. These geometric properties were defined in terms of a tooth edge fillet factor ($f_{te} \in [0, 1]$) and a tooth base fillet factor ($f_{tb} \in [0, 1]$)

respectively and applied to the motor's tooth geometry as follows.

$$R_{f_{te}} = 0.5 f_{te} \times \begin{cases} l_t, & l_t > w_t \\ w_t, & w_t \geq l_t \end{cases} \tag{2.64}$$

$$R_{f_{tb}} = 0.5 f_{tb} \times \begin{cases} l_t, & l_t > w_t \\ w_t, & w_t \geq l_t \end{cases} \tag{2.65}$$

Filleting has the effect of reducing magnetic saturation in tooth corners. Still, edge filleting has the effect of increasing air gap length, hence the need to study which fillet when applied gives favorable force production. Another filleting factor ($f_p \in [0, 1]$) was similarly applied to the pole bases of the translator to determine if introducing fillets in the pole would affect the saturation effects of the motor. The pole fillet has the effect of increasing the available space for placing phase windings and could increase their total flux generated. However, the number of turns of the motor phase windings was not modified to include this effect since the study was only focused on determining if the narrowing of the pole widths caused by filleting could negatively impact force production.

Angulation allowed the motor's teeth to taper or dovetail by applying a scaling factor ($\delta_{te} \in [0, 2]$) to the tooth edge while leaving the tooth base width at w_t. The width of the tooth's edge, therefore, becomes $\delta_{te} w_t$. The angulation factor has the effect of introducing tooth edge widths less than $\frac{1}{3} p_t$, which have positions of zero force due to a lack of interaction between opposing teeth. Angulation can also produce tooth edge widths greater than $\frac{1}{2} p_t$, which have areas of zero instantaneous force due to complete alignment of all opposing teeth. However, it also has the effect of increasing or reducing reluctance in the air gap, which could affect saturation effects in the motor and force output.

The motor's geometric characteristics affect the mechanical and magnetic features of the motor. Insight into the fundamental magnetic properties of the motor, namely flux linkage and instantaneous force, and the influence on tooth geometry on these properties can be gained using simplified analytical expressions based on equivalent magnetic circuit analysis. Such analyses, as shown in [10,13], are generally carried out under the assumption of linear magnetics and harmonics. Additional insight can gained from [14,56,57]. Figure 2.4 shows a subset of the tooth geometries that would be studied in subsequent chapters.

2.4 Simulation Setup

The 2D magnetostatic solver in MagNet®, an electromagnetic field simulation software, was used to run all the cases for all motor configurations. A large number of cases was considered, and this required an effort to minimize spurious variation between cases introduced by human error. A data management architecture was designed and implemented to streamline the generation, processing, and storage of data.

Although the motor is double-sided, only one side is modeled in simulation to take advantage of motor symmetry and reduce computational cost. Discretization error was minimized by performing a sensitivity analysis of the motor models in FEA to ensure that the meshes were sufficiently large and the geometry adequately resolved. The final mesh and solver configuration parameters were selected after gradual improvements to the mesh and solver configuration until

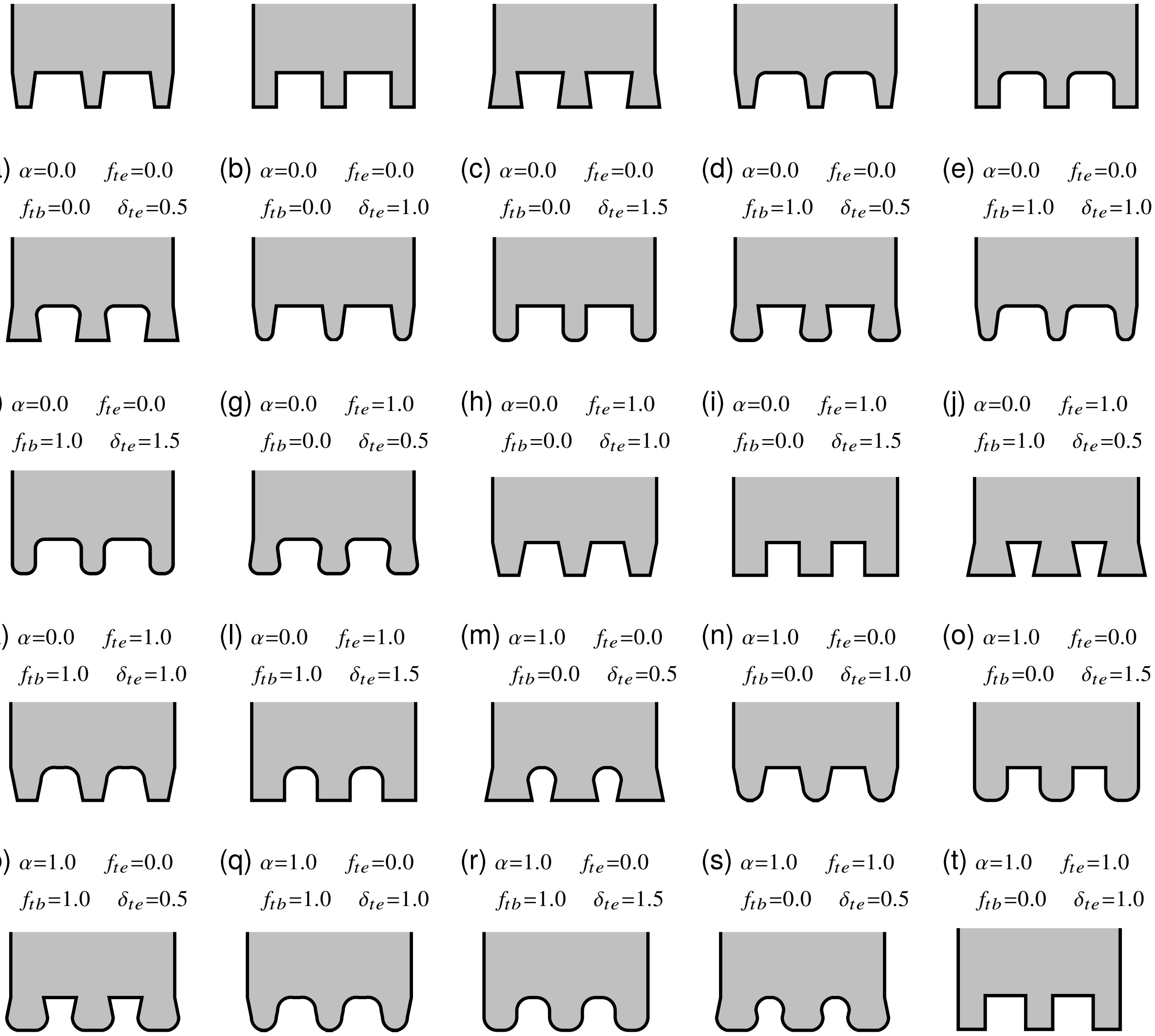

(a) α=0.0 f_{te}=0.0 f_{tb}=0.0 δ_{te}=0.5

(b) α=0.0 f_{te}=0.0 f_{tb}=0.0 δ_{te}=1.0

(c) α=0.0 f_{te}=0.0 f_{tb}=0.0 δ_{te}=1.5

(d) α=0.0 f_{te}=0.0 f_{tb}=1.0 δ_{te}=0.5

(e) α=0.0 f_{te}=0.0 f_{tb}=1.0 δ_{te}=1.0

(f) α=0.0 f_{te}=0.0 f_{tb}=1.0 δ_{te}=1.5

(g) α=0.0 f_{te}=1.0 f_{tb}=0.0 δ_{te}=0.5

(h) α=0.0 f_{te}=1.0 f_{tb}=0.0 δ_{te}=1.0

(i) α=0.0 f_{te}=1.0 f_{tb}=0.0 δ_{te}=1.5

(j) α=0.0 f_{te}=1.0 f_{tb}=1.0 δ_{te}=0.5

(k) α=0.0 f_{te}=1.0 f_{tb}=1.0 δ_{te}=1.0

(l) α=0.0 f_{te}=1.0 f_{tb}=1.0 δ_{te}=1.5

(m) α=1.0 f_{te}=0.0 f_{tb}=0.0 δ_{te}=0.5

(n) α=1.0 f_{te}=0.0 f_{tb}=0.0 δ_{te}=1.0

(o) α=1.0 f_{te}=0.0 f_{tb}=0.0 δ_{te}=1.5

(p) α=1.0 f_{te}=0.0 f_{tb}=1.0 δ_{te}=0.5

(q) α=1.0 f_{te}=0.0 f_{tb}=1.0 δ_{te}=1.0

(r) α=1.0 f_{te}=0.0 f_{tb}=1.0 δ_{te}=1.5

(s) α=1.0 f_{te}=1.0 f_{tb}=0.0 δ_{te}=0.5

(t) α=1.0 f_{te}=1.0 f_{tb}=0.0 δ_{te}=1.0

(u) α=1.0 f_{te}=1.0 f_{tb}=0.0 δ_{te}=1.5

(v) α=1.0 f_{te}=1.0 f_{tb}=1.0 δ_{te}=0.5

(w) α=1.0 f_{te}=1.0 f_{tb}=1.0 δ_{te}=1.0

(x) α=1.0 f_{te}=1.0 f_{tb}=1.0 δ_{te}=1.5

(y) α=0.4 f_{te}=0.0 f_{tb}=0.0 δ_{te}=0.0

Figure 2.4 Tooth configurations with varying tooth shape factor (α), tooth edge fillet (f_{te}), tooth base fillet (f_{tb}), and tooth edge offet (δ_{te})

convergence of force and flux linkage outputs was attained. In the air gap regions where the field changes rapidly, smaller mesh elements were used to improve solution accuracy; mesh control regions were used to restrict the maximum element sizes in the air gap regions of each design. The field was, therefore, correctly captured in the air gap regions.

The finite element analysis (FEA) outputs include the calculated force on the translator. Since the translator is a solid body, this force is calculated by integrating the Maxwell stress tensor over the surface of its model.

There was no significant relative performance cost between using higher-order FEA methods compared to lower-order ones. Also, the force, flux linkage, and co-energy results were not affected by the choice of which phase was excited. As such, all simulations used third-order polynomial elements and phase 1 excitation. The solver was configured to use h-adaptive meshing with small tolerance targets to minimize the effects of meshing errors.

Several actions were taken to minimize the cost of each simulation while maintaining accuracy.

1. Only one side of the double-sided motor was modeled to take advantage of symmetry in reducing the computational cost.

2. Adaptive mesh refinement and sensitivity analysis were used to establish the initial mesh configuration for each motor geometry.

3. Use of third-order polynomial elements, which converged faster than first-order elements and at about the same speed as second-order elements.

4. H-adaptive meshing with a reasonably small tolerance to minimize the effects of meshing errors.

The output of finite element analysis (FEA) for each motor position and winding excitation include the following.

- Instantaneous force $f(N)$ calculated as an integral of the Maxwell stress tensor over the body of the translator.
- Phase flux linkages $\lambda_j(Wb)$ $j \in \{1, 2, 3\}$.
- Copper losses (W).
- Stored magnetic energy (J).
- Stored magnetic co-energy (J).
- Field plots.

2.4.1 Data Management

Figure 2.5 shows the hierarchical view of the data management framework in Archimate 3.0 notation. Archimate 3.0 [58] is an open standard by the Open Group, and it enables broad access to the information presented here. The framework uses four process interfaces to control all data management tasks from configuration to archiving.

At the top level is the Business Layer, which shows the Research Data Pipeline. It starts with Research Workflow Information and output Research Results. Research Workflow Information contains a comprehensive description of all data sources, external application interfaces, and data processing tasks undertaken in the research. The Workflow Configuration interface generates it in the Generate Workflow Specification task. It is implemented at the application layer through

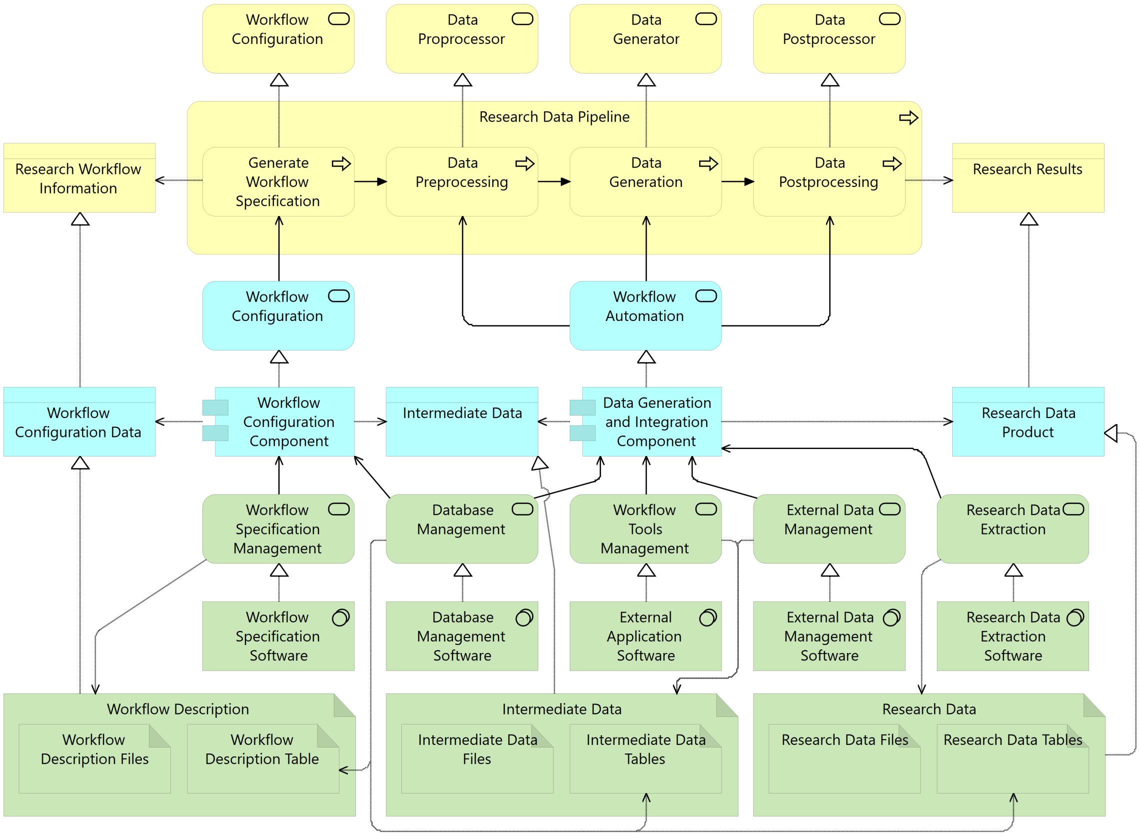

Figure 2.5 Data Management System Architecture

another Workflow Configuration interface. Based on the workflow specification, intermediate data are acquired, generated, and analyzed by the Data Preprocessor, Data Generator, and Data Postprocessor interfaces, respectively. The Workflow Automation application interface is responsible for implementing the data preprocessor, data generator, and data postprocessor.

The Application Layer has two applications, namely, Workflow Configuration Application and Data Generation and Integration Application. The former converts Workflow Description Data to project-specific Intermediate Data, and the latter uses the Intermediate Data to produce the needed Research Data Report. Intermediate Data includes input data manually, field/offline generated data, and application-specific files needed to be converted to match the project's data archiving requirements.

At the Technology Layer, the Workflow Specification Management and the Database Management interfaces implement the Workflow Configuration Application and the External Application Interface, External Data Manager, and Research Data Extractor interfaces respectively implement the Data Generation and Integration Application.

2.4.1.1 Application Layer Implementation

All cases were specified in Extensible Markup Language (XML) format, and ActiveX® automation scripts were used to translate all cases from XML configuration files into 2D magnetostatic models in the software. Automation also included the simulation task and extraction of the results into a relational database where all initial analyses were performed. It makes sense to organize the numerical results of FEA in an adequately accessible way. A relational database was used to store and analyze the numerical results. Even though considerations were given to NoSQL DB management systems, the particular schema of the dataset made it more preferable to use a relational database management system. Therefore, Microsoft SQL Server® was selected.

A Microsoft Powershell® scripting library was developed and used to create an extensible markup language (XML) case file for each of the simulation cases. The details of the data management architecture are presented in [59] and also in figure 2.6. The tasks performed using the Microsoft Powershell® scripting library are summarized as follows.

1. Generation of each simulation case XML file.

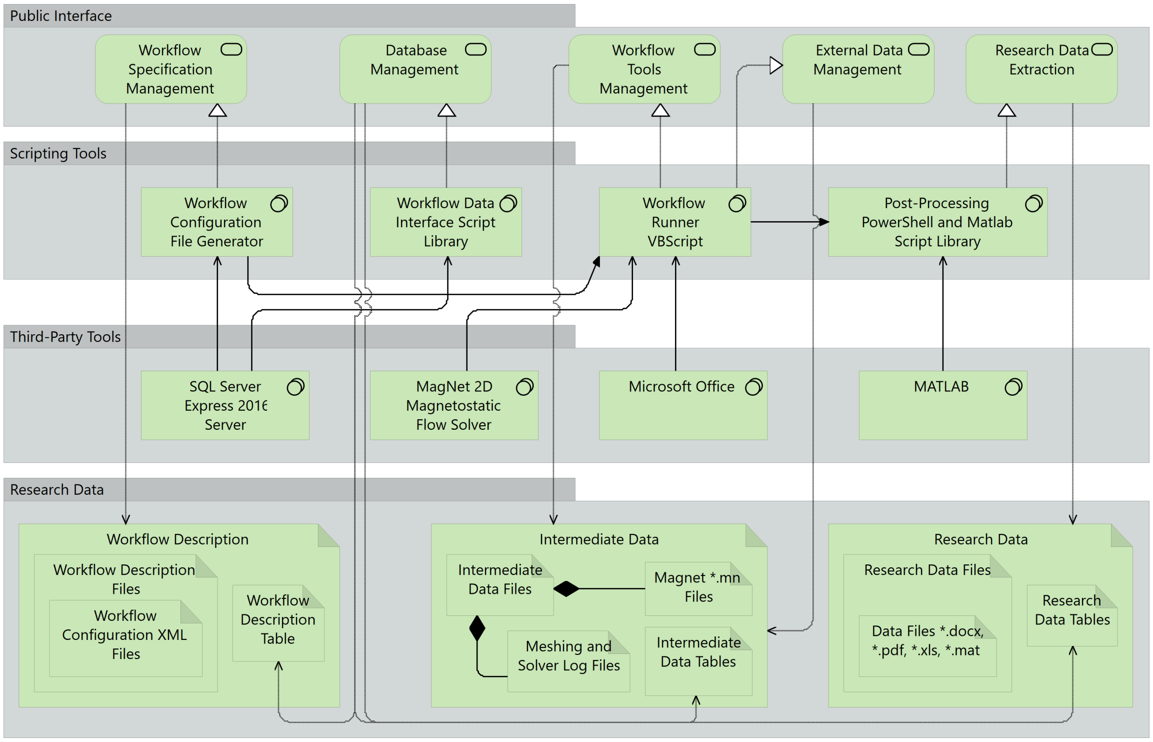

Figure 2.6 Technology Layer Implementation

2. Driving the MagNet® 2D magnetostatic flow solver based on the specifics of each case XML file.

3. Extraction of simulation results.

4. Organization of simulation results into a Microsoft SQL Server® relational database.

CHAPTER 3

CHARACTERIZATION

3.1 Introduction

The net output force of linear variable reluctance (LVR) motors results from variations in the magnetic reluctance of the air gap between opposing teeth of the stator and translator. Tooth geometry affects the shape of the air gap, which in turn influences the variation in reluctance and motor characteristics. As a result, there has been a research focus on understanding the effect of tooth geometry on LVR motor characteristics [12, 40, 60–64]. The presence of core magnetization saturation and nonlinearities [21, 31, 65, 66] presents additional modeling complexities. They have resulted in the lack of an analytical model that adequately represent the characteristics of LVR motors for a wide variety of air gap geometry characteristics. This limitation has constrained the range of air gap geometries studied in the existing literature to rectangular shapes. Finite element analysis (FEA) is the primary tool used to characterize the motors in this study, to expand the range of geometries without losing the model's accuracy.

This chapter has three main focal points. First, it presents a methodology for performing FEA based characterization of various air gap geometries of the coupled and uncoupled LVR motors and discusses the effect of magnetic coupling on the computational requirements for characterization. Secondly, this chapter shows the effects of those parameters on the characteristics of the motor by analyzing the characteristics of LVR motors with various air gap geometric parameters. Finally, as a means to extend the application of the data generated in the former, this chapter presents the development and testing of a nonlinear model for LVR motors. The next chapter uses the nonlinear model to determine an optimal geometry and commutation of LVR motors when subjected to various operating constraints. The author has published portions of this chapter's material in [12, 59, 64].

3.2 Motor Characteristics

This section presents the finite-element based characteristics of both coupled and uncoupled LVR motors under a typical air gap geometry configuration. The air gap geometry of the motors used in characterization have the following parameters (see figure 3.1).

- tooth shape factor, $\alpha = 0.4$
- tooth edge fillet, $f_{te} = 0.0$
- tooth base fillet, $f_{tb} = 0.0$
- tooth edge offset, $\delta_{te} = 0.0$

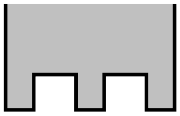

Figure 3.1 Tooth geometry for initial characterisation

The characterization subjects a given LVR motor to a representative sample of possible phase excitations under typical operating conditions. For both motor configurations, the magnitudes of selected excitation currents cover both the linear and nonlinear regions of operation. The number of turns per phase was determined based on the available area around the poles, which changes with tooth shape factor (α).

Simulations for each motor design generated for permutations on excitation currents and translator positions produced the characterization of the motor designs.

3.2.1 Translator Position

Discrete translator positions on a grid of 101 positions of relative displacement between stator and translator teeth from full alignment through complete misalignment and back to full alignment provided the full profile of instantaneous characteristics of the motor over one tooth pitch movement. Each motor position (x), is expressed in terms of p_t and the normalized motor position (x_n) as shown in (3.1) and (3.2).

$$x = x_n p_t \tag{3.1}$$

$$x_n = 0.01r \tag{3.2}$$

Where $r \in \{0, 1, ..., 100\}$.

3.2.2 Phase Excitation

3.2.2.1 Uncoupled LVR motor

Single-phase excitations currents are sufficient to fully characterize the uncoupled motor due to the negligible mutual inductances between its phases. Also, there is no need to consider both negative and positive phase excitation since the lack of mutual inductances means there are no subtractive components in the force output generation.

The FEA runs for the uncoupled motor specified phase current excitations for phase 1 (i_1) energized at various levels for each motor design and position. This grid of excitation current values is denser in the saturation range to improve interpolation accuracy.

$$I_1 \in \{0, 0.01, 0.1, 1, 3, 5, 10, 12, 14, 14.99, 15\} A \tag{3.3}$$

3.2.2.2 Coupled LVR motor

The coupled motor has three-phase coils whose flux paths are magnetically coupled. Magnetic coupling of flux paths among the phases and a corresponding increase in independent variables result in higher modeling complexity and higher requirements on the amount of data needed for characterization as compared to rotary variable reluctance (VR) motors and uncoupled linear variable reluctance (LVR) motors. As a result, nonlinear modeling of the motor must consider simultaneous excitation in all three-phase coils, since high magnetic coupling results in comparable magnitudes for both mutual and self-inductances of the phase windings.

Characterization applied discrete current values on a grid of 11 values for each phase $(1, 2, 3)$. The vectors of excitation currents for phase 1, 2, and 3 windings of the motor are as follows.

$$i_1, i_2, i_3 \in I \cup \{0\} \cup -IA \tag{3.4}$$

$$\text{Where } I = \{3, 5, 10, 12, 15\}A.$$

As a result of these and the 101 translator positions, a maximum of $12,221$ simulations needed to be performed. Taking advantage of the following facts reduced this number to about $2,036$.

1. Switching excitation current values between any two phases results in the same magnitude of force with a reversed sign from the normalized motor position that is symmetrical about $x_n = 0.5$ (3.5); and the phase flux linkages match the phase excitation currents (3.6).

2. Reversing the signs of all phase excitation currents result in the same magnitude and sign of force while changing the sign of all phase flux linkages (3.7).

$$f(i_j, i_k, i_m, x_n) = -f(i_j, i_m, i_k, 1 - x_n) \tag{3.5}$$

$$\lambda_j(i_j, i_k, i_m, x_n) = \lambda_j(i_j, i_m, i_k, 1 - x_n) \tag{3.6}$$

$$f(i_j, i_k, i_m, x_n) = f(-i_j, -i_k, -i_m, x_n) \tag{3.7}$$

$$\lambda_j(i_j, i_k, i_m, x_n) = \lambda_j(-i_j, -i_k, -i_m, 1 - x_n) \tag{3.8}$$

$$\text{Where } j, k, m \in \{1, 2, 3\}.$$

3.2.3 Instantaneous Force Production Profile

This section discusses motor force profiles over a fundamental force period (a tooth pitch) as functions of phase excitation (i_1, i_2, i_3 for coupled and i_1 for uncoupled) and normalized motor position (x_n).

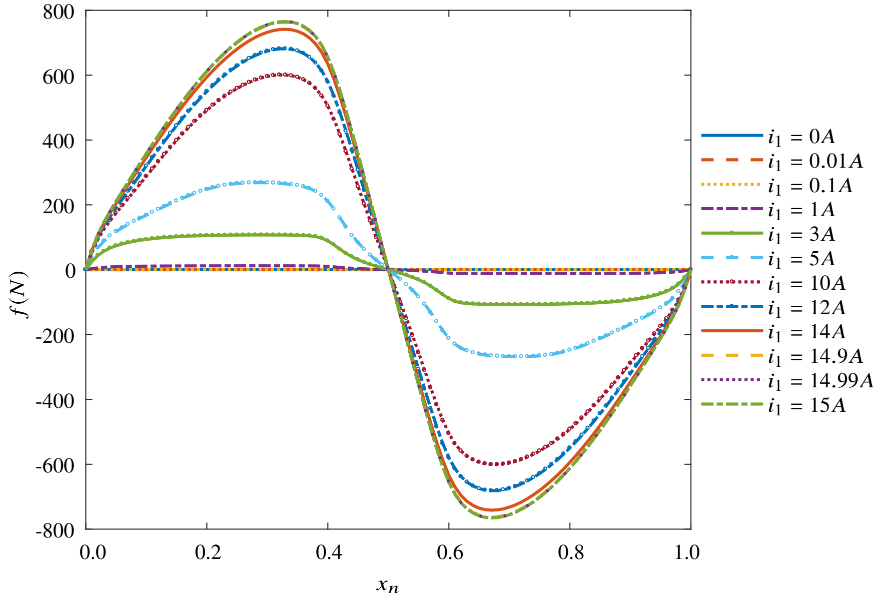

Figure 3.2 Plots of instantaneous force (f) vs. linear motor position (x_n) over one tooth pitch (p_t) for various phase 1 excitation current (i_1) values of the uncoupled linear variable reluctance motor with tooth shape factor ($\alpha = 0.4$), tooth edge fillet ($f_{te} = 0.0$), tooth base fillet ($f_{tb} = 0.0$), tooth edge scaling factor ($\delta_{te} = 0.0$) and pole fillet ($f_p = 0.0$).

3.2.3.1 Uncoupled LVR motor

Two representations of instantaneous force production of the motor for the specified phase 1 excitation currents fixed for motor positions over one tooth pitch are presented in figure 3.2 and 3.3. As seen in figure 3.2, there is no force production for $x_n \in \{0.0, 1.0\}$ where the teeth are fully aligned. The lack of force production in those motor positions is because, in the fully aligned position, the flux lines in the teeth are entirely orthogonal to the direction of motor movement, and there is no tangential force component to drive the motor. On the other hand, the entirely unaligned position ($x_n = 0.5$) also produces no force production, but for a different reason. At $x_n = 0.5$, negative and positive tangential force components are equal, leaving a net zero force production.

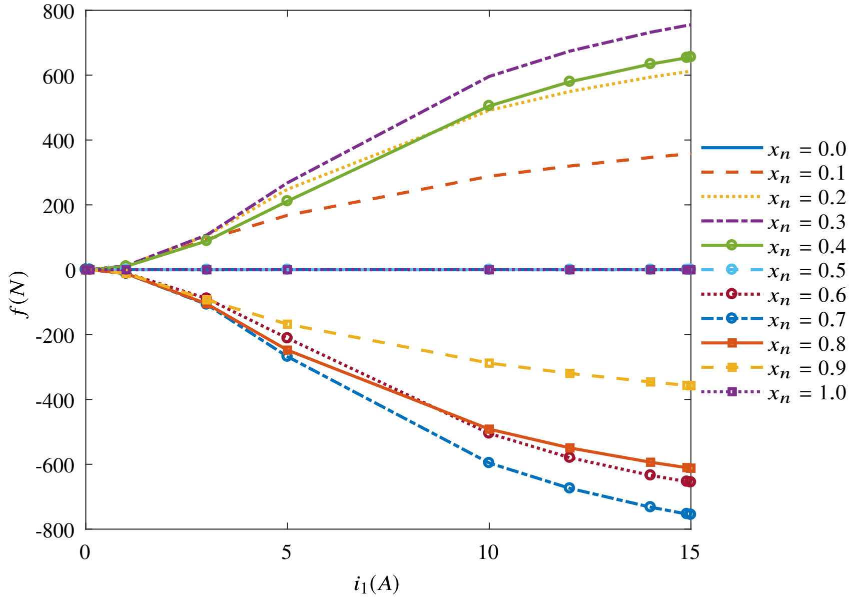

Figure 3.3 Instantaneous force (f) vs. phase 1 excitation current (i_1) plots for various normalized motor positions (x_n) over one tooth pitch (p_t) of the uncoupled linear variable reluctance motor with tooth shape factor ($\alpha = 0.4$), tooth edge fillet ($f_{te} = 0.0$), tooth base fillet ($f_{tb} = 0.0$), tooth edge scaling factor ($\delta_{te} = 0.0$) and pole fillet ($f_p = 0.0$).

Figure 3.2 also shows a wide variation in force production across a tooth pitch even with constant excitation current. This variation is a manifestation of the force ripple for which variable reluctance motors are known. In the existing literature, the reduction of force ripple is a general objective. However, [10] studies applications where it might be beneficial to relax ripple constraints.

3.2.3.2 Coupled LVR motor

Figure 3.4 is arranged in a 5-by-5 grid of sub-plots (for a total of 25 sub-plots). Each of the 25 sub-plots contains 11 waveforms of instantaneous force (f) versus normalized motor position (x_n). Each of the 11 waveforms is produced with a distinct phase current (i_1) and equal

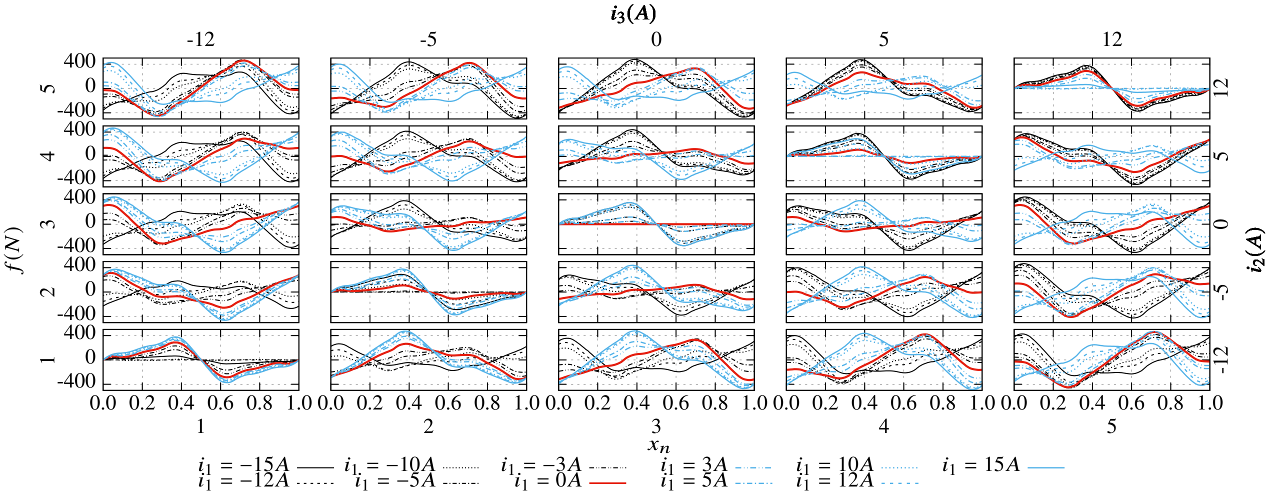

Figure 3.4 Multi-plot grid of instantaneous force output (f) vs. normalized motor position (x_n) plots for various phase 1 excitation (i_1) currents of the coupled LVR motor with tooth shape factor ($\alpha = 0.4$); phase 2 excitation current (i_2) varies vertically and is fixed for each row in $\{1, 2, 3, 4, 5\}$ and phase 3 excitation current (i_3) varies horizontally and is for each column in $\{1, 2, 3, 4, 5\}$.

phase currents (i_2) and (i_3). In other words, phase currents i_2 and i_3 are held constant within each sub-plot.

Across sub-plots, i_2 varies along the numbered rows of plots $\{1, 2, 3, 4, 5\}$ from a minimum of $-12A$ to a maximum of $12A$ in the set $\{-12, -5, 0, 5, 12\}A$. Similarly, i_3 varies along the numbered columns of plots $\{1, 2, 3, 4, 5\}$.

For clarity, the figures do not show all currents in (3.4). This discussion would henceforward refer to each plot according to its row and column number. For example, $plot_{2,4}$ refers to the plot with $i_2 = -5A$ and $i_3 = 5A$. Each curve in the series for $plot_{2,4}$ would be $f = f(i_1, -5, 5, x_n)$.

There is a wide variation of force output for each series plot even though excitation current is held constant along each curve. This observation is characteristic of the force ripple behavior of the coupled LVR motor, a well known and often undesirable feature in many applications.

The instantaneous force plot of the coupled LVR motor has an odd symmetry about the position of total phase 1 misalignment ($x_n = 0.5$) for the cases where $i_2 = i_3$ $plot_{s,s}; s \in \{1, 2, ..., 5\}$). However, since this symmetry is not valid for all other plots, is it not possible to intuitively select the turn-on and turn-off positions for each phase. Therefore, this work does not impose any such assumptions; the results show operation modes in which one phase, two phases, or all three phases, are simultaneously excited.

The facts listed in Section 3.2.2.2 can be seen by examining figure 3.4; hence, (3.9) is valid for any plot on row, s, and column, t. For instance, each curve in $plot_{3,1}$ of figure 3.4 is the same as that of the corresponding one from the same i_1 excitation in $plot_{1,3}$ rotated 180^o about $x_n = 0.5$.

$$f(i_1, x_n)|_{plot_{s,t}} = -f(i_1, 1 - x_n)|_{plot_{t,s}} \tag{3.9}$$

$$f(i_1, x_n)|_{plot_{s,t}} = f(-i_1, x_n)|_{plot_{6-t,6-s}} \tag{3.10}$$

Where $s, t \in \{1, 2, 3, 4, 5\}$.

Figure 3.4 confirms (3.7) since, from observation, (3.10) holds for any plot on row s and column t. Hence, each i_1 curve in $plot_{3,1}$ of figure 3.4 is the same as that of the corresponding $-i_1$ curve in $plot_{5,3}$ rotated 180^o about $x_n = 0.5$.

3.2.4 Instantaneous Flux Linkage

3.2.4.1 Uncoupled LVR motor

Two representations of the flux linkage over one tooth pitch are shown in figures 3.5 and 3.6, for the motor design with tooth shape factor $\alpha = 0.4$ and $f_{te}, f_{tb}, \delta_{te}, f_p = 0.0$.

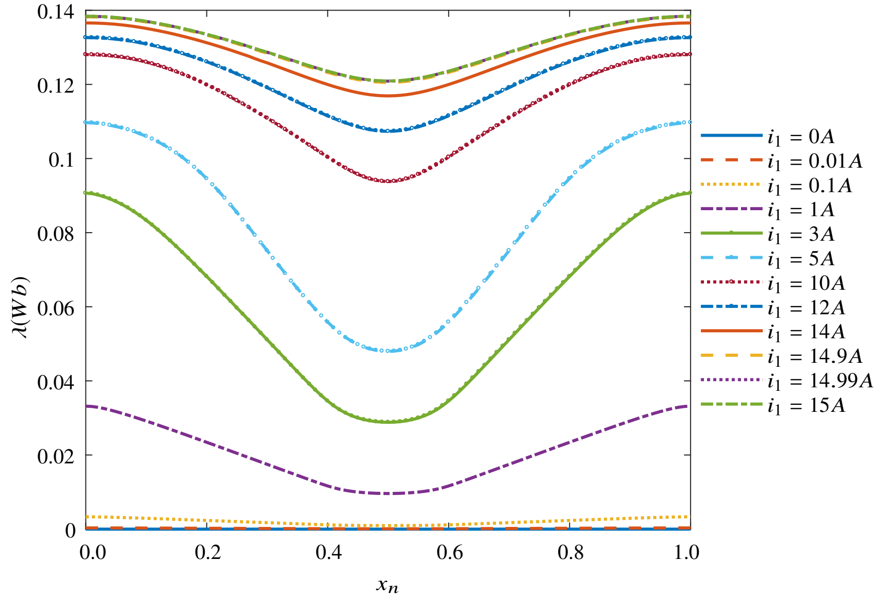

Figure 3.5 Comparison of instantaneous flux linkage (λ) vs. normalized motor position (x_n) over one tooth pitch (p_t) plots for various phase 1 excitation current (i_1) values of the uncoupled linear variable reluctance motor with tooth shape factor ($\alpha = 0.4$), tooth edge fillet ($f_{te} = 0.0$), tooth base fillet ($f_{tb} = 0.0$), tooth edge scaling factor ($\delta_{te} = 0.0$) and pole fillet ($f_p = 0.0$).

In figures 3.3 and 3.6, the effects of saturation are apparent for all positions since the gradient of the force curve is steep and linear for lower phase excitation currents. Yet, higher phase excitation currents show minimal gains in force and flux for proportional increases in excitation currents. It is also notable that the magnetic saturation occurs at the highest phase excitation currents for the entirely unaligned position (linear motor position, $x_n = 0.5$). Here, nonlinearities begin to show with phase 1 excitation, $i_1 \approx 10A$. On the other hand, the effects of magnetic saturation start showing with phase 1 excitation, $i_1 \approx 3A$, when the motor is in full alignment. The saturation effects range between the two extremes for intermediate linear motor positions.

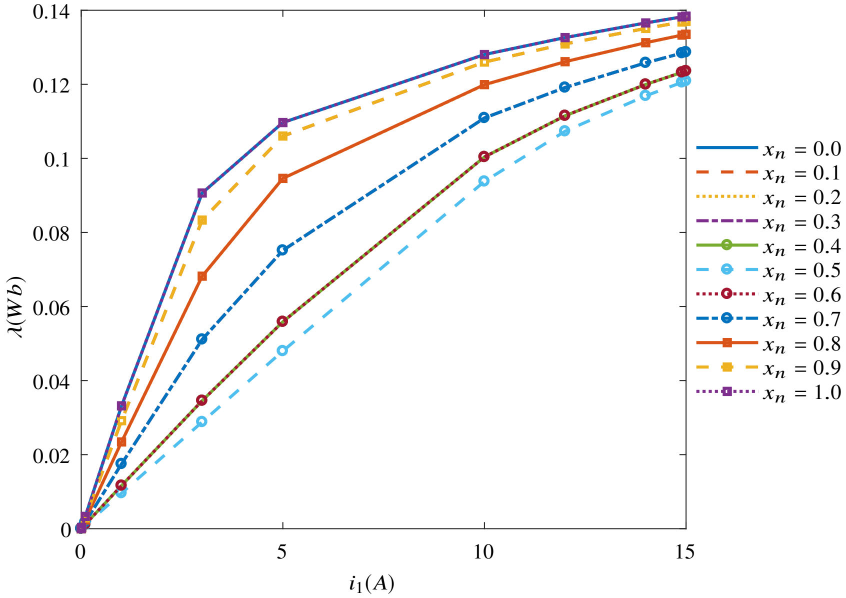

Figure 3.6 Comparison of instantaneous flux linkage (λ) vs. phase 1 excitation current (i_1) plots for various linear motor positions (x_n) over one tooth pitch (p_t) of the uncoupled linear variable reluctance motor with tooth shape factor ($\alpha = 0.4$), tooth edge fillet ($f_{te} = 0.0$), tooth base fillet ($f_{tb} = 0.0$), tooth edge scaling factor ($\delta_{te} = 0.0$) and pole fillet ($f_p = 0.0$).

In figure 3.5, the instantaneous flux linkage for varying motor positions and currents shows significant harmonics that are difficult to account for in analytical models. Comparing figures 3.2 and 3.5, the highest force occurs at positions where the gradients of the flux linkage curves are steepest. This coincidence in flux and force requirements possess a possible trade-off relationship between the maximum force production and the maximum speed of operation; since a steeper flux linkage gradient limits the stall speed of the motor when operating at a constant excitation voltage. Also, figure 3.3 and 3.6 show that these positions experience significant magnetic saturation that further complicates the possibility of defining relevant analytical models for the full range of the motor's operation.

3.2.4.2 Coupled LVR motor

The discussion uses only flux linkage on phase 1 (λ_1); the periodicity requirement of the motor's construction and operation leads to similar observations in λ_2 and λ_3.

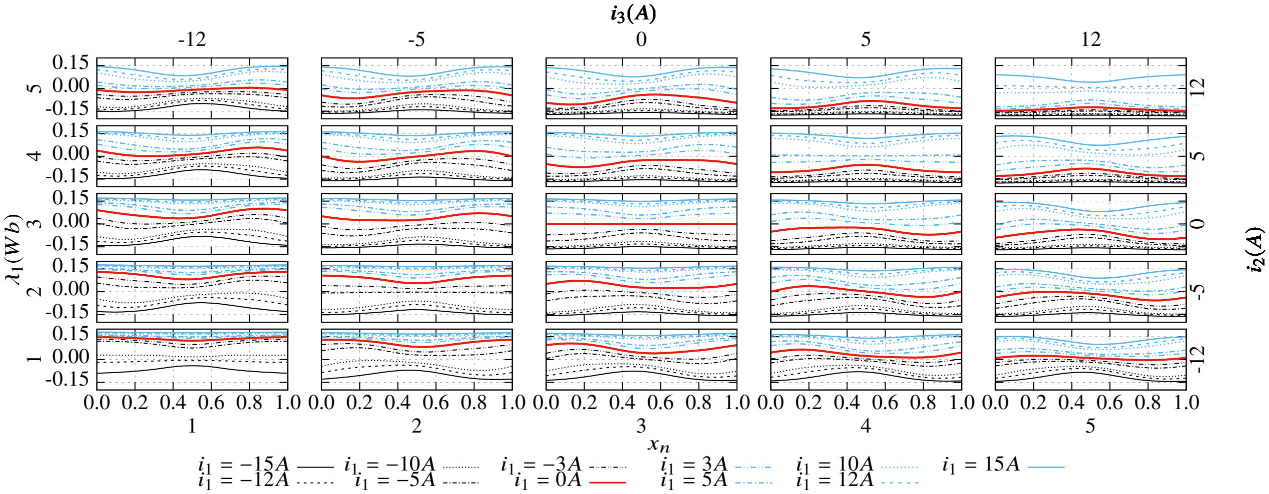

Figure 3.7 Multi-plot grid of instantaneous phase 1 flux linkage (λ_1) vs. normalized motor position (x_n) plots for various phase 1 excitation (i_1) currents of the coupled LVR motor with tooth shape factor ($\alpha = 0.4$); phase 2 excitation current (i_2) varies vertically and is fixed for each row in $\{1, 2, 3, 4, 5\}$ and phase 3 excitation current (i_3) varies horizontally and is for each column in $\{1, 2, 3, 4, 5\}$.

Figure 3.7 shows a 5-by-5 multi-plot grid structured similar to figure 3.4, but with a different dependent variable (λ_1). For each plot in the grid of figure 3.4, phase currents (i_1, i_2, i_3) are held constant and the instantaneous phase 1 flux linkage (λ_1) is plotted against normalized motor position (x_n). See section 3.2.3.2 for a detailed discussion of the multi-plot structure.

Like the instantaneous force profile, figure 3.7 shows the even symmetry of the λ_1 plots about $x_n = 0.5$ is valid only for cases where $i_j = i_k; j, k \in \{1, 2, 3\}$. This fact adds complexity to the motor's dynamic operation and control.

Equation (3.5) is clearly demonstrated in figure 3.7. Hence, (3.11) is valid for, $plot_{s,t}$. For example, each curve in $plot_{3,1}$ of figure 3.7 is the same as that of the corresponding one from the same i_1 excitation in $plot_{1,3}$ reflected about $x_n = 0.5$.

$$\lambda_1(i_1, x_n)|_{plot_{s,t}} = \lambda_1(i_1, 1 - x_n)|_{plot_{t,s}} \tag{3.11}$$

$$\lambda_1(i_1, x_n)|_{plot_{s,t}} = -\lambda_1(-i_1, 1 - x_n)|_{plot_{6-t,-s}} \tag{3.12}$$

Where $s, t \in \{1, 2, 3, 4, 5\}$

Equation (3.8) is confirmed in figure 3.7 since, from observation, (3.12) holds for any $plot_{s,t}$. Each i_1 curve in $plot_{5,2}$ of figure 3.7 is the same as that of $-i_1$ excitation in plot $plot_{4,1}$ rotated 180^o about $x_n = 0.5$.

3.2.4.2.1 Saturation

Saturation is affected by the magnitude of excitation currents and normalized motor position. Figure 3.7 shows the effects of saturation on λ_1 for all phase excitations and x_n. λ_1 is zero for all x_n when $i_1 = i_2 = i_3$ and it increases in magnitude as the deviation the phase excitation currents increases. However, due to saturation, the marginal increase in λ_1 decreases as the deviation between phase excitation currents increases. This effect is clearly observable by comparing plots $plot_{1,1}$, $plot_{1,5}$, $plot_{5,5}$, and $plot_{5,1}$ in figure 3.7. The role of x_n on λ_1 saturation is demonstrated in all plots of figure 3.7. Generally, the range of λ_1 is least at the position of full phase 1 misalignment ($x_n = 0.5$) and increases to a maximum at the position of full alignment ($x_n \in \{0.0, 1.0\}$). Saturation effects are least at $x_n = 0.5$, highest at $x_n \in \{0.0, 1.0\}$ and it ranges between the extremes for intermediate positions; with a few exceptions.

Figure 3.4 shows that f varies widely for any fixed current applied over a full pitch. The fact that instantaneous force (f) for variable reluctance motors is a function of a spatial derivative of λ_1 explains this variation. The motor is, therefore, typically operated with non-sinusoidal commutation with high harmonic content, whether or not there are ripple constraints [10].

Hence, the motor typically operates with high harmonics and saturation that analytical expressions cannot easily model.

3.3 Effect of Tooth Geometry on Motor Characteristics

This section presents the relative effect of four geometric parameters that affect the air gap reluctance on the characteristics of the LVR motor. With tooth pitch held constant, the geometric parameters of interest are tooth width, tooth edge fillet, tooth base fillet, and tooth angle (whether tapered or dovetailed). Previous work on air gap geometry for this kind of motor has been focused only on a limited number of tooth widths. By considering four more geometric characteristics, this study explores a broader set of features. It allows the possibility of finding an optimal air gap geometry outside those already discussed in published literature.

For each motor geometry, 2D magnetostatic finite element analysis generates the magnetic characteristics, particularly flux linkage and force. Post-processing of the data stores the characteristics as functions of motor displacement and current for the family of motors. Analysis of the data reveals the influence of tooth geometry on motor characteristics such as which geometry provides the maximum average force per mass (necessary for fast motion applications). Force production capability does not vary monotonically with tooth width or tooth fillet; instead, a particular tooth width and tooth fillet correspond to maximum average force (averaged over a tooth pitch). This observation provides valuable insight into the optimal geometrical design.

3.3.1 Analytical Model

The effect of tooth geometry on motor characteristics has been presented in [13] but without considering saturation effects and harmonics. [13] uses equivalent magnetic circuits to derive the phase flux linkage and the phase inductance as functions of air gap geometry (tooth geometry). For each phase, indexed j, the truncated Fourier series expansion of the periodic inductances, L_{jj}, for p_t is given by (3.13). The phase flux linkage, λ_j, is given by (3.14). Note that for the uncoupled LVR motor, mutual inductances are zero.

$$L_{jj} = L_0 + L_1 cos\left(\frac{2\pi}{p_t}x_n - (j-1)\frac{2\pi}{3}\right); j \in \{1,2,3\} \tag{3.13}$$

L_0 is the average self-inductance, and L_1 is the variation of inductance due to air gap differences.

$$\lambda_j = L_{jj} i_j \tag{3.14}$$

Air gap geometry, therefore, determines the instantaneous force output of the motor (f) given by (3.15).

$$f = \frac{1}{2}\sum_{j=1}^{3} i_j \frac{dL_{jj}}{dx}; j \in \{1,2,3\} \tag{3.15}$$

(a) $\alpha = 0.0$ (b) $\alpha = 0.1$ (c) $\alpha = 0.2$ (d) $\alpha = 0.3$

(e) $\alpha = 0.4$ (f) $\alpha = 0.5$ (g) $\alpha = 0.6$ (h) $\alpha = 0.7$

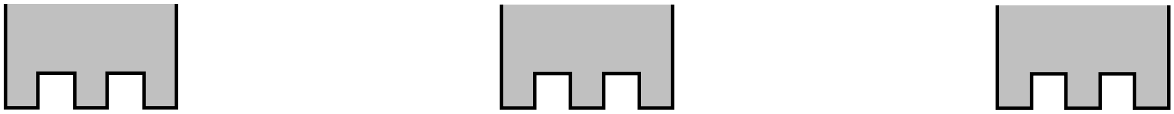

(i) $\alpha = 0.8$ (j) $\alpha = 0.9$ (k) $\alpha = 1.0$

Figure 3.8 Tooth configurations with varying tooth shape factor (α), tooth edge fillet $f_{te} = 0.0$, tooth base fillet $f_{tb} = 0.0$, and tooth edge offset $\delta_{te} = 0.0$.

3.3.2 Parameter Selection

Figure 3.8 shows the eleven tooth width settings of the LVR motor designs used in this study. Each LVR motor design variation has a particular tooth shape factor (α). Magnetostatic FEA simulations of various configurations of the motor were performed at 101 teeth alignment positions of the translator, defined by motor position (x).

$$x \in 0.01kp_t; k = 0, 1, \ldots, 100 \tag{3.16}$$

The tooth shape factor (α) values in the study are given by:

$$\alpha \in \{0.1q\}; q = 0, 1, ..., 10 \tag{3.17}$$

A finite set of $f_{te} \in \{0.0, 0.5, 1.0\}$ and $f_{tb} \in \{0.0, 0.5, 1.0\}$ was used for the simulations performed in this study. A discrete set of $\delta_{te} \in \{0.5, 1.0, 1.5\}$ was used in the simulations performed in this study. See figures 3.9 to 3.11.

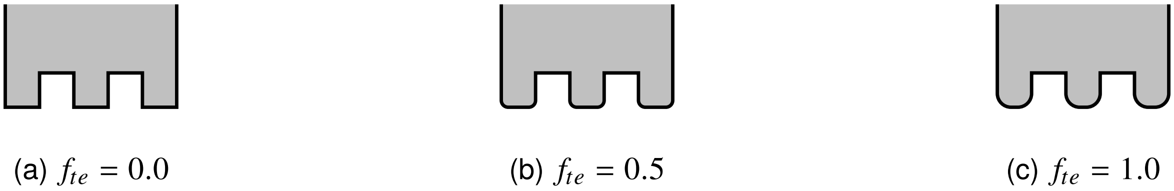
(a) $f_{te} = 0.0$ (b) $f_{te} = 0.5$ (c) $f_{te} = 1.0$

Figure 3.9 Tooth configurations with varying tooth edge fillet (f_{te}), tooth shape factor ($\alpha = 1.0$), tooth base fillet $f_{tb} = 0.0$, and tooth edge offset $\delta_{te} = 0.0$.

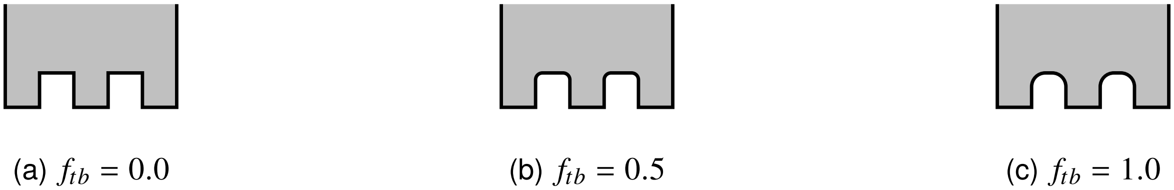
(a) $f_{tb} = 0.0$ (b) $f_{tb} = 0.5$ (c) $f_{tb} = 1.0$

Figure 3.10 Tooth configurations with varying tooth base fillet (f_{tb}), tooth shape factor ($\alpha = 1.0$), tooth edge fillet $f_{te} = 0.0$, and tooth edge offset $\delta_{te} = 0.0$.

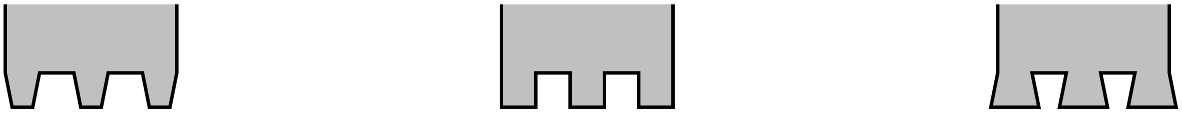

(a) $\delta_{te} = 0.5$ (b) $\delta_{te} = 1.0$ (c) $\delta_{te} = 1.5$

Figure 3.11 Tooth configurations with varying tooth edge offset (δ_{te}), tooth shape factor ($\alpha = 1.0$), tooth edge fillet $f_{te} = 0.0$, and tooth base fillet $\delta_{te} = 0.0$.

3.3.3 Comparison of Force Production for Various Tooth Shape Factors

The interest in the effect of tooth width on air gap geometry is prominent due to its influence on the cross-sectional area of the air gaps and hence their reluctance. This section analyses the effect of varying the tooth shape factor while holding other tooth geometry parameters (f_{te}, f_{tb}, δ_{te}, f_p) at zero.

3.3.3.1 Uncoupled LVR motor

Figure 3.12 depicts the influence of tooth shape on flux linkage and force. The root mean square (RMS) value of the instantaneous force production (F) for positions of the LVR motor over one full tooth pitch (p_t) is calculated as (F_{RMS}) together with the RMS loss over motor over the same set of positions (P_{RMS}). Table 3.1 shows the results of those calculations.

The combination of the copper losses and hysteresis losses derived from FEA are the losses experienced by the motor. Hysteresis losses were estimated (for benchmarking purposes) by assuming that the current varied at a fixed frequency of $60Hz$ for all configurations. This assumption neglects the fact that the actual variation of commutation current would possibly have several harmonics and a fundamental frequency that is different from the assumed one. This

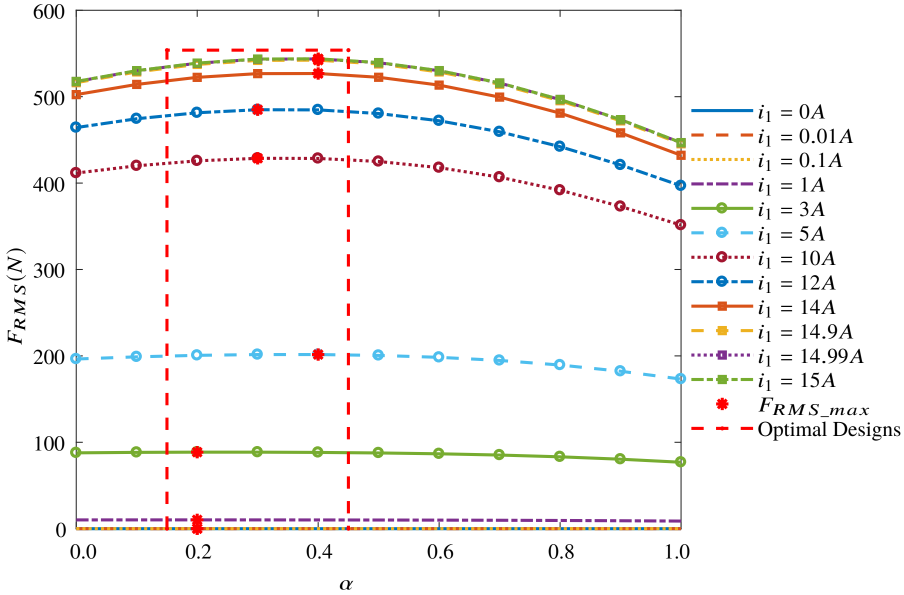

Figure 3.12 Comparison of full pitch positions RMS force production (F_{RMS}) vs. designed motor tooth shape factor (α) plots for various phase 1 excitation current (i_1) values of the uncoupled linear variable reluctance motor. F_{RMS_max} points show the α values for the motor designs that give the maximum F_{RMS} output for each excitation current level. The *Optimal Designs* box indicates the range of α values for the motor designs that provide the maximum F_{RMS} output for all excitation current levels. Other tooth geometry properties namely tooth edge fillet ($f_{te} = 0.0$), tooth base fillet ($f_{tb} = 0.0$), tooth edge scaling factor ($\delta_{te} = 0.0$) and pole fillet ($f_p = 0.0$) are held constant.

approximation is still acceptable in this case since the focus is on learning the effect of varying core geometry on hysteresis losses regardless of operating conditions.

Based on the design parameters specified in Table 2.1, the total volume of upper and lower motor translators is calculated using (3.18).

$$V_T = 515 + 27.5\alpha \tag{3.18}$$

Table 3.1 Comparison of Full Pitch Force Production and Force Densities for Various Designed Motor Tooth Shape Factors (α)

α %	F_{RMS} N	V_T cm^3	P_{RMS} W	FD_{RMS} Ncm^{-3}	FD_{RMS}/P_{RMS} $NW^{-1}cm^{-3}$
0	411.61	475	47.62	0.867	0.0182
10	420.02	478	47.49	0.879	0.0185
20	425.74	481	47.36	0.885	0.0187
30	428.69	484	47.22	0.886	0.0188
40	428.52	487	47.09	0.880	0.0187
50	425.01	490	46.96	0.867	0.0185
60	417.87	493	46.82	0.848	0.0181
70	406.84	496	46.67	0.820	0.0176
80	391.77	499	46.52	0.785	0.0169
90	372.96	502	46.37	0.743	0.0160
100	351.36	505	46.22	0.696	0.0151

Two prominent figures of merit are calculated. The ratio of motor RMS Force (F_{RMS}) to translator volume (V_T) is calculated as RMS Force Density (FD_{RMS}), and the ratio of RMS Force Density to RMS Loss is calculated for all other motor designs under consideration as illustrated in Table 3.1.

Table 3.1 shows that the maximum RMS Force (F_{RMS}), RMS Force Density (FD_{RMS}), and the ratio of RMS Force Density to RMS Loss (FD_{RMS}/P_{RMS}) all occur for the uncoupled LVR motor with tooth shape factor, $\alpha = 0.3$ (highlighted in Table 3.1). The results show that there is minimal to no need to consider the effects of translator volume changes (V_T) and core losses due to V_T changes when considering motor designs that maximize force production, subject to varying tooth shape factor (α). However, as this insight is based on an instantaneous commutation and not based on the whole spectrum of possible phase excitations, it only serves as a guide to further optimization studies, and it does not offer certain prescriptions by itself. Additionally, since this suggestion runs contrary to the conclusion by [63] that force production is largest for motors having the greatest feasible tooth width ($\alpha = 1.0$), further investigation is warranted.

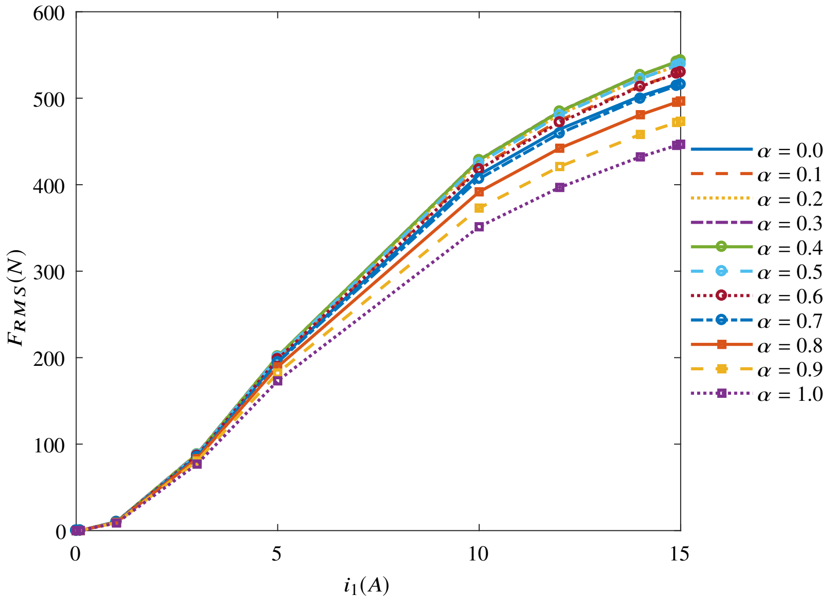

Figure 3.13 Comparison of full pitch RMS force production (F_{RMS}) vs. phase 1 excitation current (i_1) plots for various designed motor tooth shape factors (α). Other tooth geometry properties namely tooth edge fillet ($f_{te} = 0.0$), tooth base fillet ($f_{tb} = 0.0$), tooth edge scaling factor ($\delta_{te} = 0.0$) and pole fillet ($f_p = 0.0$) are held constant.

Combining the information in table 3.1 and figures 3.12 and 3.13 it is apparent that the maximum force production is achieved between $\alpha = 0.2$ and $\alpha = 0.4$ for all phase 1 excitation currents. These results offer an insight into considerations for designs that could be utilized for force maximization studies. Preliminary studies show that these designs have some advantages in constrained-ripple force maximization and loss minimization operations.

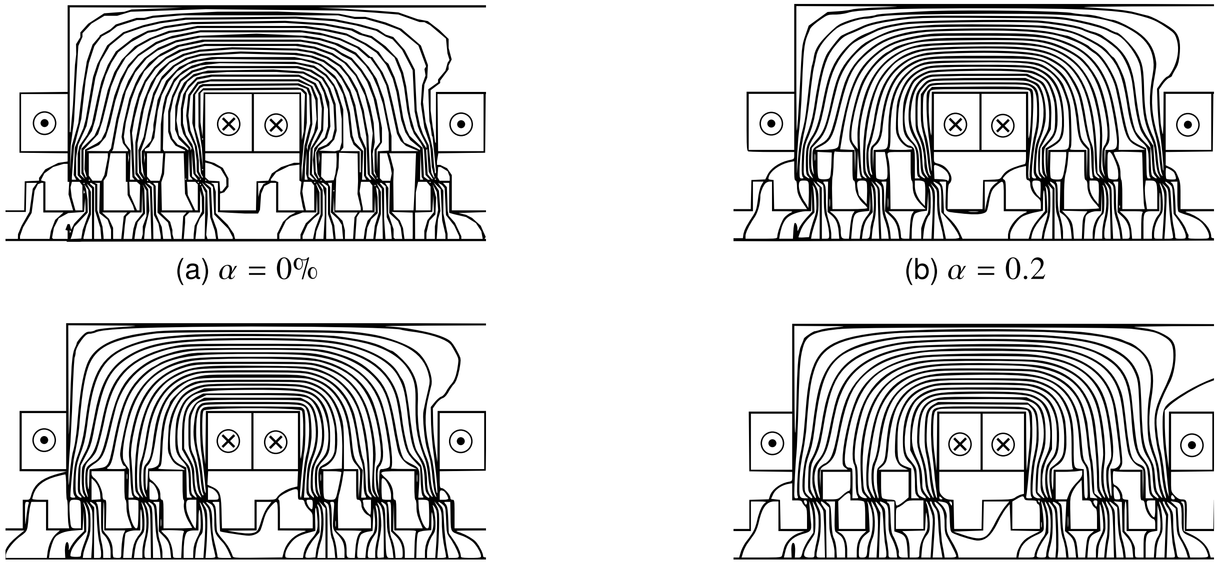
(a) $\alpha = 0\%$
(b) $\alpha = 0.2$
(c) $\alpha = 0.4$
(d) $\alpha = 1.0$

Figure 3.14 Flux lines for FEA runs at linear motor Position ($x_n = 0.25$) and Phase 1 Excitation ($i_1 = 8A$) for Uncoupled LVR Motors with tooth shape factor ($\alpha \in \{0.0, 0.2, 0.4, 1.0\}$). Other tooth geometry properties namely tooth edge fillet ($f_{te} = 0.0$), tooth base fillet ($f_{tb} = 0.0$), tooth edge scaling factor ($\delta_{te} = 0.0$) and pole fillet ($f_p = 0.0$) are held constant.

A possible explanation for the observed variation can be explained using figure 3.14, which shows the flux lines for various motor designs at the same motor position and current. While flux lines typically split between adjacent and opposing teeth for the motor design with $\alpha = 1.0$, the flux lines are concentrated in the opposing teeth for all the other tooth shape factors having $\alpha <= 0.4$. Also, note that there is more fringing in the motor design with $\alpha = 1.0$ than the others in the figure.

In general, the flux lines are more concentrated between opposing teeth for designs with $\alpha <= 0.4$, and sparsity starts to develop in designs with $\alpha = 0.5$ then increase to a maximum in those with $\alpha = 1.0$.

Another critical observation is the fact that the motor design with the highest F_{RMS} also has the highest FD_{RMS} and FD_{RMS}/P_{RMS}. Hence the next section would only focus on using F_{RMS} as a basis for comparing motor geometries to simplify the analysis since the introduction of other geometric factors significantly increases the size of the dataset.

3.3.3.2 Coupled LVR motor

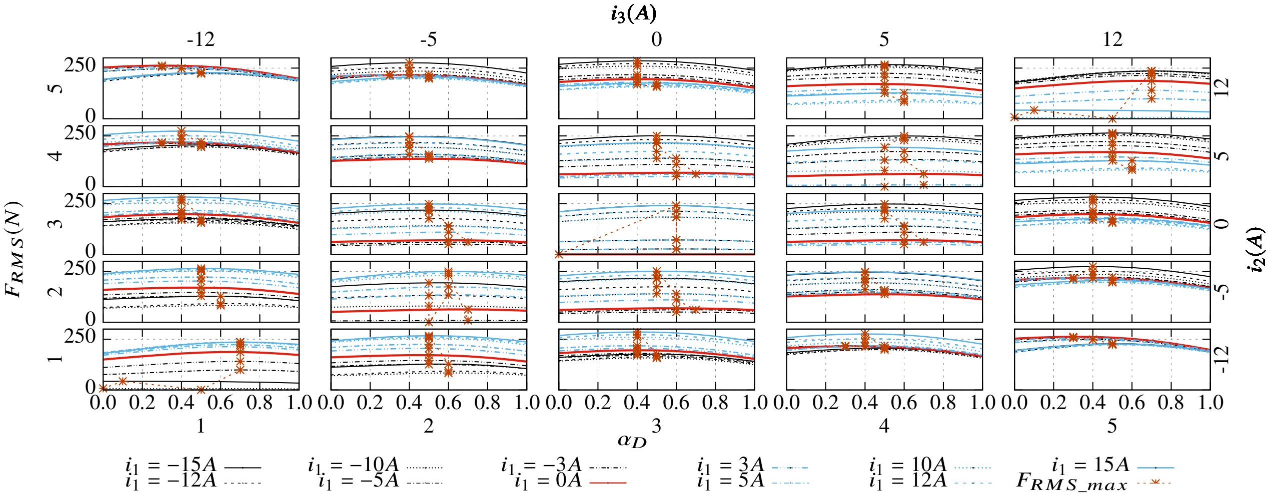

Figure 3.15 Multi-plot grid of plots comparing full pitch positions RMS force production (F_{RMS}) against designed motor tooth shape factor (α) plots for several phase 1 excitation (i_1) currents of the coupled linear variable reluctance motor; phase 2 excitation current (i_2) varies vertically and is fixed for each row in $\{1, 2, 3, 4, 5\}$ and phase 3 excitation current (i_3) varies horizontally and is for each column in $\{1, 2, 3, 4, 5\}$. F_{RMS_max} points show the α values for the motor designs that give the maximum F_{RMS} output for each excitation (i_1, i_2, i_3).

This section uses the characterization of the coupled LVR motor geometries of interest as a basis to comparatively analyze the effect of tooth geometry on the motor's force output. It uses the root mean square force as the figure of interest in making this analysis. This quantity, as seen in (3.19) and (3.20), shows the effect of phase excitation (i_1, i_2, i_3) on the motor's force output over one tooth pitch. As a result, F_{RMS} eliminates the need to compare instantaneous force at individual x_n positions leaving the need to focus only on the different combinations of phase excitations (1, 331 in this case) and which motor geometries yield the highest force output under most phase excitations.

$$F_{RMS}(i_1, i_2, i_3) = \sqrt{\frac{1}{p_t}\int_{x_0}^{x_0+p_t} \Big[f(i_1, i_2, i_3, x)\Big]^2 dx} \tag{3.19}$$

Where x_0 is any arbitrary initial x.

$$F_{RMS}(i_1, i_2, i_3) = \sqrt{\int_{0}^{1} \Big[f(i_1, i_2, i_3, x_n)\Big]^2 dx_n} \tag{3.20}$$

Figure 3.15 is a 5-by-5 grid of plots that show shows F_{RMS} as a function of x_n whilst holding $\{i_1, i_2, i_3\}$ constant in each curve, and $\{i_2, i_3\}$ is constant in each plot ($plot_{s,t}; s, t \in \{1, 2, ..., 5\}$). Figure 3.4 has a similar structure, so this section only gives an abridged description of the structure of figure 3.15; see section 3.2.3.2 for a comprehensive description of the multi-plot structure. i_2 is constant for each row but varies from row to row. i_3 is constant for each column but varies from column to column. Curves for negative i_1 excitation are colored black, positive i_1 current plots are light blue, and zero plots are red.

The defined F_{RMS_max} points in figure 3.15 that give a general indication of which α values provide the maximum force output for any given phase excitation. Figure 3.16 additionally shows the statistical frequency (f_{α_D}) distribution of each α and the number of excitations for which it gives the highest F_{RMS} compared to other x_n geometries when subjected to the same excitation. Clearly $\alpha = 0.5$ gives the highest F_{RMS} for the most excitations but $\alpha = 0.4$ is a close second. Two

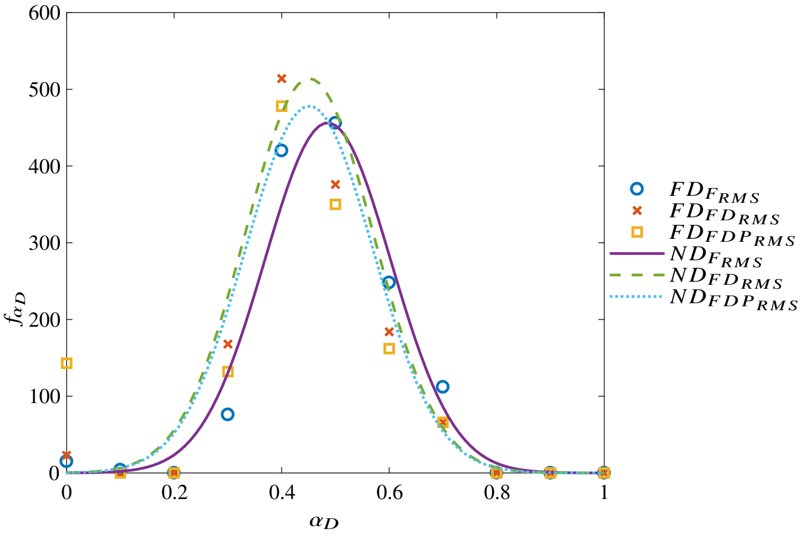

Figure 3.16 Frequency distributions of the number of phase excitations for which each designed tooth geometry (α) of the coupled LVR motor provides the maximum root mean square (RMS) force (F_{RMS}), RMS force density (FD_{RMS}) or RMS force density to RMS copper loss (FDP_{RMS}) compared to other tooth geometries. $FD_{F_{RMS}}$, $FD_{FD_{RMS}}$ and $FD_{FDP_{RMS}}$ are the raw frequency distributions from the finite element analysis (FEA) data when the respective variables are the design objective. $ND_{F_{RMS}}$, $ND_{FD_{RMS}}$ and $ND_{FDP_{RMS}}$ are the frequency distributions when the raw FEA data is fitted to the normal probability density function and the respective variables are the design objective.

additional figures of merit were defined to form the basis for comparing coupled LVR motors of different tooth geometries.

The root mean square (RMS) force density (FD_{RMS}) is defined in a ratio of F_{RMS} to the total volume of the motor's translator core (V_T). V_T is defined in (3.22) based on the motor design parameters specified in table 2.1.

$$FD_{RMS}(i_1, i_2, i_3) = \frac{F_{RMS}(i_1, i_2, i_3)}{V_T} \tag{3.21}$$

$$V_T = 285 + 10\alpha \tag{3.22}$$

Using FD_{RMS} as the figure of merit, the coupled LVR motor with tooth geometry $\alpha = 0.4$ has the highest FD_{RMS} for most excitations. See figure 3.16.

Finally, by defining a third figure of merit (FDP_{RMS}) as the ratio of FD_{RMS} and the root mean square (RMS) copper loss for motor positions over one full pitch (P_{RMS}), the coupled LVR motor with tooth geometry $\alpha = 0.4$ still has the highest FDP_{RMS} for most phase excitations. See figure 3.16. P_{RMS} and FDP_{RMS} are defined in (3.23) and (3.24) respectively.

$$P_{RMS}(i_1, i_2, i_3) = \sum_{j=1}^{3} \left[\int_0^1 i_j^2 r_j dx_n \right] \tag{3.23}$$

$$FDP_{RMS} = \frac{FD_{RMS}}{P_{RMS}} \tag{3.24}$$

Table 3.2 shows the means, and standard deviations of the distribution of highest output coupled LVR motor designs fitted to normal distributions with 95% confidence using F_{RMS}, FD_{RMS} and FDP_{RMS} as figures of merit. It shows that overall, $\alpha \in [0.44, 0.50]$ are the best candidates for all figures of merit. Specifically $\alpha \in [0.48, 0.49]$ are best for F_{RMS}, $\alpha \in [0.44, 0.46]$ are best for FD_{RMS} and $\alpha \in [0.48, 0.50]$ are best for FDP_{RMS}.

Table 3.2 Comparison of Full Pitch Force Production and Force Densities for Various Designed Motor Tooth Shape Factors (α)

Figure of Merit	α			
	μ_α	σ_α	μ_{min_α}	μ_{max_α}
F_{RMS} (N)	0.49	0.12	0.48	0.49
FD_{RMS} (Ncm^{-3})	0.45	0.12	0.44	0.46
FD_{RMS}/P $(NW^{-1}cm^{-3})$	0.41	0.17	0.40	0.42

These findings run contrary to the conclusion by [63] that the force production is largest for motors having the greatest possible tooth width ($\alpha = 100\%$), further investigation is warranted.

3.3.4 The Effect of Fillets and Tapering on Force Production

3.3.4.1 Uncoupled LVR motor

The plots in figure 3.17 depict the effect of pole fillet (f_p), tooth edge fillet (f_{te}), tooth base fillet (f_{tb}) or tooth edge scale factor (δ_{te}) on the rms force production (F_{RMS}) of the uncoupled LVR motor. Each data point is drawn from a subset of motor geometries, is achieved by holding the geometric factor of interest (f_p, f_{te}, f_{tb}, or δ_{te}) constant while allowing all other factors (including tooth shape factor, α) to change. The F_{RMS} for each motor geometry and phase excitation is calculated, and the average F_{RMS} and median F_{RMS} calculate from the derived set become corresponding points in the data series for the respective plots.

To maintain consistency of scales between the plots, and the aid the comparison of the relative effects of the various geometry factors, the mean and median F_{RMS} values are expressed as ratios of the values obtained when the geometric property of interest is set to zero (the baseline geometry). This is expressed as the improvement in RMS force output ($\Delta_{F_{RMS}}$) where $\Delta_{F_{RMS}} > 1.0$ shows a positive effect of a geometric factor and $\Delta_{F_{RMS}} < 1.0$ shows that the geometric factor negatively impacts force production. $\Delta_{F_{RMS}} = 1.0$ indicates that there is no effect on F_{RMS}.

The introduction of f_p did not have any significant effect on the average and median F_{RMS} production of the motor. This null effect means that by packing more turns around the poles of the motor and taking advantage of the additional space permitted by introducing $f_p > 0$, would not

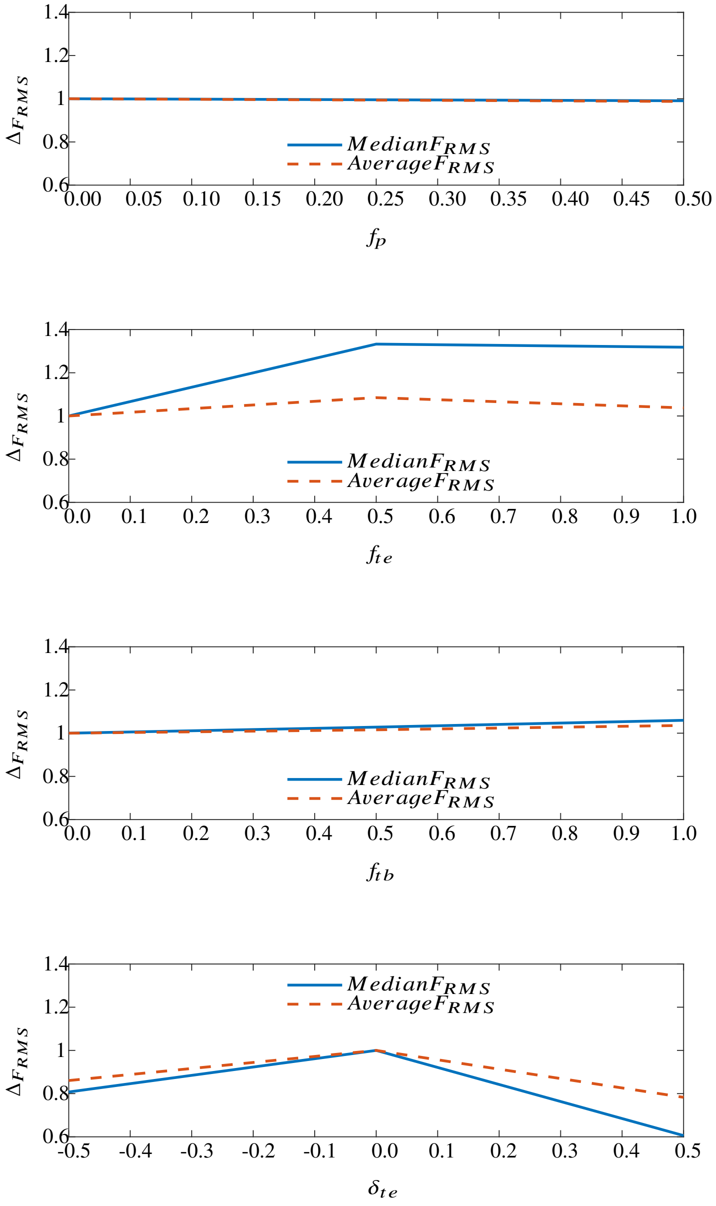

Figure 3.17 Comparison of the effect of pole fillet (f_p), tooth edge fillet (f_{te}), tooth base fillet (f_{tb}) and tooth edge offset (δ_{te}) on the average and median RMS force production (F_{RMS}) of the uncoupled linear variable reluctance (LVR) motor. $\Delta_{F_{RMS}}$ for each geometric property measures the ratio of the average and median RMS force production attained when the geometric property (f_p, f_{te}, f_{tb}, δ_{te}) is applied to that attained when it is not.

by itself increase the saturation of the motor. The fact that much of the flux path concentration in figure 3.14 occurs in the teeth and not the poles, supports this observation.

Figure 3.17 also shows that increasing f_{te} has the highest impact on increasing F_{RMS}. However, the benefits of introducing $f_{te} > 0$ are not monotonic, and it peaks at $f_{te} = 0.5$ although the improvement in RMS force output, $\Delta_{F_{RMS}} > 1.0 \forall f_{te} > 0.0$. This non-monotonic nature of the improvement needs to be further investigated by testing with a more refined set of f_{te} values since a polynomial fit of the comparison curves suggests that the best f_{te} would probably be in the range $f_{te} \in [0.5, 1.0]$.

Although figure 3.17 also shows f_{tb} as having a positive effect on improving F_{RMS}, the improvement is insufficient compared to that of f_{te} and any $f_{te} > 0.5$ yields an increase greater than that achievable by any f_{tb} value.

Both tapering and dovetailing of the tooth shape introduced by δ_{te} had the effect of significantly reducing F_{RMS}. As a result, that geometric factor has a net negative impact on force production.

3.4 Nonlinear Modeling

The stored results for each motor constitute a model for computing the flux linkage and force given current and position, or the desired currents for a commanded force. Force calculated by interpolation and force obtained via finite element analysis matched approximately for all tooth configurations for both the coupled and uncoupled motor.

3.5 Cubic Spline Interpolation for Each Motor Configuration

3.5.1 Uncoupled LVR motor

Using the force and flux linkage outputs from the model's database, MATLAB® was used to form a 2D gridded interpolant for each motor design. i_1 and x_n formed the grid's independent variables. Therefore, for any given x_n and i_1, the force, flux linkage, and stored magnetic co-energy can be determined by 2D cubic spline interpolation. Also, because the input data came from both the linear and nonlinear regions of the motor's operation, the model can be applied to all modes of operation. Even though results from magnetostatic FEA runs formed the model, it is still useful in the analysis of motor motion due to its provision of flux linkages and magnetic co-energy. Finally, interpolations are more suited to very computationally intensive optimization tasks since they are much faster than alternative regression models.

3.5.1.1 Verification of the Cubic Spline Interpolation Model

The model for motor design tooth shape factor (α), 0.4 was subjected to the test sine and square shaped excitation current waveforms defined in (3.25) and (3.26) respectively. Figure 3.18 shows the configurations of the trial i_1 excitations. Even though there are negative currents in these test current waveforms the sign of the excitation current has no effect on the sign of the force.

$$i_1(x_n) = 8sin(2\pi x_n) \tag{3.25}$$

$$i_1(x_n) = 8(-1)^{\lfloor 2x_n \rfloor} \tag{3.26}$$

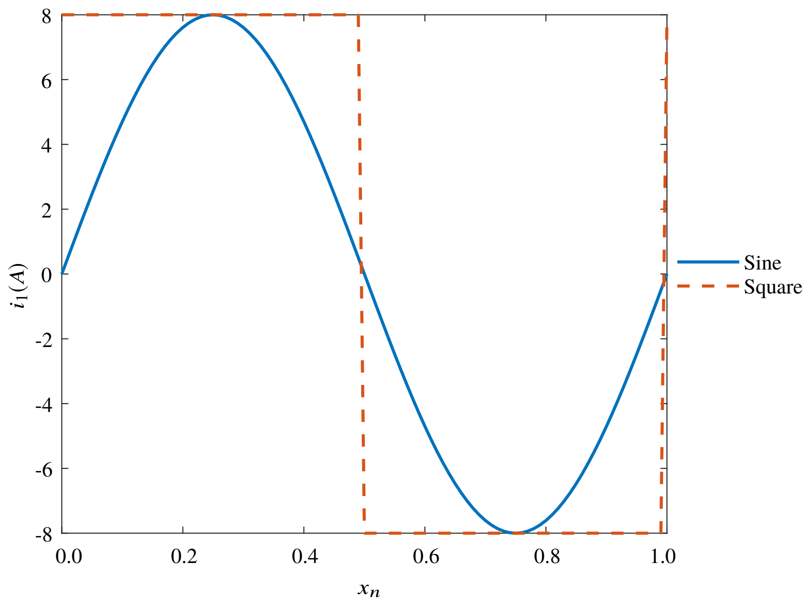

Figure 3.18 Variation of test phase 1 excitation (i_1) with linear motor position (x_n) for sine and square shaped excitation current waveforms

The force production predicted by the model is presented in figure 3.19 and compared with the results of determining the force production using FEA. It shows that the base uncompensated interpolation model deviates from the FEA prediction at an error of about 1.76% for the sine wave excitation and 6.83% for the square wave excitation. One prominent observation is that the deviation is minimum at the fully aligned and wholly unaligned positions and peaks at the during the maximum magnitude of instantaneous force production. Based on the different inputs that were tested, the deviation does not seem to depend on the excitation current. Still, it is a feature of the model deviating from the FEA prediction based on the position of the motor. As a result, the model or its outputs can be improved by compensating (expressing the error as a function of position and adding it to all model outputs) for the deviation based on the motor's position. Figure 3.19 shows that this compensated model matches the FEA prediction almost perfectly for all positions.

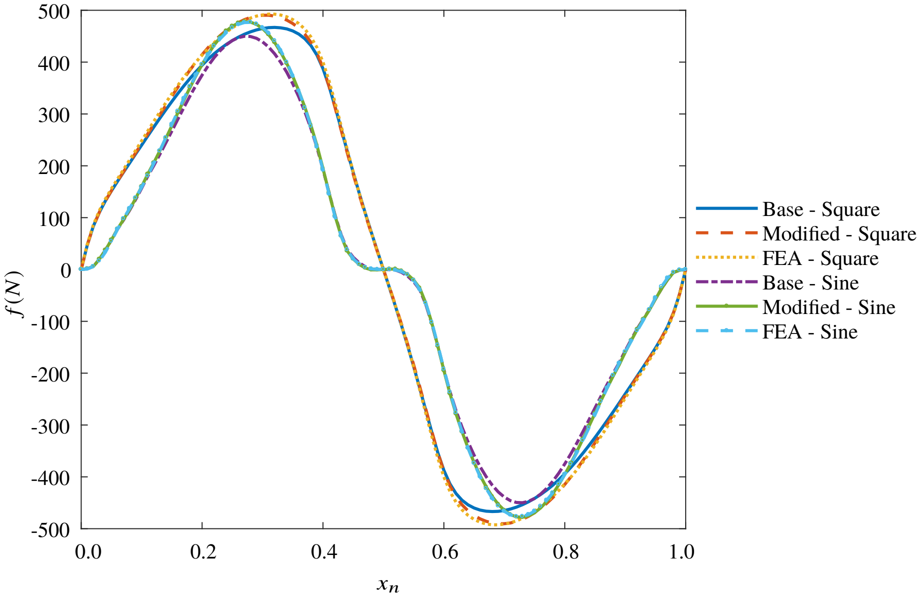

Figure 3.19 Comparison of instantaneous force production of the uncoupled linear variable reluctance motor with tooth shape factor ($\alpha = 0.4$) vs. linear motor position (x_n) for FEA, uncompensated (base) cubic spline interpolation model, and compensated (modified) cubic spline interpolation model when subjected to the sine and square phase 1 excitation current (i_1) waveforms. Other tooth geometry properties namely tooth edge fillet ($f_{te} = 0.0$), tooth base fillet ($f_{tb} = 0.0$), tooth edge scaling factor ($\delta_{te} = 0.0$) and pole fillet ($f_p = 0.0$) are held constant.

3.5.2 Coupled LVR motor

The model for motor design tooth shape factor $\alpha = 0.4$ was subjected to the test sinusoidal, square and triangular phase excitations defined in (3.25), (3.26) and (3.27).

$$i_j = 8(-1)^{\lfloor 2\gamma+0.5 \rfloor}\left(4\gamma - 2\lfloor 2\gamma + 0.5 \rfloor\right) \tag{3.27}$$

Where $\gamma = x_n - \frac{1}{3}(j-1)$ and $j \in \{1, 2, 3\}$

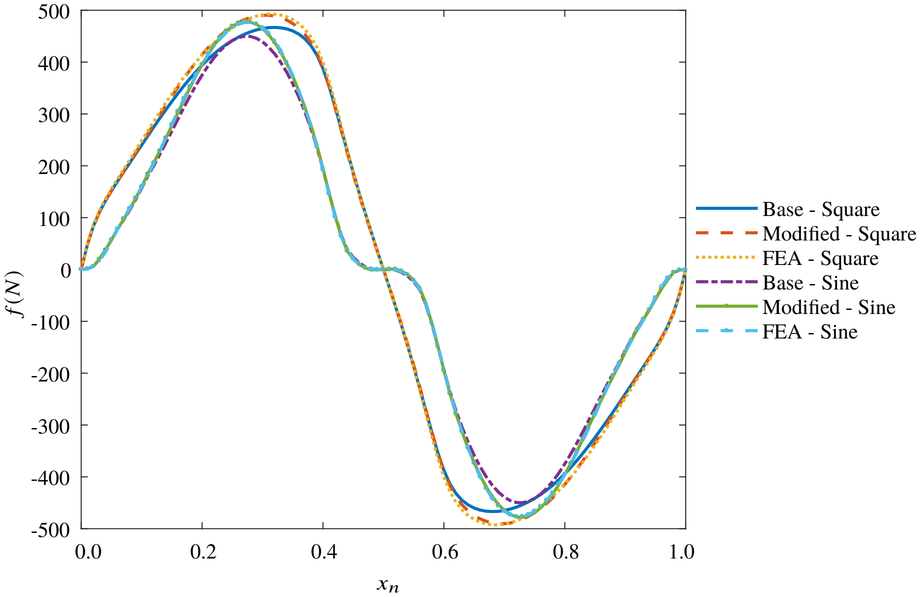

Figure 3.20 Comparison of instantaneous force production (f) vs. normalized motor position (x_n) plots for the coupled linear variable reluctance (LVR) motor with designed tooth shape factor ($\alpha = 0.4$). The *model* and *FEA* series are respectively for outputs obtained using 4D cubic spline interpolation of the motor model and finite element analysis. The *Sine*, *Square*, and *Tri* series are for outputs obtained when the motor is subjected to sinusoidal, square and triangular excitation currents respectively.

The force production predicted by the model is presented in figure 3.19 and compared with the results of determining the force production using FEA. Calculations show that the interpolation model deviates from the FEA predictions by 1.49%, 1.08%, and 1.23% respectively for the sin, square, and triangle commutations.

CHAPTER 4

OPTIMAL COMMUTATION

4.1 Introduction

Sets of excitation currents and motor positions were selected and applied in several finite element simulations to obtain a lookup table for instantaneous force output (f) for each motor geometry (α). All finite element simulations used the magnetostatic 2D solver in MagNet® [53], a flow solver that uses the finite element method to solve low-frequency electromagnetic problems. Data management was automated using a library of scripts developed on the architecture presented in [59].

$$f = f(i_1, i_2, i_3, x_n) \tag{4.1}$$

The set of currents included high enough values for the model to address saturation effects. The author has published portions of this chapter's material in [67].

4.2 Cost Function Setup

This section focuses on the mathematical formulation of the optimization problems that searched for the current profiles that yield some predefined objectives subject to the design constraints of the various motor geometries specified in table 2.1 and additional restrictions. Before discussing the additional constraints, it is necessary to define some prerequisite quantities of interest.

The phase excitation wave (I_k) for phase $k \in \{1, 2, 3\}$ describes the set of instantaneous currents ($i_k = i_k(x_n)$) in phase k windings for all x_n. These are specified in terms of the global normalized motor position (x_n) and not time due to the static relationship between the excitation currents and force.

$$I_k = \{i_k(\mathcal{X}_n)\} \tag{4.2}$$

The ampacity of the phase winding wires and the fact that reversing the phase excitation does not affect f imposes a lower and upper bound for I_k as follows.

$$I_{min} = \underbrace{\begin{pmatrix} 0 & 0 & \cdots & 0 \end{pmatrix}}_{Ntimes} A \tag{4.3}$$

$$I_{max} = \underbrace{\begin{pmatrix} 15 & 15 & \cdots & 15 \end{pmatrix}}_{Ntimes} A \tag{4.4}$$

Where $N = 101$ is the number of motor positions.

The instantaneous force wave for motor positions over one tooth pitch is $F = f(I_1, I_2, I_3)$ and the average force production for motor positions over one tooth pitch is:

$$F_{avg} = \int_0^1 \left[f(i_1, i_2, i_3) \right] dx_n \tag{4.5}$$

The instantaneous force ripple wave for motor positions over one tooth pitch is $\delta_F = \left|F - F_{avg}\right|$. The overall force ripple over one tooth pitch is calculated as the 2-norm of the instantaneous force ripple, as seen in (4.6).

$$\Delta_F = \sqrt{\int_0^1 \left|F - F_{avg}\right|^2 dx_n} \tag{4.6}$$

To enforce the periodicity between $\{I_k\}$ sets, I_2 and I_3 were expressed in terms of I_1 as shown in (4.7). The $\frac{1}{3}$ shift between adjacent phases leads to query points outside of $\mathcal{X}_n$, hence, the shape-preserving piecewise cubic hermite interpolation polynomial (PCHIP) [68] is used to implement (4.7).

$$I_k = I_1\left(\mathcal{X}_n + \frac{mod(4-k,3)}{3}\right) \tag{4.7}$$

The following is an outline for the mathematical formulation of the set of optimization problems under this study. These formulations apply to all motor designs, motor positions, and excitation currents, and the results of their implementation yield the optimal α and excitation current waveforms. See [10] for studies that use similar approaches in formulating the optimization problem.

- *Maximum Average Force* optimal commutation determines the phase excitation profiles (I_k) that maximize average force output subject to no additional constraints beyond those imposed by the motors' design characteristics. This problem is formulated as:

$$\underset{\{I_k,\alpha\}}{min}(-F_{avg}) \text{ s.t.} \begin{cases} I_k = I_1\left(\mathcal{X}_n + \frac{mod(4-k,3)}{3}\right) \\ \\ I_{min} \leq I_k \leq I_{max} \end{cases} \tag{4.8}$$

The result of optimization yields the unconstrained maximum average force ($F_{avg_{max}}$) and its associated force ripple is also the maximum force ripple that the motor can generate ($\Delta_{F max}$).

- *Ripple-Specified Maximum Average Force* optimal commutation produces the $\{I_k\}$ that maximize the average force whilst constraining the force ripple to a value that is less than its maximum $\Delta_{F max}$ value. Force ripple is specified by introducing a *force ripple factor* ($\beta \in [0, 1]$) such that force ripple limit ($\Delta_{F con}$) is defined in (4.9).

$$\Delta_{F con} = \begin{cases} \beta\Delta_{F max}, & \beta < 1 \\ \\ \infty, & \beta = 1 \end{cases} \tag{4.9}$$

The optimization problem is defined as follows using the finite subset $\beta \in \{0.005, 0.05, 0.1, 0.2, \cdots, 0.9\}$.

$$\underset{\{I_k,\alpha\}}{min}(-F_{avg}) \text{ s.t.} \begin{cases} \Delta_F \leq \Delta_{F con} \\ \\ I_k = I_1\left(\mathcal{X}_n + \frac{mod(4-k,3)}{3}\right) \\ \\ I_{min} \leq I_k \leq I_{max} \end{cases} \tag{4.10}$$

- *Minimum Copper Loss at Maximum Average Force* optimal commutation searches for the phase excitation current profiles (I_k) that minimize copper loss (4.11) while maximizing average force (F_{avg}).

$$P_{avg} = R\sum_{k=1}^{3}\int_{0}^{1} {i_k}^2 dx_n \tag{4.11}$$

Since the maximum average force has already been determined in (4.8), the ${F_{avg}}_{max}$ output is imposed as an equality contraint in the problem formulation as shown in (4.12).

$$\min_{\{I_k,\alpha\}}(P_{avg}) \text{ s.t.} \begin{cases} F_{avg} = {F_{avg}}_{max} \\ I_k = I_1\left(\mathcal{X}_n + \frac{mod(4-k,3)}{3}\right) \\ I_{min} \leq I_k \leq I_{max} \end{cases} \tag{4.12}$$

- *Ripple-Specified Minimum Copper Loss at Maximum Average Force* optimal commutation determines the phase excitation current profiles (I_k) that minimize copper loss (4.11) while maximizing average force (F_{avg}), subject to a ripple constraints ($\Delta_{F con}$) as defined in (4.9). The problem is formulated as follows.

$$\min_{\{I_k,\alpha\}}(P_{avg}) \text{ s.t.} \begin{cases} F_{avg} = {F_{avg}}_{max} \\ \Delta_F \leq \Delta_{F con} \\ I_k = I_1\left(\mathcal{X}_n + \frac{mod(4-k,3)}{3}\right) \\ I_{min} \leq I_k \leq I_{max} \end{cases} \tag{4.13}$$

4.3 Optimization With Nonlinear Model

This presents the results of solving each of the optimization problems presented in section 4.2 using *multistart* solver and *fmincon* in MATLAB®.

4.3.1 Maximum Average Force

4.3.1.1 Uncoupled LVR motor

Figure 4.1 shows the results of solving the maximum average force problem formulated in (4.8) for each uncoupled LVR motor geometry (α). The first plot shows the maximum average force output (F_{avg}) of each motor geometry when subjected to optimal commutation current waves. Under these conditions, the associated force ripple with the instantaneous force output waves is also the maximum possible force ripple (Δ_F) for each motor design, as seen in the second plot. The first plot shows that F_{avg} rises from a minimum at $\alpha = 1.0$ to peak at $\alpha = 0.4$, after which it falls off at the same rate as the rise to $\alpha = 0.0$. On the other hand, the second plot shows that Δ_F rises from a minimum at $\alpha = 0.0$ to a peak at $\alpha = 0.6$ then falls off at the same rate as the rise to $\alpha = 1.0$. The variation of F_{avg} and Δ_F over tooth geometry $\alpha \in [0, 1]$ is not due to a difference in the optimal excitation current waves. From figure 4.5, the excitation current waves under this condition does not change with tooth geometry. Even though the optimization problem did not specify turn-on and turn-off x_n positions, the instantaneous excitation current is set to the maximum of $15A$ for a particular subset of $\mathcal{X}_n$ for each phase winding and turned off to $0A$ for all other positions. The instantaneous force waves are, however, distinct for each α due to a difference in flux paths and saturation resulting from geometric differences in their tooth shapes.

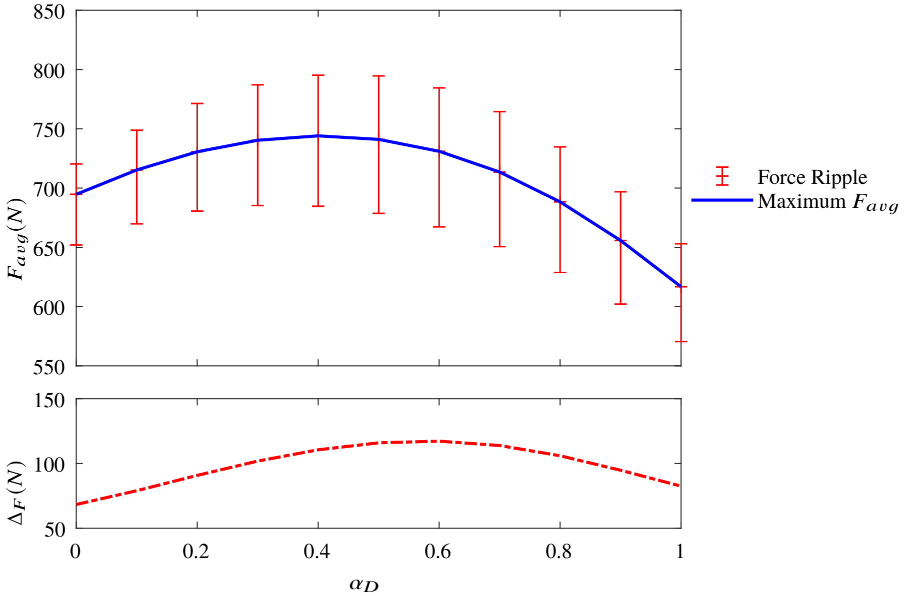

Figure 4.1 The variation of maximum average force (F_{avg}) and force ripple (Δ_F) when each uncoupled linear variable reluctance (LVR) motor design (α) is subjected to its specific optimal commutation current waveforms (I_1, I_2, I_3) that maximize average force (F_{avg}).

The previous observations imply that for all possible ripple constraints that may be specified, $\alpha \in [0.0, 0.4]$ is the range of tooth geometries that yield the highest F_{avg}. Tooth geometries with $\alpha > 0.4$ are likely to produce lower F_{avg} outputs while still producing higher Δ_F. For applications where maximum throughput is not affected by the amount of force ripple, the motor geometry with $\alpha = 0.4$ is best suited.

4.3.1.2 Coupled LVR motor

Solving (4.8) determines the optimal geometry and commutation current waveforms that maximize the average force (F_{avg}) output.

Figure 4.2 shows that the maximum average force output of the coupled LVR motor depends on α. It is maximum at $\alpha = 0.4$ symmetrical about it; $\alpha = 1.0$ produces the lowest F_{avg} as a result.

On the other hand, the ratio of maximum average force to force ripple is lowest for $\alpha = 0.7$ and symmetrical about it. Thus, $\alpha = 0.0$ has the highest F_{avg}/Δ_F. Also, Δ_F is maximum at $\alpha = 0.6$ and symmetrical about it; leading to a minimum Δ_F occuring at $\alpha = 0.0$. These are consistent with the findings of [67] that all possible force ripple constraints can be satisfied with $\alpha \in [0.0, 0.4]$. The

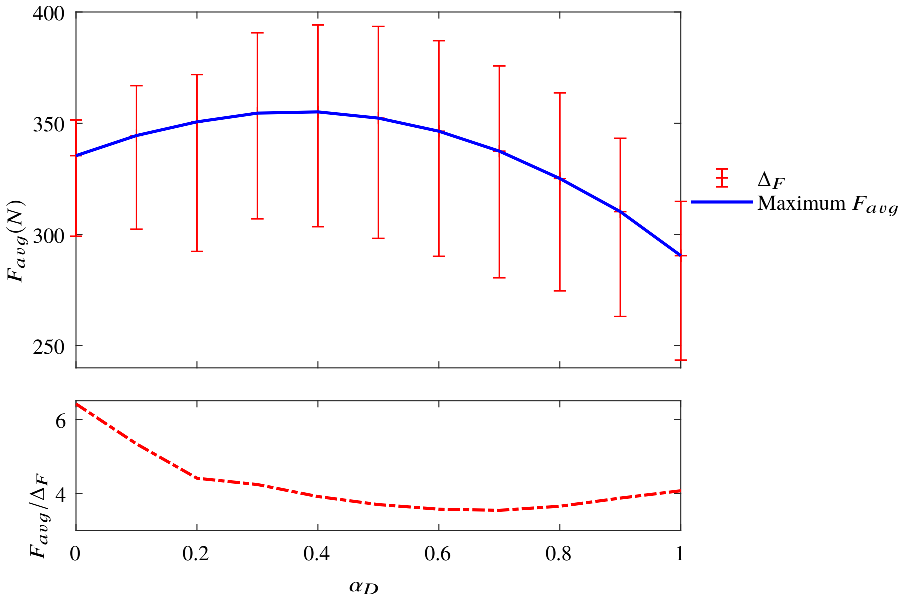

Figure 4.2 The variation of maximum average force (F_{avg}), force ripple (Δ_F) and F_{avg}/Δ_F to when each coupled linear variable reluctance (LVR) motor design (α) is subjected to its specific optimal commutation current waveforms (I_1, I_2, I_3) that maximize average force (F_{avg}).

optimal geometry for maximum average force is $\alpha = 0.4$, and its corresponding phase excitations currents are shown in figure 4.3, which also shows the resulting instantaneous force profile. The optimal commutation current waveforms are not switched (as in the case of the uncoupled LVR motor), but they are always on and alternating between positive and negative phase excitation.

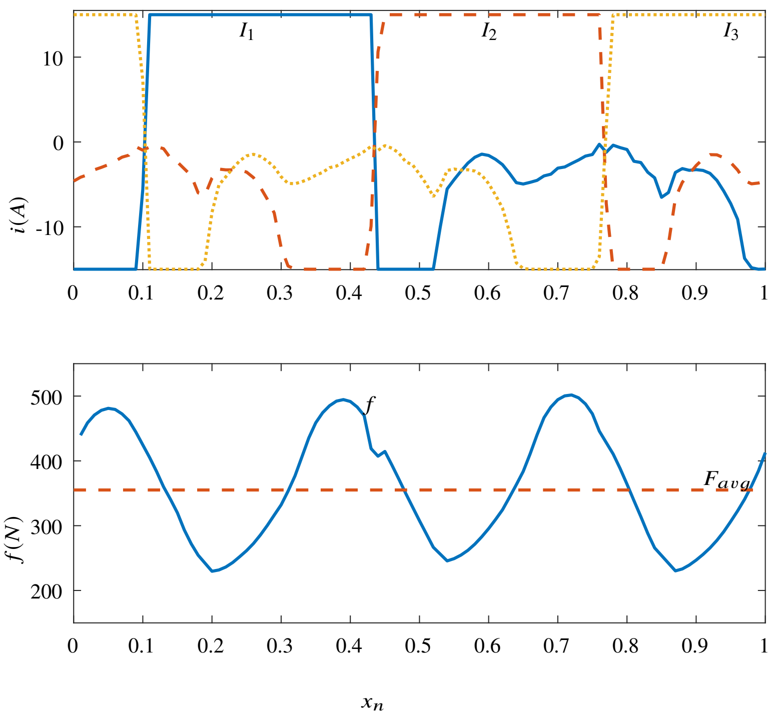

Figure 4.3 Optimal phase excitation (I_1, I_2, I_3) waveforms and the corresponding instantaneous force wave (f) and average force (F_{avg}) for coupled linear variable reluctance (LVR) motor with optimal airgap geometry ($\alpha = 0.4$) when maximizing average force (F_{avg}) subject to no force ripple constraint or power dissipation constraint. x_n is the normalized motor positon expressed as a ratio of motor position (x) to tooth pitch (p_t).

4.3.2 Ripple-Specified Maximum Average Force

4.3.2.1 Uncoupled LVR motor

Each series plot in figure 4.4 shows the variation of F_{avg} attained by solving (4.10) for a given uncoupled LVR geometry (α) while changing β from a high of 1.0 to a low of 0.05. In general, F_{avg} decreases for all α as β decreases from 1.0 to 0.05 and the marginal rate of this drop increases with decreasing β. Also, the general reduction in F_{avg} is affected by the choice of α. It is highest for $\alpha = 0.5$ and lowest for $\alpha \in \{0.0, 1.0\}$ with its value being inversely proportional to $|\alpha - 0.5|$. From figure 4.4 it is clear the motor geometry with $\alpha = 0.4$ is most suitable for producing

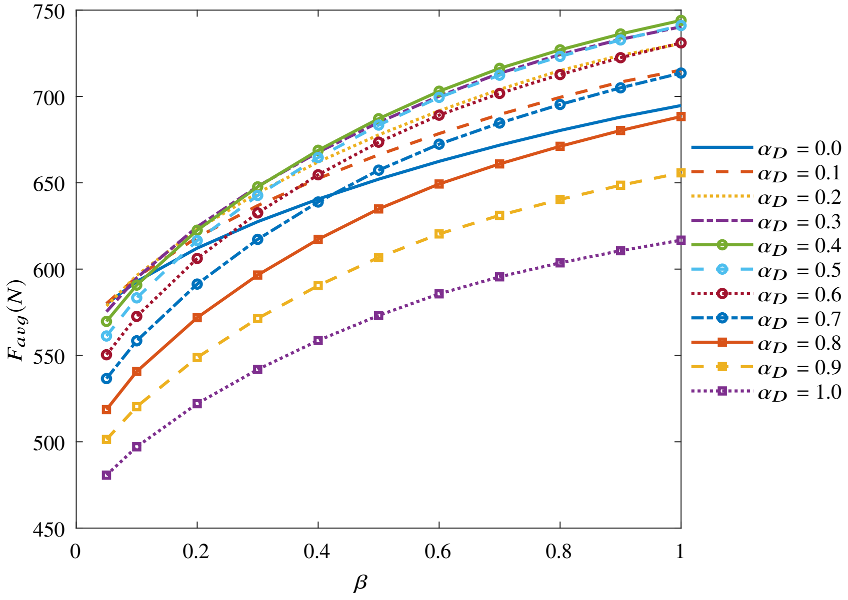

Figure 4.4 Plots of maximum average force (F_{avg}) versus force ripple factor (β) attained by maximizing F_{avg} and limiting force ripple (Δ_F) subject to a constraint imposed by β. α is the tooth shape factor for the uncoupled linear variable reluctance (LVR) motor geometry for each series.

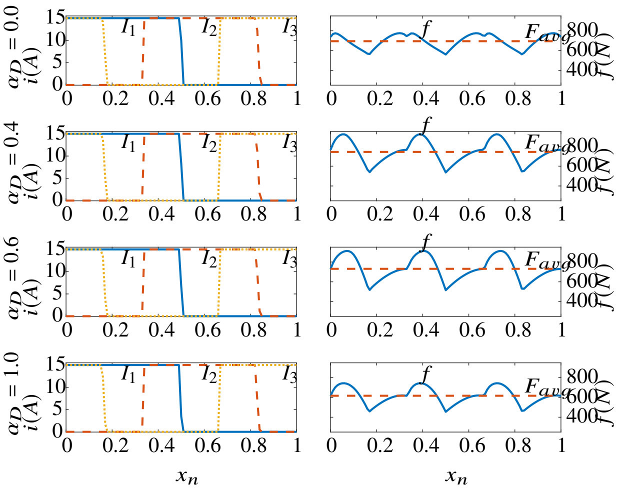

Figure 4.5 Plots of optimal phase excitation (I_1, I_2, I_3), the corresponding instantaneous force wave (f) and average force (F_{avg}) for uncoupled linear variable reluctance (LVR) motor geometries with designed tooth shape factor $\alpha \in \{0.0, 0.4, 0.6, 1.0\}$ when maximizing F_{avg} subject to no force ripple or power dissipation constraints. x_n is the normalized motor positon expressed as a ratio of motor position (x) to tooth pitch (p_t).

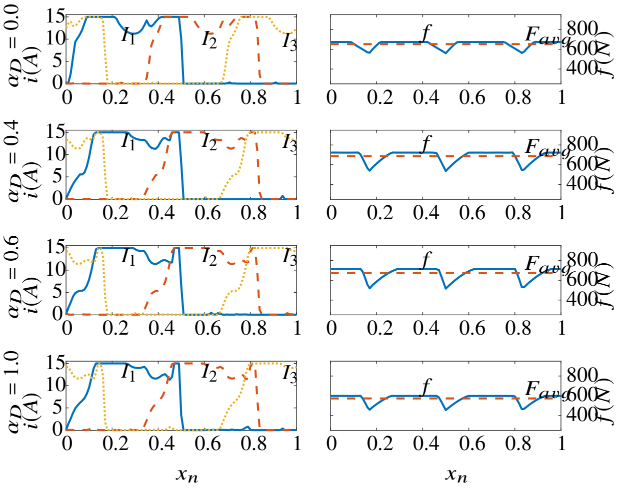

Figure 4.6 Plots of optimal phase excitation (I_1, I_2, I_3), the corresponding instantaneous force wave (f) and average force (F_{avg}) for uncoupled linear variable reluctance (LVR) motor tooth geometries $\alpha \in \{0.0, 0.4, 0.6, 1.0\}$ when maximizing F_{avg} subject to force ripple constraint imposed by force ripple factor ($\beta = 0.5$) and unconstrained power dissipation. x_n is the normalized motor positon expressed as a ratio of motor position (x) to tooth pitch (p_t).

the highest F_{avg} for high force ripple applications with $\beta \geq 0.3$ and $\alpha = 0.0$ is most suited for applications where $\beta \leq 0.05$. For applications where $0.05 < \beta < 0.3$, the most suitable motor geometry is a choice in the range of $0.0 < \alpha < 0.4$.

The effect of force ripple constraint (β) on the optimal excitation current and intantaneous force waveforms at $\beta = 0.5$ and $\beta = 0.05$ are shown in figure 4.6 and 4.7 respectively. The imposition of β constraints has the effect of clamping the peaks of the instantaneous force wave and reducing the maximum gradient of the optimal commutation current waves. The former leads to a reduction in the F_{avg} for the instantaneous force wave profiles, and the latter could lead to the possibility of operating the motors at higher speeds than those sustainable at unconstrained force ripple. Since this study focuses on the excitation current waves and therefore assumes that source

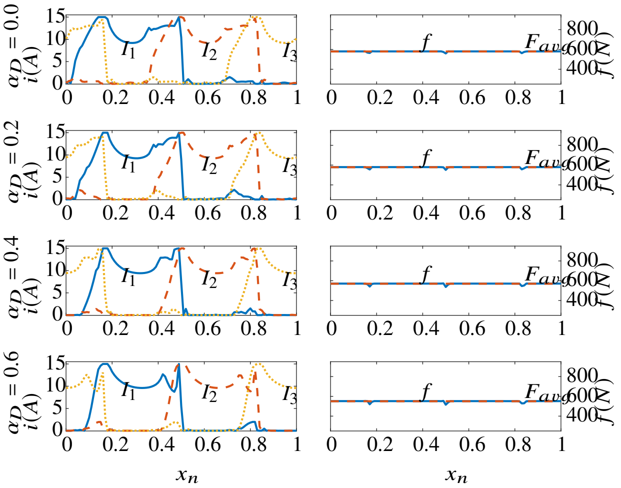

Figure 4.7 Plots of optimal phase excitation (I_1, I_2, I_3), the corresponding instantaneous force wave (f) and average force (F_{avg}) for uncoupled linear variable reluctance (LVR) motor tooth geometries $\alpha \in \{0.0, 0.4, 0.6, 1.0\}$ when maximizing F_{avg} subject to force ripple constraint imposed by force ripple factor $(\beta = 0.05)$ and unconstrained power dissipation. x_n is the normalized motor positon expressed as a ratio of motor position (x) to tooth pitch (p_t).

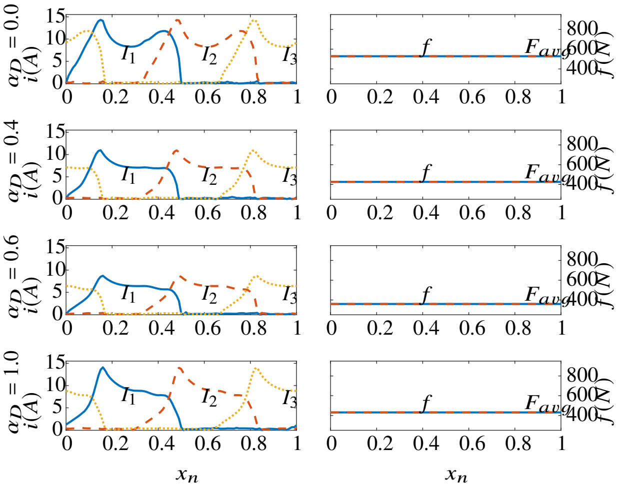

Figure 4.8 Plots of optimal phase excitation (I_1, I_2, I_3), the corresponding instantaneous force wave (f) and average force (F_{avg}) for uncoupled linear variable reluctance (LVR) motor tooth geometries $\alpha \in \{0.0, 0.4, 0.6, 1.0\}$ when minimizing power dissipation (P_{avg}) subject to maximum average force (F_{avg}) and a constraint force ripple limit imposed by force ripple factor $(\beta = 0.005)$. x_n is the normalized motor positon expressed as a ratio of motor position (x) to tooth pitch (p_t).

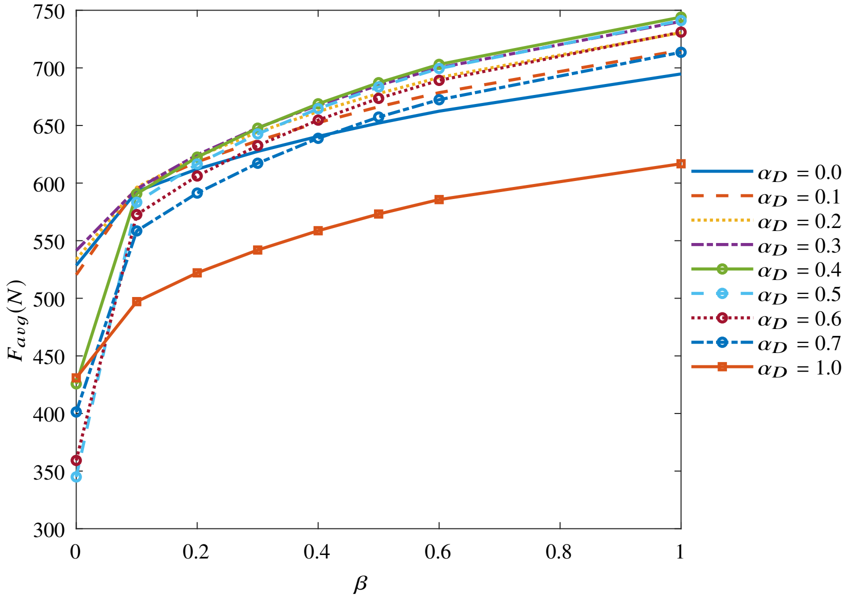

Figure 4.9 Plots of maximum average force (F_{avg}) versus force ripple factor (β) attained by minimizing average power disspation (P_{avg}) while maximizing F_{avg} and limiting force ripple (Δ_F) by subjecting it to a constraint imposed by β. α is the tooth shape factor for the uncoupled linear variable reluctance (LVR) motor geometry for each series.

voltage does not limit the motors' operation, the latter determination cannot be readily confirmed.

Ongoing studies that impose supply voltage limits are further investigating this possibility.

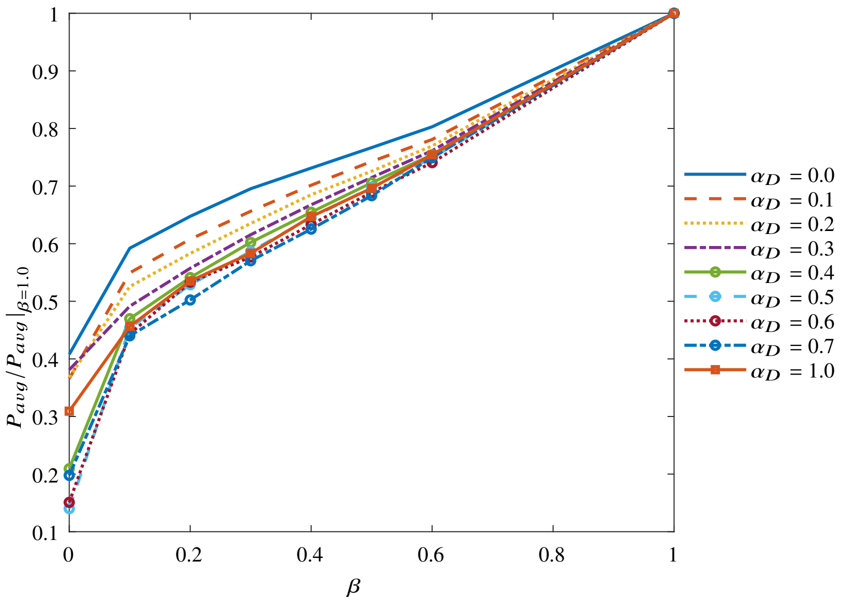

Figure 4.10 Plots of the ratio of the minimum power disspation (P_{avg}) at constrained ripple to the minimum power dissipation at unconstrained ripple optimal commutation versus force ripple factor (β) attained by minimizing P_{avg} while maximizing average force (F_{avg}) and limiting force ripple (Δ_F) by subjecting it to a constraint imposed by β. α is the tooth shape factor for the uncoupled linear variable reluctance (LVR) motor geome try for each series.

4.3.2.2 Coupled LVR motor

Solving (4.10) imposes the force ripple constraints, and it results in the reduction of the maximum average force output of motor with increasing force ripple constraint (reducing β). Optimal geometry also varies between $\alpha = 0.2$ and $\alpha = 0.4$. Figure 4.11 shows the variation of maximum F_{avg} and the optimal α with the imposition of force ripple constraint specified by force ripple factor ($\beta \in [0.15, 1.00]$). It shows that the drop in F_{avg} accelerates as β approaches zero.

At $\beta = 0.15$, the optimal airgap geometry is $\alpha = 0.3$ and the corresponding optimal commutation current waveforms are presented in figure 4.12 together with the instantaneous force

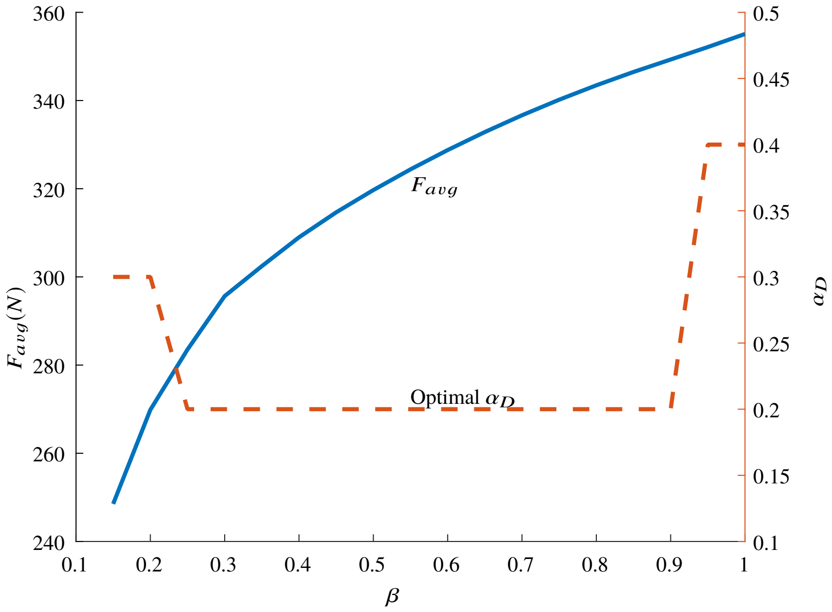

Figure 4.11 Maximum average force (F_{avg}) and the corresponding optimal airgap geometry (α) plotted against force ripple factor (β) attained by maximizing F_{avg} and limiting force ripple (Δ_F) subject to a constraint imposed by β.

output profile. Compared to figure 4.3, there is a significant increase in the harmonic content in the excitation current at low ripple, together with a reduction of F_{avg}.

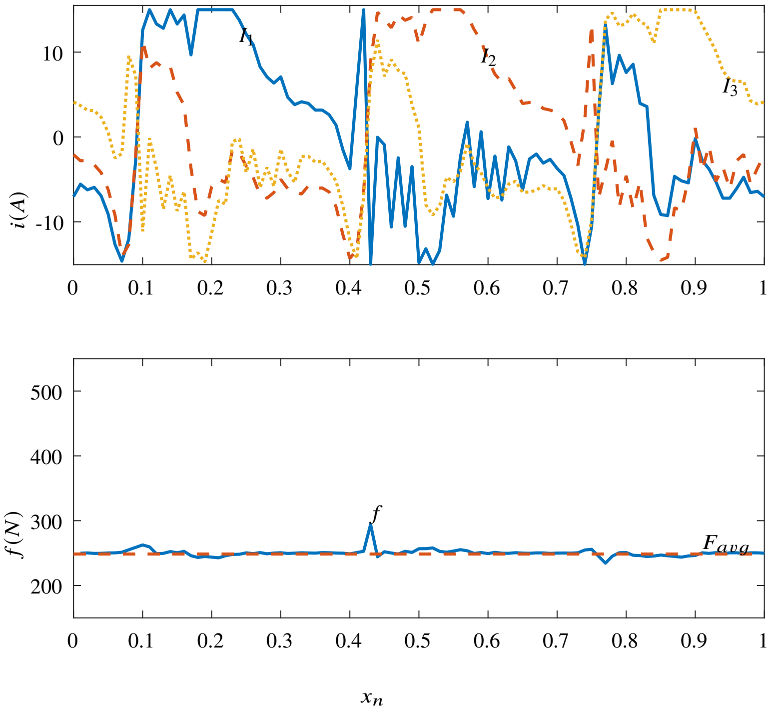

Figure 4.12 Optimal phase excitation (I_1, I_2, I_3) waveforms and the corresponding instantaneous force wave (f) and average force (F_{avg}) for coupled linear variable reluctance (LVR) motor with optimal airgap geometry ($\alpha = 0.3$) when maximizing average force (F_{avg}) subject to force ripple constraint imposed by force ripple factor ($\beta = 0.5$) and unconstrained power dissipation. x_n is the normalized motor positon expressed as a ratio of motor position (x) to tooth pitch (p_t).

4.3.3 Minimum Power Dissipation

4.3.3.1 Uncoupled LVR motor

Comparing figures 4.7 and 4.8, it is clear that the introduction of power dissipation limits allows for the imposition of tighter ripple constraints that lead to even smoother excitation current waveforms with less harmonic content. Also, the imposition of power dissipation and tighter ripple constraints cause the motors to operate under less saturation mostly.

The results of solving (4.12) and (4.13) for motors with $\alpha \in \{0.0, 0.2, 0.4, 0.6, 1.0\}$ are shown in figure 4.10 and 4.9. From figure 4.10, the steepest decline in the power dissipation rate are observed for $\alpha \geq 0.4$ while in figure 4.9, uncoupled LVR motor geometries with $\alpha \leq 0.4$ experience the least reduction in F_{avg} with the imposition of tighter force ripple constraints. This finding means that for applications where both high power dissipation and force ripple are undesirable, the uncoupled LVR motor with $\alpha = 0.4$ is most desirable.

4.3.3.2 Coupled LVR motor

The solution to (4.13) imposes minimum power dissipation constraints to the geometry and commutation optimization problem. The results show that the addition of power dissipation constraints had a less significant effect on the optimal geometry and commutation than force ripple, and it did not change the optimal geometry. There was a moderate change in the harmonic component of the optimal commutation current waveforms, but it was not significant to warrant a comparative analysis. Airgap geometry was, however, found to have a significant effect on minimum power dissipation, and lower α resulted in higher P_{avg}. Minimization of power dissipation, however, has implications for the efficiency of the motor and would need to be further examined in future optimal geometry and commutation studies that include the dynamic behavior of the motor. This line of study is relevant since it provides avenues to further improve the motor's efficiency by constraining power dissipation in a dynamic configuration.

4.3.4 Practical Range of Tooth Geometries

The findings of this study have shown that the practical range of tooth geometries for all applications is $\alpha \in [0.0, 0.4]$ for both the coupled and uncoupled configurations of the motor. On that basis, it is reasonable to introduce a practical geometry tooth shape factor ($\alpha_P \in [0, 1]$) for this useful range. Thus tooth width (w_t) and valley width (w_v) can be defined using α_P and tooth pitch (p_t) as follows.

$$w_t = \frac{p_t}{15}(5 + \alpha_P) \tag{4.14}$$

$$w_v = \frac{p_t}{15}(10 - \alpha_P) \tag{4.15}$$

As a result, the minimum practical tooth width is $\frac{1}{3}p_t$ when $\alpha_P = 0.0$ and $\frac{2}{5}p_t$ when $\alpha_P = 1.0$. Further studies need to be performed with the motor under dynamic conditions to verify this finding.

CHAPTER 5

CONCLUSION

5.1 Summary of Contributions

The discussions in previous chapters present a detailed finite-element-analysis-based characterization of a family of linear variable reluctance (LVR) motors with different tooth geometries. The research introduces a new expression for tooth shape factor to help in the analysis and design studies by constraining choices to the range of feasible tooth widths to this favorable range. Also, it shows a specific range of tooth edge fillets that improve the characteristics of LVR motors. It also demonstrated the limited favorable effect of tooth base fillets and adverse effects of tooth edge scaling on LVR motor characteristics.

Characterization showed the effects of motor position and excitation current on two motor output variables, namely instantaneous force, and phase flux linkage. Through these output variables, the analysis highlights salient characteristics of both coupled and uncoupled LVR motors, including force ripple, magnetic saturation, nonlinearity, and harmonics. These characteristics increase the complexity of operating and controlling the motor, and accurately modeling them is essential to this effort. Unlike the uncoupled LVR that can be analyzed based on single-phase excitation, developing optimal commutations for the coupled LVR motor requires excitation on all three phases, further complicating the analysis.

A data management system that includes a simulation driver managed the large dataset generated in characterization and applied in nonlinear modeling and optimal commutation. The system manages the generation, processing, storage, and retrieval of all data.

The complete dataset generated in characterization forms the basis for a nonlinear model for LVR motors. Applying a cubic spline interpolant over the data formed a nonlinear model of the LVR motors. The model relates input variables (displacement and phase currents) to corresponding outputs (force, coenergy, and phase flux linkages) using the stored data, which accounts for saturation and harmonics. The stored data serves an additional purpose by facilitating comparisons of the motors under study using three force production attributes. These attributes are the root mean square (RMS) averaged force (averaged over one tooth pitch), the RMS force density, and the ratio of RMS force density to copper loss. Tests show that the model can predict outputs that are comparable to finite element analysis (FEA) runs with a significantly lower computational cost. Closer agreement between the model and FEA results came by imposing a compensating factor that adjusts the outputs based on motor position. The verification of the model showed its predictive ability for instantaneous force output to be within 98% of force production when using finite element analysis (FEA).

Analysis of the data shows the influence of tooth geometry parameters on figures of merit, namely root mean square (RMS) averaged instantaneous force, RMS force density, and RMS force density to copper loss ratio. Motor characteristics have practical implications. For instance, knowing which geometry provides the maximum average force per mass is vital for fast-motion applications. The discussion shows that the selection of tooth width, the introduction of pole fillet, and the introduction of tooth edge fillets can yield improvement in the motor's force production.

Force production capability does not vary monotonically with tooth width or tooth fillet; instead, a particular tooth width and tooth fillet correspond to maximum average force (averaged over a tooth pitch). However, the introduction of tapering or dovetailing of the motor's teeth caused a reduction in the force production capability of the motor. This observation provides valuable insight into geometry optimization.

The study uses a nonlinear model to present comparative operating characteristics of a family of linear variable reluctance motors with magnetically uncoupled and couple phases for multiple objective functions subject to various constraints. Comparing optimization results (to maximize force or minimize copper losses with or without constraints on force ripple), shows a trade-off between power losses and force ripple minimization. It is also possible to identify the range of motor tooth geometries that are favorable for either objective. The results include the optimal current waveforms and corresponding instantaneous force waveforms for the select motor geometries that have performed best for given optimization and constraint scenarios.

5.2 Recommendations for Further Study

The characterization of LVR motors used 2D magnetostatic finite element analysis (FEA) since the variables of interest (namely instantaneous force, flux linkage, and magnetic co-energy) depend on the motor's position and phase excitation currents and are independent of time. The nonlinear model introduced in this document models most, but not all the factors that affect dynamic control of linear variable reluctance (LVR) motors. Future work could study the dynamic behavior of the motor by subjecting it to a phase voltage source and including the effects of motion on the phase voltage. Transient finite element simulations may help to develop a new model that applies to such studies. Also, applying a 3D FEA tool to refine the nonlinear model of the motor would improve its predictive accuracy in motor drive design.

Another approach to nonlinear modeling of the LVR motor would be to use machine learning algorithms to analyze the combined dataset for all motor geometries and applying a randomized sampling method such as Monte-Carlo analysis to train the model's dataset further. Such an approach opens the possibility of developing a fast unified model of the LVR motor that factors in all magnetic and geometric characteristics and can be invaluable in the development of more reliable drive systems for the LVR motor.

This study includes an analysis of the effect of tooth edge fillets on LVR motor characteristics, and it has demonstrated that a wide range of tooth edge fillets improves the force output of LVR motors. Further analysis is needed to refine the range of favorable tooth edge fillets and identify which values are favorable for various optimization objectives.

The findings in the study can be further validated experimentally by first developing a drive system using the nonlinear model of the optimal tooth geometry for both coupled and uncoupled LVR motors. The drive system can be applied to a prototype of the optimal LVR motor design to experimentally validate the results of this study against a control base design of the motor.

REFERENCES

[1] Nasar, S. A. and Boldea, I., *Linear Electric Motors: Theory, Design, and Practical Applications.*, Prentice-Hall Inc., Englewood Cliffs, New Jersey, 1987.

[2] Laithwaite, E. R., *A history of linear electric motors*, Macmillan, Basingstoke, 1987.

[3] Krishnan, R., *Switched Reluctance Motor Drives, Modeling, Simulation, Analysis, Design, and Applications*, Industrial Electronics Series, CRC Press LLC, 2001.

[4] Yang, H., Panda, S. K., and Liang, Y. C., "Experimental investigation of feedback linearization controller for switched reluctance motor," *PESC Record. 27th Annual IEEE Power Electronics Specialists Conference*, Vol. 2, Jun 1996, pp. 1804–1810 vol.2.

[5] Zhao, S. W., Wang, W. X., Yang, X. Y., and Cheung, N. C., "Analysis and design of a Linear Switched Reluctance Motor with force improvement," *2013 5th International Conference on Power Electronics Systems and Applications(PESA)*, Dec 2013, pp. 1–4.

[6] Ganji, B. and Askari, M. H., "Analysis and modeling of different topologies for linear switched reluctance motor using finite element method," *Alexandria Engineering Journal*, Vol. 55, No. 3, 2016, pp. 2531 – 2538.

[7] Garcia-Amoros, J., Andrada, P., Blanque, B., and Genesca, M. M., "Influence of Design Parameters in the Optimization of Linear Switched Reluctance Motor under Thermal Constraints," *IEEE Transactions on Industrial Electronics*, Vol. PP, No. 99, 2017, pp. 1–1.

[8] Song, S., Zhang, M., Ge, L., and Wang, L., "Multiobjective Optimal Design of Switched Reluctance Linear Launcher," *IEEE Transactions on Plasma Science*, Vol. 43, No. 5, May 2015, pp. 1339–1345.

[9] Wang, D., Wang, X., and Du, X. F., "Design and Comparison of a High Force Density Dual-Side Linear Switched Reluctance Motor for Long Rail Propulsion Application With Low Cost," *IEEE Transactions on Magnetics*, Vol. 53, No. 6, June 2017, pp. 1–4.

[10] Ahmed, R. and Taylor, D., "Targeted-ripple optimal commutation of coupled and uncoupled linear variable reluctance motors," *SoutheastCon 2015*, IEEE, April 2015, pp. 1–8.

[11] Ahmed, R. and Taylor, D. G., "Optimal Excitation of Linear Variable Reluctance Motors with Coupled and Uncoupled Flux Paths," *2006 IEEE International Symposium on Industrial Electronics*, Vol. 3, July 2006, pp. 2498–2503.

[12] Boakye-Boateng, N. A. and Ahmed, R., "Characterization and modeling of a linear variable reluctance motor considering a full range of feasible tooth widths with finite element method," *2017 IEEE Industry Applications Society Annual Meeting*, Oct 2017, pp. 1–7.

[13] Taylor, D. and Ahmed, R., "Comparative analysis of linear variable reluctance motors with coupled and uncoupled flux paths," *Thirty-Sixth Southeastern Symposium on System Theory, 2004. Proceedings of the*, IEEE, 2004, pp. 436–440.

[14] Chayopitak, N. and Taylor, D. G., "Dynamic simulation of a linear variable reluctance motor using coupled network models," *Thirty-Sixth Southeastern Symposium on System Theory, 2004. Proceedings of the*, 2004, pp. 160–164.

[15] Taylor, D. G. and Ahmed, R., "Analysis of a linear variable reluctance motor with magnetically coupled phases," *Proceedings of the Thirty-Fourth Southeastern Symposium on System Theory (Cat. No.02EX540)*, 2002, pp. 219–223.

[16] Ilic'-Spong, M., Marino, R., Peresada, S., and Taylor, D., "Feedback linearizing control of switched reluctance motors," *IEEE Transactions on Automatic Control*, Vol. 32, No. 5, May 1987, pp. 371–379.

[17] Haiqing, Y., Panda, S. K., and Chii, L. Y., "Performance comparison of feedback linearization control with PI control for four-quadrant operation of switched reluctance motors," *Applied Power Electronics Conference and Exposition, 1996. APEC '96. Conference Proceedings 1996., Eleventh Annual*, Vol. 2, Mar 1996, pp. 956–962 vol.2.

[18] Barhoumi, E. M., Hajji, M., and Ben Salah, B., "Design of a double stator LSRM with improvements in the mobile structure," *Renewable Energies and Vehicular Technology (REVET), 2012 First International Conference on*, 2012, pp. 194–198.

[19] Darabi, S. and Ardebili, M., "Optimization of driving force of linear switched reluctance motor," *Power Electronics, Drive Systems and Technologies Conference (PEDSTC), 2011 2nd*, 2011, pp. 71–74.

[20] Darabi, S., Mohammadi, A., and Hemati, S. H., "Advantages of longitudinal flux linear switched reluctance motor compared to transverse flux linear switched reluctance motor for levitation purposes," *Electrical and Computer Engineering (CCECE), 2011 24th Canadian Conference on*, 2011, pp. 000832–000835.

[21] Amin, B., Masoumi, M., and Mirsalim, M., "Field and Torque Calculation and Transient Analysis in Variable Reluctance Machines," *IEEE Transactions on Magnetics*, Vol. 53, No. 9, Sept 2017, pp. 1–9.

[22] MorÃşn, C., Garcia, A., and Somolinos, J. A., "Mathematical Model Switched Reluctance Motor," *Key Engineering Materials*, Vol. 644, Trans Tech Publ, may 2015, pp. 87–91.

[23] Naayagi, R. T. and Kamaraj, V., "A Comparative Study of Shape Optimization of SRM using Genetic Algorithm and Simulated Annealing," *2005 Annual IEEE India Conference - Indicon*, Dec 2005, pp. 596–599.

[24] Balaji, M. and Kamaraj, V., "Design optimization of Switched Reluctance Machine using Particle Swarm Optimization," *2011 1st International Conference on Electrical Energy Systems*, Jan 2011, pp. 164–169.

[25] Andrade, D. A. and Krishnan, R., "Characterization of switched reluctance machines using Fourier series approach," *Industry Applications Conference, 2001. Thirty-Sixth IAS Annual Meeting. Conference Record of the 2001 IEEE*, Vol. 1, 2001, pp. 48–54 vol.1.

[26] Chapman, P. L. and Sudhoff, S. D., "Design and precise realization of optimized current waveforms for an 8/6 switched reluctance drive," *IEEE Transactions on Power Electronics*, Vol. 17, No. 1, 2002, pp. 76–83.

[27] Lovatt, H. C. and Stephenson, J. M., "Computer-optimised smooth-torque current waveforms for switched-reluctance motors," *IEE Proceedings - Electric Power Applications*, Vol. 144, No. 5, Sep 1997, pp. 310–316.

[28] Lovatt, H. C. and Stephenson, J. M., "Computer-optimised current waveforms for switched-reluctance motors," *IEE Proceedings - Electric Power Applications*, Vol. 141, No. 2, Mar 1994, pp. 45–51.

[29] Ahmed, R. and Taylor, D. G., "Assessment of linear variable reluctance motor performance limits via finite element modeling," *Proceedings of the International Conference on Electrical Machines*, Sept. 2006, pp. 6 pages on CD–ROM.

[30] Du, J., Lu, P., and Liang, D., "Optimal design of a linear transverse-flux machine with mutually coupled windings for force ripple reduction," *IET Electric Power Applications*, Vol. 12, No. 2, 2018, pp. 271–280.

[31] Dowlatshahi, M., Nejad, S. M. S., Moallem, M., and Ahn, J. W., "Torque ripple reduction of switched reluctance motors considering copper loss minimization," *2014 IEEE International Conference on Industrial Technology (ICIT)*, Feb 2014, pp. 858–865.

[32] Pavlitov, C., Chen, H., Gorbounov, Y., Tashev, T., Georgiev, T., and Xing, W., "Switched Reluctance Motor Torque Ripples Reduction by the Aid Of Adaptive Reference Model," *SPEEDAM 2010*, June 2010, pp. 1276–1279.

[33] Evangeline, S. J. and Kumar, S. S., "Torque Ripple Minimization of switched reluctance drives - A survey," *5th IET International Conference on Power Electronics, Machines and Drives (PEMD 2010)*, April 2010, pp. 1–6.

[34] Lee, D. H., Liang, J., Lee, Z. G., and Ahn, J. W., "A Simple Nonlinear Logical Torque Sharing Function for Low-Torque Ripple SR Drive," *IEEE Transactions on Industrial Electronics*, Vol. 56, No. 8, Aug 2009, pp. 3021–3028.

[35] Kim, T. H., Lee, D. H., and Ahn, J. W., “Advanced non-linear logic torque sharing function of SRM for torque ripple reduction,” *INTELEC 2009 - 31st International Telecommunications Energy Conference*, Oct 2009, pp. 1–4.

[36] Gobbi, R. and Ramar, K., “Optimisation techniques for a hysteresis current controller to minimise torque ripple in switched reluctance motors,” *IET Electric Power Applications*, Vol. 3, No. 5, 2009, pp. 453–460.

[37] Nabeta, S. I., Chabu, I. E., Lebensztajn, L., Correa, D. A. P., da Silva, W. M., and Hameyer, K., “Mitigation of the Torque Ripple of a Switched Reluctance Motor Through a Multiobjective Optimization,” *IEEE Transactions on Magnetics*, Vol. 44, No. 6, June 2008, pp. 1018–1021.

[38] Hur, J., Kang, G. H., Lee, J. Y., Hong, J. P., and Lee, B. K., “Design and optimization of high torque, low ripple switched reluctance motor with flux barrier for direct drive,” *Conference Record of the 2004 IEEE Industry Applications Conference, 2004. 39th IAS Annual Meeting.*, Vol. 1, Oct 2004, p. 407 Vol.1.

[39] Husain, I., “Minimization of torque ripple in SRM drives,” *IEEE Transactions on Industrial Electronics*, Vol. 49, No. 1, Feb 2002, pp. 28–39.

[40] Garip, M., Ozoglu, Y., and Mese, E., “An approach to torque ripple reduction in fully pitched switched reluctance motors by pole tip shaping,” *11th IEEE Mediterranean Electrotechnical Conference (IEEE Cat. No.02CH37379)*, 2002, pp. 157–161.

[41] Reay, D. S., Green, T. C., and Williams, B. W., “Minimisation of torque ripple in a switched reluctance motor using a neural network,” *1993 Third International Conference on Artificial Neural Networks*, May 1993, pp. 224–228.

[42] Kavanagh, R. C., Murphy, J. M. D., and Egan, M. G., “Torque ripple minimization in switched reluctance drives using self-learning techniques,” *Industrial Electronics, Control and Instrumentation, 1991. Proceedings. IECON ’91., 1991 International Conference on*, Oct 1991, pp. 289–294 vol.1.

[43] Zaharia, M. V., Laczko, A. A., Pop, A. A., Radulescu, M. M., and Gillon, F., “Optimal commutation angles of a switched reluctance motor/generator,” *2015 Tenth International Conference on Ecological Vehicles and Renewable Energies (EVER)*, March 2015, pp. 1–8.

[44] Xu, Y. Z., Zhong, R., Chen, L., and Lu, S. L., “Analytical method to optimise turn-on angle and turn-off angle for switched reluctance motor drives,” *IET Electric Power Applications*, Vol. 6, No. 9, November 2012, pp. 593–603.

[45] VujiÄŊiÄĞ, V. P., “Minimization of Torque Ripple and Copper Losses in Switched Reluctance Drive,” *IEEE Transactions on Power Electronics*, Vol. 27, No. 1, Jan 2012, pp. 388–399.

[46] Prabhu, V. V., Mahesh, K. S., and Renuka, C., “Simulation of Switched Reluctance motor/-generator with optimum turn-on and turn-off control for the application of variable speed

drives," *International Conference on Sustainable Energy and Intelligent Systems (SEISCON 2011)*, July 2011, pp. 501–506.

[47] Shirahase, M., Morimoto, S., and Sanada, M., "Torque ripple reduction of SRM by optimization of current reference," *The 2010 International Power Electronics Conference - ECCE ASIA -*, June 2010, pp. 2501–2507.

[48] Xue, X. D., Cheng, K. W. E., and Ho, S. L., "Optimization and Evaluation of Torque-Sharing Functions for Torque Ripple Minimization in Switched Reluctance Motor Drives," *IEEE Transactions on Power Electronics*, Vol. 24, No. 9, Sept 2009, pp. 2076–2090.

[49] Deskur, J., Pajchrowski, T., and Zawirski, K., "Optimal control of current commutation of high speed SRM drive," *2008 13th International Power Electronics and Motion Control Conference*, Sept 2008, pp. 1204–1208.

[50] Sozer, Y. and Torrey, D. A., "Optimal turn-off angle control in the face of automatic turn-on angle control for switched-reluctance motors," *IET Electric Power Applications*, Vol. 1, No. 3, May 2007, pp. 395–401.

[51] Silvester, P. P. and Ferrari, R. L., *Finite Elements for Electrical Engineers*, Cambridge University Press, 3rd ed., 1996.

[52] Kuczmann, M. and Iványi, A., *The Finite Element Method in Magnetics*, Akadémiai Kiadó, Budapest, 2008.

[53] "MagNet v7," .

[54] Costabel, M., "A coercive bilinear form for MaxwellâĂŹs equations," *Journal of Mathematical Analysis and Applications*, Vol. 157, No. 2, 1991, pp. 527âĂŞ541.

[55] Bangerth, W., Davydov, D., Heister, T., Heltai, L., Kanschat, G., Kronbichler, M., Maier, M., Turcksin, B., and Wells, D., "The `deal.II` Library, Version 8.4," *Journal of Numerical Mathematics*, Vol. 24, 2016.

[56] Du, J. and Lu, P., "Optimal force ripple design of mutually coupled linear switched reluctance machines with transverse flux by Taguchi method," *2016 IEEE Conference on Electromagnetic Field Computation (CEFC)*, Nov 2016, pp. 1–1.

[57] Pupadubsin, R., Chayopitak, N., Taylor, D. G., Nulek, N., Kachapornkul, S., Jitkreeyarn, P., Somsiri, P., and Tungpimolrut, K., "Adaptive Integral Sliding-Mode Position Control of a Coupled-Phase Linear Variable Reluctance Motor for High-Precision Applications," *IEEE Transactions on Industry Applications*, Vol. 48, No. 4, July 2012, pp. 1353–1363.

[58] Group, T. O., "ArchiMate ® 3.0.1 Specification," 2017.

[59] Boakye-Boateng, N. A. and Ahmed, R., "A Windows-Based Framework for Enhancing Scalability and Reproducibility of Large-scale Research Data," *2018 ASEE Southeastern Section Conference*, ASEE Southeastern Section, Mar 2018, pp. 1–4.

[60] Jang, G. and Lieu, D., “The effect of magnet geometry on electric motor vibration,” *Magnetics, IEEE Transactions on*, Vol. 27, No. 6, 1991, pp. 5202–5204.

[61] Murthy, S. S., Singh, B., and Sharma, V. K., “Finite element analysis to achieve optimum geometry of switched reluctance motor,” *TENCON '98. 1998 IEEE Region 10 International Conference on Global Connectivity in Energy, Computer, Communication and Control*, Vol. 2, 1998, pp. 414–418 vol.2.

[62] Hossain, S. A. and Husain, I., “A geometry based simplified analytical model of switched reluctance machines for real-time controller implementation,” *Power Electronics, IEEE Transactions on*, Vol. 18, No. 6, 2003, pp. 1384–1389.

[63] Taylor, D. G. and Ahmed, R., “Current limited optimal excitation of magnetically coupled linear variable reluctance motors,” *IEEE International Electric Machines and Drives Conference, 2003. IEMDC'03.*, Vol. 2, IEEE, June 2003, pp. 857–860 vol.2.

[64] Boakye-Boateng, N. and Ahmed, R., “Effects of Tooth Geometry on the Operating Characteristics of Linear Variable Reluctance Motors with Coupled Flux Paths,” *SoutheastCon 2018*, April 2018, pp. 1–8.

[65] Suriano, J. R. and Ong, C.-M., “Variable reluctance motor structures for low-speed operation,” *IEEE Transactions on Industry Applications*, Vol. 32, No. 2, Mar 1996, pp. 345–353.

[66] Chang, J., Kang, D. H., Viorel, I. A., and Larisa, S., “Transverse Flux Reluctance Linear Motor’s Analytical Model Based on Finite-Element Method Analysis Results,” *IEEE Transactions on Magnetics*, Vol. 43, No. 4, April 2007, pp. 1201–1204.

[67] Boakye-Boateng, N. and Ahmed, R., “Finite Element Based Optimal Commutation Under Multiple Objective Functions for Magnetically Uncoupled Linear Variable Reluctance Motors with Different Airgap Geometries,” *SoutheastCon 2019*, April 2019, pp. 1–7.

[68] Fritsch, F. N. and Carlson, R. E., “Monotone Piecewise Cubic Interpolation,” *SIAM Journal on Numerical Analysis*, Vol. 17, No. 2, apr 1980, pp. 238–246.

VITA

Nasir Abdulai Boakye-Boateng was born in Ijebu Ode in Ogun State, Nigeria, to Ghanaian parents Ahmad and Haleema Boakye. He is the last of eight children, having six sisters and a brother. After attending Labone Senior High School in Accra, Ghana, he completed his Bachelor of Science in Electrical/Electronic Engineering from Kwame Nkrumah University of Science and Technology (KNUST) in June 2006 in Kumasi, Ghana. He earned his CEMBA in Strategic and Quality Management from KNUST in 2012 and an MS Electrical Engineering from the University of Tennessee at Chattanooga in May 2013.

Nasir is currently a Senior Software Engineer in Abundant Robotics, Inc in California and is part of a team developing a robotic apple harvester. He is also collaborating with a team of Orthodontic Doctors from Harvard University to create a 3D Indirect Bonding system for archwire placement using tunnel attachments. He lives in California with his wife, Ammatur-Raheem, and three children.